GENERATION OF QUANTUM DOTS
via nanoindentation in MoS_2

José David Hernandez
Universidade Federal de Minas Gerais
ICEx, Departamento de Física.

Advisor: Paulo Sérgio Soares Guimarães

Co-advisor: Pierre-Louis de Assis

Dissertation presented to the ***Universidade Federal de Minas Gerais*** to partially fulfill the requirements for the degree of Master of Sciences in Physics.

Belo Horizonte, July of 2016

Fue en la selva, en la amazonia ecuatoriana.
Los indios shuar estaban llorando a una abuela moribunda.
Lloraban sentados, a la orilla de su agonía. Un testigo, venido de otros mundos, preguntó:
- ¿Por qué lloran delante de ella, si todavía está viva?
Y contestaron los que lloraban:
- Para que sepa que la queremos mucho.

A doña Aurora

CONTENTS

LIST OF FIGURES

ACKNOWLEDGMENTS-AGRADECIMENTOS

Primeiramente eu agradeço ao universo, por ser mestre, deleite, tela e tinta e tormento, ao mesmo espaço e ao mesmo tempo.
Ao Prof. P. S. Soares Guimarães, meu orientador, pelo imenso apoio e compreensão. Pelo seu interesse nos aspectos extra-acadêmicos dos seus alunos e as suas tentativas de faze-los se tornarem em físicos experimentais. Ao meu co-orientador P. L. de Assis pelas suas sugestões na minha pesquisa, pelas discussões sobre tópicos fundamentais da física como ondas planas, osciladores harmônicos e transformadas de Fourier. Por ser um grande exemplo a seguir. Ao Thales, pela sua infinita paciência e as tentativas de ensinar-me a técnica de AFM, pela sua colaboração nos aspectos mais vitais desta pesquisa, como as nanoindentações e o estudo dos substratos. Por ter-me ensinado a exfoliar MoS_2 e criar minhas próprias receitas.
Aos meus pais, Miguel e Isabel, meus irmãos Diana e Jesús, as minhas avós Emma e Aurora, amo vocês com todo o meu coração, aos meus primos e amigos da minha terra, por terem me apoiado na minha idéia de estudar fora, de não desistir e por serem uma ótima razão para sempre voltar. Ao Eliel, por ser um ótimo *roommate* e pelas conversações lógicas (e as vezes falaciosas) sobre os infinitos e importansíssimos campos da besteira, o absurdo e a música. Ao bonde dos Rafamés: Jojo da Bahia, Tassius, Davi, Pedro, Hakob, Mirna, Igor, Mariana, Andreij, Joyce, Sangram, pombo-sujo, e o dr. Bolinho: sempre foi divertido rafamear com vocês; à galera da Capoeira Angola do mestre João: Thalesman, Lucas, Maurízio, Larissa, Gustavo... pelo jogo bonito e pelo muito axé. À Gabi, a Barbara Daros, a Raquel e a Amapola, suas lindezas: Por terem sido amor, sensibilidade, luta e arte. Ao pessoal da física: às meninas Ana Clara e Danielle, Wilmer, Guillermo, Wescley,

Nestor, Leonel, Nathan, Luisa, Pacho e demais, pela acolhida no DF. Ao pessoal do laboratório de semicondutores: Dudu, Thiagueta, Campô, Juan, Sara, as Barbaras e as Julianas, pelo acompanhamento e pelas infinitas dúvidas de laboratorio que vocês tiraram. Ao Elvis, a Milena e a pequena Victoria, por terem sido a minha segunda família nesta terra distante.
Academicamente falando: Ao pessoal do laboratório de nanoscopia, especialmente ao Thales Fernandes pela ajuda na criação das amostras. Ao pessoal do laboratório de espectroscopia ao prof. Leandro Malard e ao Cassiano pelas medidas dos hiperespectros. Ao pessoal da espectroscopia Raman à prof. Ariete Righi pela colaboração nas medidas de espectros de fotoluminescência e de Raman quando eu mais precisei.
A todos, por terem corrigido meu português ao longo destes dois anos. À agencia CAPES, pelo apoio financeiro no desenvolvimento da minha pesquisa, ao CNPQ e a Fapemig, pelo apoio ao Laboratório de Semicondutores e finalmente, ao povo brasileiro que contribui (muitas vezes sem saber) a não deixar morrer à ciência neste país.

J. D. H. R.

ABSTRACT

We predict the confinement of excitons in quantum dots generated by strain via the atomic force microscope (AFM) in atomically thin molybdenum disulfide (MoS_2). MoS_2 is a transition metal dichalcogenide (TMDC) and a bidimensional material which is now being studied due to its potential applications for transistors, detectors, sensors and single-photon emitters. We used an AFM probe to indent a monolayer flake of MoS_2 over a poly-methyl methacrylate (PMMA) and thus generate an energy funnel of nanometric scale in which the excitons can be confined. The PMMA substrate has elastic-plastic properties that allow the indentations to have the suitable size to generate quantum dots.

We make a review of the electronic, mechanical, vibrational and optical features of MoS_2 in order to describe the exciton and how it is affected by the presence of a strain field. We make use of the *deformation potential* theory, and combine it to the $k \cdot p$ perturbation theory to describe the exciton energy and wavefunctions as a funcion of the biaxial strain. We also model the nanoindentation via the method of finite elements and find that the most feasible conditions for achieving exciton confinement at 10 K are 15 nm - size and 2% - 3% average strained indentations.

We review the experimental aspects of the AFM technique such as the contact and non-contact mode, the properties of the cantilever and the tip in order to estimate the force applied on the material at each nanoindentation. We also measure the mechanical response of PMMA to the deformation via AFM and obtain the stress-strain curve, showing that the substrate behaves plastically at the same regime in which MoS_2 is elastic, which is convenient for performing nanoindentations without damaging the TMDC. Additionally, we perform Raman spectroscopy and photoluminescence spectroscopy measurements to characterize the emission of

the strained MoS_2 at room and low temperatures. We introduce the *hyperspectrum* which allows us to map the indented sample with a sub-μm resolution and observe the local phenomena associated to the nanoindentation.
Despite we did not observe the single sharp emission lines that are a signature of quantum-dot emission, we observed both a redshift of the exciton emission due to the strain generated in the monolayer, and a slant due to the shift of the populations of charged and neutral exciton at the indentation.

Keywords: Molybdenum disulfide, mechanical exfoliation, quantum dots, exciton confinement, nanoindentation, atomic force microscopy, strain field, deformation potential, $k \cdot p$ theory, Raman spectrum, photoluminescence, elastic-plastic polymer, poly-methyl methacrylate, single photon emission, charged exciton, photoluminescence hyperspectrum.

INTRODUCTION

The quantum offers a plenty of possibilities for the development of technologies and the discovery of new phenomena in the microscopic world. *Bidimensional materials* and semiconductor *nanostructures* are widely used in detectors, sensors, lasers and even in quantum optics and quantum information experiments, as well as in fundamental physics research [1–4]. For instance, bidimensional materials are useful because of their interesting mechanical, topological and electronic properties [5–7], while nanosystems are attractive due to all those effects that emerge from the confinement of particles [8, 9]. In particular, we are interested in structures called *quantum dots*, which are nothing else than 3D confiners and are known for being the "*artificial atoms*" of the condensed matter. Additionally, the recent exploration of bidimensional systems since the graphene in the 2000's contributed to the achievement of a class of non-zero gap materials known as *transition metal dichalcogenides* (MoS_2, WS_2, $MoSe_2$, etc.) which display some interesting electronic features when subjected to mechanical deformation.

Thereby, the main *motivation* of this work is to develop and prove the hypothesis that quantum dots in atomic layers of molybdenum dysulfide (MoS_2) can be generated via *nanoindentation*. To achieve this goal, we shall review the strain-dependent phenomena on MoS_2 and describe it via perturbation theory and simulations of the confined wavefunctions; we will also analyze the physics of nano-indentations fabricated via atomic-force-microscopy (AFM), which is a common technique used to study mechanical properties of materials. Finally, we characterize optically the quantum dots generated via nanoindentation through the *photoluminescence spectrum*, which is a powerful way to study the emission of any substance. In the

following paragraphs we will point out some arguments and historical background that constitute the basis of our work.

The quantum dot and the materials in the flatland

As *atoms* and *molecules* display quantized attributes such as energy, vibrational and angular momentum, then the transitions between quantum states that lead to light emission are sharp, making it easy to define discrete collective quantum states. Nevertheless, it is harder to achieve this regime in condensed matter systems because the strong interactions between atoms tend to obscure the individual states of the atoms and molecules. Instead of discrete levels of energy we observe bands which are filled with many charge carriers, then the electronic transitions are broad and incoherent.

Although the coherence properties of atoms and molecules make the quantum processes be more evident and suitable for quantum information and computation than those in condensed matter systems, the latter are closer to any practical application. Then we should find the means to generate structures that imitate the same features of atoms and molecules: such structures have already been found, and are known as *quantum dots*. Incredibly versatile, they can be combined with cavities to produce states of ligth-matter interaction, or generate two-state quantum bits to perform computation tasks.

Since their discovery in colloidal solutions in the 1980s, the study of quantum dots grew rapidly because of their capacity to combine the properties of bulk solid state systems and those of discrete molecules [10]. Also, their energy levels can be tuned through adjusting the dot size and composition, making them able to be part of optoelectronic devices in the infrared and the visible. There exist some ways to create quantum dots, such as epitaxial *semiconductor heterostructures*, *colloidal*, *defect vacancies* in crystals, or *zero-dimensional* fullerenes.

Apart from the mentioned before, quantum dots are able to be produced in graphene (or any 2D material by default) by growing tiny crystals which are then deposited on a substrate, or left suspended in a liquid [11]. Their unique features, such as high absorption and intense photoluminescence have made two-dimensional materials very attractive to generate quantum dots. Moreover, 2D crystals such as *Molybdenum disulfide* could be transferred to the top of a photonic crystal to enhance the photon emission and to couple light with matter. Atomically thin molybdenum disulfide have been recently discovered [12] and gained a lot of attention together with other *transition metal dichalcogenides* because they are direct band-gap semiconductors, thus the optical processes are more efficient in them than those in graphene.

Hybrid devices such as lead(II) sulfide PbS colloidal quantum dots [13], or even graphene nanocrystals [14] are deposited over a MoS_2 sheet to enhance the quantum efficiency of photodetectors. Other way of creating quantum dots is making them of MoS_2, by the means of liquid exfoliation and sonication in which nanocrystals of monolayers are suspended: very tiny cristals ($\approx$ 2 nm size) have been reported with this technique [15,16], and can be implemented as catalysts for efficient

evolution of hydrogen (electrolysis) [17]. Perhaps the most successful attepmt of producing quantum dots in 2D materials is through the trapping of excitons within defects of the lattice. In 2015, four different groups claimed to have characterized single-photon sources in tungsten selenide (WSe_2) [18–21]: very sharp emission lines and photon antibunching at low temperatures reveal the quantumness of the light produced by these defects. The defects are spontaneously generated as vacancies of chalcogen atoms, and are hard to control and tune, which is an important difficulty for their implementation in devices.

Now, in order to engineer a quantum dot in a 2D material, scientists have been used the fact that the electronic properties are highly dependent on the strain, to create exciton funnels [22] or even quantum confiners at exact positions. For instance, we also know an attempt in 2015 to produce strain-induced quantum emitters in WSe_2, in which spectral isolation was achieved at very specific places at the edge of a suspended membrane [23] on a pre-patterned SiO_2 substrate. However, it is hard to know where along the edge the quantum dots will appear. Until now, the possibility to generate QDs via AFM nanoindentation has been unexplored. In this work we address this possibility and explain how it allows us to achieve a better control of the dot properties and localization, and which are the advantages or disadvantages of this method compared to the other techniques mentioned above.

Summarizing, the importance of generating artificial atoms in condensed matter relies not only upon their almost infinite practical applications, such as quantum information processing, nanoscale lasers and optoelectronic devices, but also they may help us to understand the behaviour of the matter in the *nanoscale*. Here, MoS_2 is presented as a potential candidate for the generation of quantum dot structures because of its astonishing strain-dependent properties and the assumed facility of quantum dots being obtained through AFM nanoindentation. This work is divided in three parts in order to expose clearly the development of our hypothesis: Part I is devoted to address the MoS_2, the exciton and the strain-dependent phenomena. The subject of Part II is to describe the quantum dot and establish the hypothesis of exciton confinement in MoS_2, together with our main theoretical and experimental results. Finally, Part III is a short insight into the perspectives and main difficulties found along the progress of this work.

Part I is divided in four chapters, whose main topic is the molybdenum dysulfide: The first is a short chapter in which we introduce the MoS_2 and the different techniques for achieving the monolayer. In Chapter 2 we review the electronic, mechanical, excitonic and optical properties of MoS_2. Chapter 3 is devoted to explain in detail the experimental techniques used to produce and characterize the quantum dots in the samples. Chapter 4 is mainly theoretical, in which we present the calculation of the main features of the exciton, based on perturbative methods and simulations.

Part II consists on two chapters dedicated to present and discuss the results of our work: In Chapter 5 we state the hypothesis of exciton confinement, define the quantum dot and show our model based on the *deformation potential theory* for the exciton energy as a function of the strain field. In Chapter 6 we show our model of AFM nano-indentation and the results of the characterization via photolumines-

cence and Raman spectroscopy for both room-temperature and low-temperature regimes.

Part III has only one chapter: the conclusions and future work, in which we expose the difficulties and the possible reasons why the quantum dot generation and characterization were not completely successful. We also review other different measurements which may help us to corroborate the generation of quantum dots in MoS_2 atomic monolayers.

An general overview of our research is related to the organization of the ideas exposed in this work, which can be addressed from the following diagram:

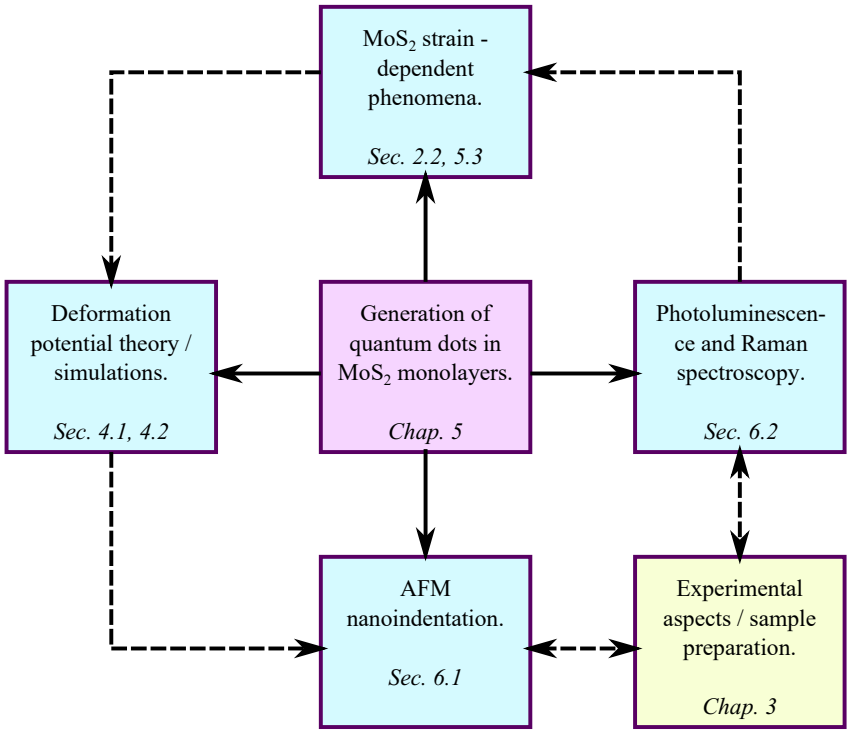

The central discussion and the hypothesis of generation of quantum dots in MoS_2 monolayers is found in Chapter 5. The hypothesis is supported by four important aspects which are closely-related among them: the review strain-dependent phenomena (Section 2.2, 5.3), the theoretical background based on the deformation potential theory and finite-element simulations (Sections 4.1 and 4.2), the physical realization of the quantum dots using AFM nanoindentation (Section 6.1) and the characterization of the quantum dots via photoluminescence and Raman spectroscopy (Section 6.2). The generation and characterization are in turn supported by the experimental details of the preparation of the samples in the Chapter 3.

PART I

MOS_2

CHAPTER 1

MOS_2 AND 2D MATERIALS

Molybdenum disulfide (MoS_2) is part of the family of the *transition metal dichalcogenides* (TMDs) which consist on molecules of the type MX_2, where M is the transition metal and X is a chalcogen atom. Other common examples of TMDs are WS_2, $MoSe_2$, WSe_2, $MoTe_2$, etc. All of them share along with graphene the property of being *layered*, that is, they are composed of sucessive layers which are held together by weakly attractive Van der Waals forces. This feature enables the obtaining of atomically thin layers, which give rise to different electrical, optical and mechanical phenomena than that of their bulk counterpart. MoS_2 and other TMDs have attracted a great interest recently [24] because of their potential applications in 2D devices such as transistors [25, 26], memories and logic gates [27], gas sensors [2], photodetectors [28], solar cells [29], single-photon sources and Bose-Einstein condensates [30] and many others.

MoS_2 is found in nature in its solid form called *molybdenite*, which is silvery black and similar in appearance to graphite. Molybdenite (See Figure 1.1) is also the most common ore of molybdenum and despite the fact that being carbon its major contaminant, MoS_2 is considered as nonreactive. Its low friction coefficient makes it very useful as a dry lubricant [31]; similarly to graphene, MoS_2 can be added to plastics to improve their strength and reduce friction [32]. MoS_2 is also used as a catalyst in a wide variety of reactions in petrochemistry and some organic synthesis, for example, in the hydrogen evolution, and the electrolysis of water [17]. All these properties were well-known and used even much before the achievement

Figure 1.1 MoS2: The compound *molybdenite* is the main ore of molybdenum.

of its bidimensional form, then MoS_2 among the other TMDs has been favoured with a high interest along the past decades.

Before their bidimensional forms were explored, some studies based on band structure calculations since the 1970s addressed the atomically thin TMDs [33], and in the late 1990s the study of the bands of MoS_2 nanotubes revealed an important feature of these nanostructures: the emergence of a direct band gap when reducing the thickness of the material to the atomic scale [34].

All TMDs display a transition between indirect band gap in the bulk to direct in the monolayer, which is a great advantage for applications in optoelectronics. Additionally, a monolayer TMD crystal has a new degree of freedom called the *k-valley index* due to the lack of inversion center: this leads to the birth of a new research area, the *valleytronics*, which consists on the manipulation of the valley index of charge carriers to create quantum bits of information. One of the reasons why TMDs and in general all 2D materials are successful, is the relatively easy fabrication of samples and devices. In the next section we will review the main ways to prepare MoS_2 monolayer samples.

1.1 Achieving the MoS_2 monolayer

There exist some techniques to obtain atomically thin MoS_2, each one suitable for a different need. For example, characterization of electrical and optical properties requires a sample with highly pure, pristine and clean structure [35]. Mechanical exfoliation is a technique in which atomically layers of a material are separated from the material with the help of an adhesive tape. It gives one of the most clean and pristine samples, nevertheless it is not suitable for practical applications at large scale because of the disadvantages in controlling the sheet size and layer number [36]. Other techniques aspire to satisfy these requirements, such as *chemical exfoliation (CE)* and *chemical vapour deposition (CVD)* synthesis. CE uses solvents such as lithium ions to create intercalation of Li and MoS_2 sheets which are then sonicated in order to isolate the sheets. CE allows us to increase the production of

monolayer flakes, but the sonication process causes crystalline defects and reduces the size of the flake, limiting the technical applications.

CVD is a set of techniques in which deposition of Mo and S atoms, and chemical reactions or nucleation processes, are present. The most common is the sulfurization of Mo or Mo-based oxides: a thin film of Mo is deposited on SiO_2 by *electron beam evaporation* and then it is put to react with S vapour in a furnace at 750°C [37, 38]. Other CVD technique is based on the reaction of solid MoO_3 and S powders on a SiO_2 substrate at room temperature [2]. CVD allows us to obtain large-area monolayers, but the strong interaction with the substrate and the large density of defects affect both electronic and optic properties, and make this technique unsuitable for fundamental research [39, 40].

Another, lesser common, technique for growing TMDs is based on the *molecular beam epitaxy* [41], in which pure Mo and S are heated and sublimated, then the vapor generated condenses on a SiC wafer. The resulting compound grows as a structure in which the sucessive layers are weakly interacting through van der Waals forces, reason why this technique is also called the *Van der Waals epitaxial growth* and preserves most of the characteristics of mecanically exfoliated MoS_2 [42].

Summarizing, the distinct techniques to obtain atomically thin layers of MoS_2 are adjusted to the necessities of the research: from pristine-mechanically exfoliated monolayers for the study of fundamental properties of MoS_2 to the large-area flakes generated via CVD that are suitable to build devices, solar funnels and field-effect transistors. These techniques may also be combined to achieve very specific scenarios such as sonicated graphene on exfoliated MoS_2, generating quantum dots and so on. To achieve the main goal of this work, we used the mechanical exfoliation over polymer substrates to achieve the most convenient conditions to perform AFM nanoindentation. In the next chapter we will review other important features of MoS_2 that will help us to understand the physics of the nanoindentation and the generation of quantum dots via strain.

CHAPTER 2

FEATURES OF THE MOS_2 MONOLAYER

As stated in Chapter 1, the MoS_2 molecule is composed by two sulfur atoms that are covalently bound to a molybdenum atom. When packed together, MoS_2 molecules form the crystalline structure of an atomic layer, which is not "strictly" atomic (Figure 2.1 (a)) due to the vertical separation of the two S atoms in each site. The top view shows that the structure is that of a honeycomb lattice (Figure 2.1 (b)), the same as that of grahpene, in which the unit cell is composed of two sites (one molybdenum at one and two sulfurs at the other) resulting in a triangular Bravais lattice of parameter $a = 3.16$ Å. The two lattice vectors can be written as $\mathbf{a}_1 = \frac{a}{2}(1, \sqrt{3})$, $a_2 = \frac{a}{2}(1, -\sqrt{3})$.

Two sucessive layers are stacked with the Mo center of the upper layer right above the S of the lower layer, with their unit cells inverted with respect to each other, where $c = 12.58$ Å. The Brillouin zone of the honeycomb lattice is another hexagonal lattice with reciprocal lattice vectors $\mathbf{b}_1 = \frac{2\pi}{a}(1, \frac{1}{\sqrt{3}})$, $\mathbf{b}_2 = \frac{2\pi}{a}(1, -\frac{1}{\sqrt{3}})$. The Brillouin zone is sketched in Figure 2.2(a): it shows the high symmetry points of an hexagon, which are the Γ, M, M', K and K' points. In the next section we will discuss the actual importance of these symmetry points and how they are related to the electronic or mechanical properties of the material.

2.1 Electronic properties

The electronic configuration of Mo ($4d^5 5s^1$) tells us that there are six valence electrons in the d shell. On the other hand, the electronic configuration of S ($3s^2 3p^4$)

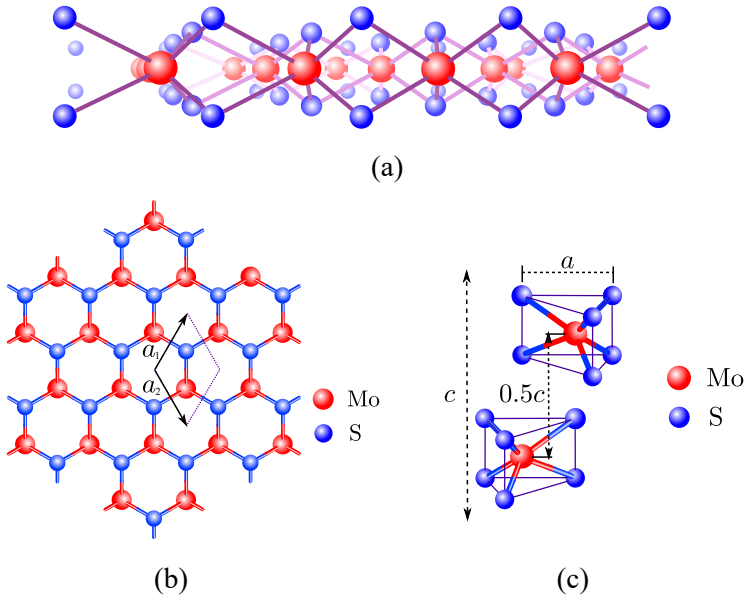

Figure 2.1 Structure of MoS_2: (a) monolayer side view, (b) monolayer top view and (c) unit cell and bilayer stacking.

displays other six valence electrons in the p shell: in order to satisfy the octet rule, two additional electrons are needed in the Mo site, thus MoS_2 is a negatively doped semiconductor. We will see later how this fact is manifested in the photoluminescence spectrum. The covalent σ bonds between Mo and S atoms are made of hybridized p and s states, and the weak π bonds are responsible for the interlayer coupling [1]. One of the properties of transition metals is their strong *spin-orbital coupling* (SOC) due to their relatively high mass. We also expect that the SOC will originate a large spin-orbit splitting (SOS), which is proportional to $\frac{1}{r}\frac{dV(r)}{dr}\mathbf{L}\cdot\mathbf{S}$, where $V(r)$ is the Coulomb potential of the Mo valence electrons, $\mathbf{L}$ and $\mathbf{S}$ their angular momenta and spin, respectively. SOS in MoS_2 is approximately 100 meV.

When studying the electronics of the crystal, a fundamental issue emerges: we need to describe a wavefunction which depends on the 3N coordinates of the many-electron problem, which becomes a computationally impossible task when the number N of electrons tend to the thermodynamic limit. Beyond the Hartree-Fock approximation, the so-called *density functional theory* (DFT) in the *local density approximation* (LDA) gives us an accurate description of the ground state of the electrons at the different bands of the crystal [43, 44].

Symmetry provides helpful information about the degeneracies and states close to the band edges [2]. As most of the optical phenomena involves direct-gap transitions at the K point of the Brillouin zone, the Mo-d orbitals can be divided in three *irreducible representations*: $A'(d_{z^2})$, $E'_1(d_{xy}, d_{x^2-y^2})$ and $E''(d_{xz}, d_{yz})$; in the

[1] The covalent σ bonds lie within the plane of the lattice and are responsible of most of the elastic properties of the monolayer, while the π bonds represent the weak Van der Waals interlayer coupling.

[2] A formalism based on group theory and irreducible representations for the dependence of the observables on the crystal symmetry has been extensively reviewed in the literature [45].

monolayer limit, reflection symmetry σ_h only allows the hybridization between A' and E'_1 orbitals. To determine the weight of each orbital at the band edges and what is the band structure itself, DFT *ab initio* calculations have to be performed. Figure 2.2 (b)-(c) shows the density of states (DOS) and the electronic band structure for spin up (red lines) and spin down (blue lines). A study of the DOS reveals that the states at the bottom of conduction band are mostly projected on the Mo d_{z^2} orbital and secondarily on the S p_x, p_y orbitals, while the states at the top of valence band are mostly Mo $d_{x^2-y^2}, d_{xy}$ and in a lesser proportion are S p_x, p_y orbitals.

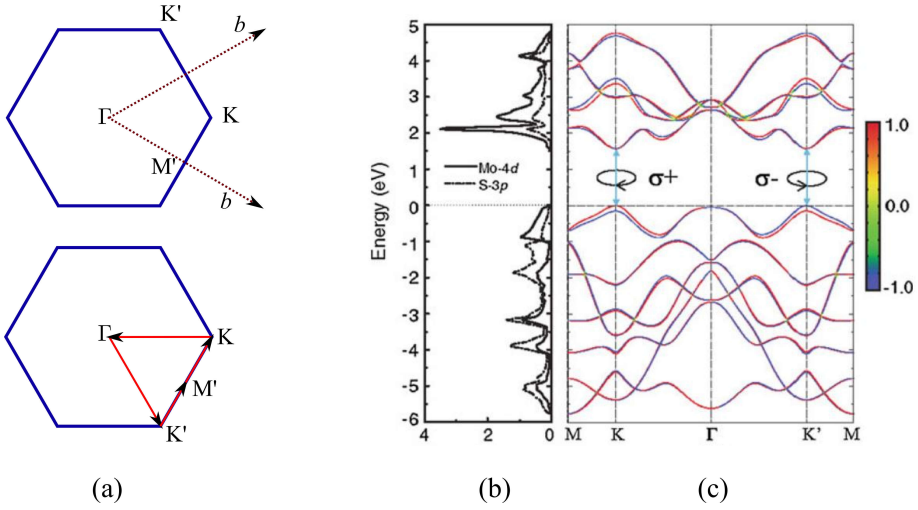

Figure 2.2 Color online. Electronic band structure of MoS_2 monolayer, (a) Brillouin zone and the path along which the bands are calculated, (b) the density of states and (c) the band structure with the projection of spin operator J_z. Partially extracted from [46].

The band structure shows the direct band gap opening in the K, K' points, which is due to the lack of the inversion symmetry of the monolayer, as seen in Figure 2.2 (c). The SOS of the valence band (VB) is much larger than that of the conduction band (CB), and have opposite sign for each K or K' points: this phenomenon in which the spin [3] of the electron at the top of VB (TVB) is coupled to the valley index of the bottom CB (BCB) is called the *spin-valley coupling* [47] [4]. In Figure 2.2 (c) note that the TVB electron spin is 3/2 at the K point, and 1/2 at the K' point: this tells us that the polarization of light, the valley and the electron spin are mutually coupled. We are able to control the population of each valley by exciting the material with either σ^+ or σ^- light. In the next sections we describe other mechanical, excitonic and optical properties of MoS_2.

[3]When we are referred to the *spin* of an electron in the electronic band structure, we are actually speaking about the total angular momentum J, J_z, which is defined for each band.

[4]The light emitted from an optical transition is circularly polarized (we denote the polarization of the light as σ^+ for right-polarization and σ^- for left-polarized) due to the *optical selection rules*: the change in the angular momentum of the electron in the transition must be $\Delta L = \pm 1$, which is the angular momentum $\sigma^\pm$ of the photon emited

2.2 Mechanical and vibrational properties

One of the more interesting properties of MoS_2 is its high hardness, despite of its apparently fragile layered structure. Furthermore, the gap is highly sensitive to strain variations: a semiconductor-to-semimetal transition occurs at $\sim$30% of tensile strain [48].

Bulk molybdenum disulfide has a Young's modulus 330 GPa, which is softer than graphene (1050 GPa), but stiffer than steel (200 GPa). The in-plane stiffness is reported to be 120.1 N/m [5, 49]. We need to exert a tension on MoS_2 in order to study its mechanical properties; one way is by uniaxial stretching as shown in Figure 2.3 (a), in which a rod which descends horizontally makes the membrane be stretched in one direction. The honeycomb lattice has the same elastic properties than that of an isotropic 2D material, reason why the uniaxial strain in the *armchair* and the *zig-zag* directions is the same for a given force load. The other way is to stretch in both directions at the same time via *nanoindentation*, Figure 2.3 (b); this can be done[5] using an AFM probe in contact mode with a force load of several nN.

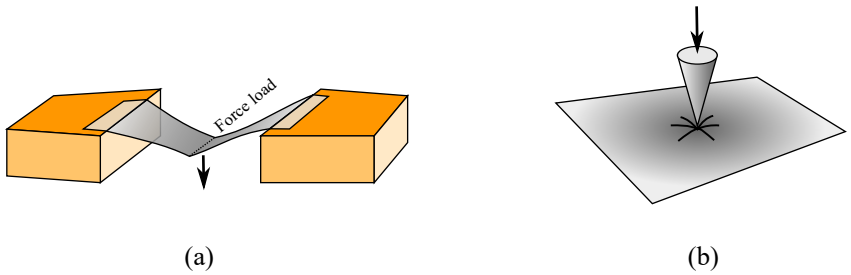

Figure 2.3 Two ways to stretch membranes to study (a) uniaxial or (b) biaxial strain.

Now, we will talk about another mechanical feature of MoS_2 and of every solid in general: a property that concerns to the lattice vibrations, or *phonons*. These vibrations form a field which can propagate along the material as plane waves, whose wavevector and frequency are related to each other through the *dispersion relation*, $\omega(k)$. The modes of lattice vibrations can be either optical or acoustical depending on the coupling of the mode to the light waves at the Γ point. The vibration field of these modes propagate along the crystal with a finite group velocity $v_g = \partial\omega/\partial k$. In most of the known solids, the optical modes are active in the infrared (IR) and visible (red, R) [45]. Figure 2.4 shows the dispersion relation of phonons in MoS_2 monolayer and their calculated density of states. This information is also provided by ab initio calculations, in which the lattice parameter, the angle between Mo-S bonds and the layer thickness are found in such a way that minimizes the elastic energy of the lattice; then the modes are studied [50].

When light strikes the surface of a material, it is either elastically or inelastically scattered at very specific frequencies which correspond to the excitation of phonon modes, since the law of conservation of momentum is satisfied. Inelastic scattering of light involves the creation of phonons of very small wavevectors (compared to

[5]The strain in an uniaxial deformation of MoS_2 has proven to be the same in the zig-zag and armchair directions [1].

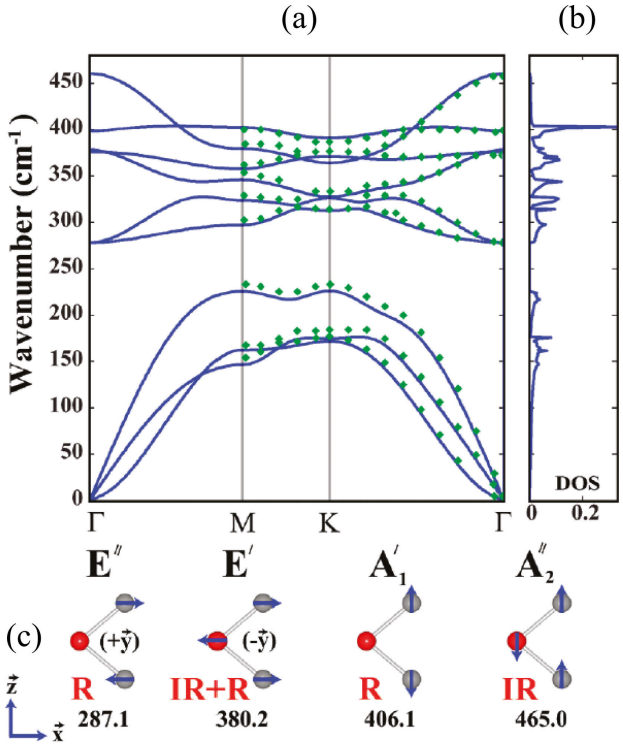

Figure 2.4 Dispersion relation of phonon modes for MoS_2 monolayer, (a) as calculated, (b) the corresponding density of states and (c) depiction of the optically active phonon modes. Extracted from [51].

that of electrons), normally between 280 cm^{-1} and 470 cm^{-1} for ultrathin MoS_2 [52]. Figure 2.4 (c) depicts the motion of each one of the optical phonon modes of the monolayer. The most representative optically active modes in the *Raman spectrum* are the longitudinal E' and the transversal A'_1, because they offer to us an accurate identification of the number of layers of the material [53], see Figure 2.5. The separation between E' and A'_1 peaks for a monolayer is ~ 18.5 cm^{-1}; for bulk the separation of the E^1_{2g} and A_{1g} raises to 25 cm^{-1}. Besides, Raman shift could serve as an indicator of the strain of the monolayer, since the strain affects the average bond length and the frequency of each mode, then it may also change the phonon energy. In the next section, we review the optical properties of MoS_2, which are somehow related to the Raman spectrum, in the sense that we study the way that light is scattered by or interacts with a substance.

2.3 Optical properties

The optical processes which involve both light and matter are refraction, scattering, absorption and luminescence. Then it is fundamental to study these processes to understand the optical behavior of materials. For instance, the refractive index gives the velocity of light through the medium and the transmission amplitude, which are very important factors to consider in the identification of atomically thin MoS_2 by optical contrast: the thicker the film, the more contrast with the substrate we will

see. The refractive index is usually a complex and wavelength-dependent quantity whose real part is related to the optical polarizability ($\varepsilon_r \approx 4.5$ for $\lambda = 650$ nm) and the imaginary part is related to the absorbance. The absorption as a function of the frequency of the light is called the *absorption spectrum*, and is shown in Figure 2.6. The absorption of the monolayer and the bilayer is characterized by two lines at 1.85 eV and 2.1 eV that correspond to the exciton A and B absorption, respectively. Additionally, as increasing the energy, more states of the are accessible and the absorption tends to increase. Figure 2.6 shows the photoluminescence of both the monolayer and bilayer (red solid lines); in which the bilayer spectrum displays three peaks corresponding to the indirect gap recombination (that will be explained later) and the exciton A and B emission. In contrast, the photoluminescence of the monolayer is characterized by the absence of the indirect band gap recombination.

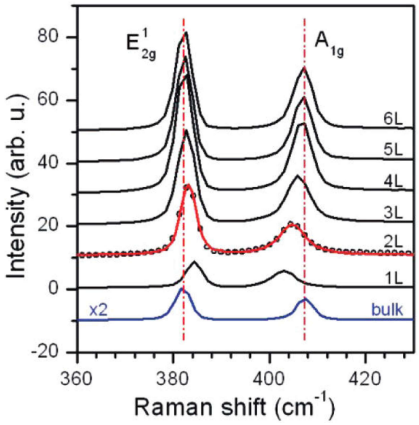

Figure 2.5 Raman spectra for MoS_2 few layers and bulk. Extracted from [54].

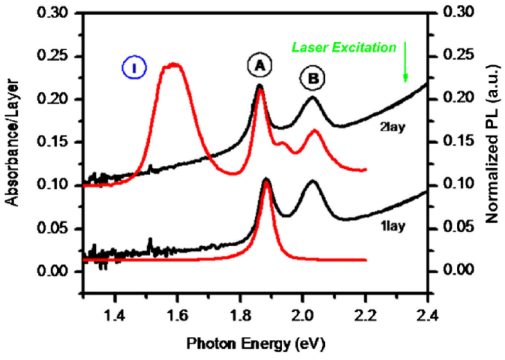

Figure 2.6 Absorbance spectrum (black solid line) and photoluminescence (red solid line) for one- and bi-layer MoS_2. Extracted from [12].

The transition rate in absorption processes are described by the *Fermi's golden rule* [55], which states that the amplitude of the transition between two states labeled as i and f is

$$W_{i\to j} = \frac{2\pi}{\hbar}|M|^2 g(\hbar\omega), \tag{2.1}$$

where $\hbar$ is the reduced Planck's constant, M is the element of the matrix which describes the light-matter interaction, and $g(\hbar\omega)$ the DOS evaluated at the photon energy $\hbar\omega$. For most materials, the nature of the interaction is dipolar, in which

$$M = \langle f|(-\mathbf{p}\cdot\mathscr{E}(\mathbf{r}))|i\rangle, \tag{2.2}$$

where $\mathbf{p}$ is the electric dipole moment $-e\mathbf{r}$ and $\mathscr{E}(\mathbf{r})$ the electric field at $\mathbf{r}$. As the photon momentum is very small compared to typical electronic momentum, the conservation law establishes that $\mathbf{k}_i = \mathbf{k}_f$ for the initial and final momenta, thus the absorption processes involve a *direct transition*. The DOS near to the TVB or BCB for a 2D material in the *effective mass approximation* is

$$g(E) = \frac{1}{4\pi}\left(\frac{2m^*}{\hbar^2}\right), \tag{2.3}$$

where m^* is the effective mass of the electron. Until now we have described the optical absorption process labeled as A in Figure 2.7: an electron from VB is "vertically" promoted to CB via laser excitation, leaving a *hole* behind it. Then the carriers relax to the bottom of CB, as shown in process B. The diference between the parts (a) and (b) of Figure 2.7 is that the bottom of CB is located at different positions in the reciprocal space; this will give rise to a *direct gap recombination* for (a) and an *indirect gap recombination*. For (a), a photon is emitted without perturbing the crystal; for (b), a photon of momentum q is created in the lattice, as described by process C. The whole process is known as *photoluminescence* (PL): luminescence is defined as any process of emission of light from a substance, and photoluminescence is the luminescence but restricted to the case when the excitation is performed optically.

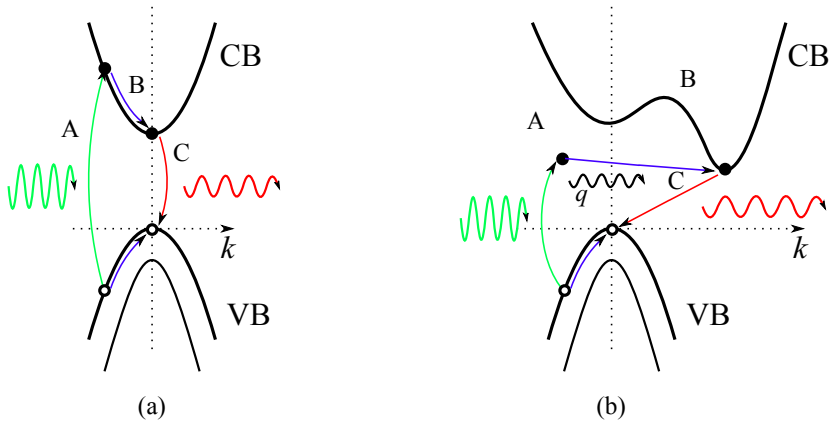

Figure 2.7 Optical transitions in MoS_2 for (a) direct and (b) for indirect bandgap recombination.

As MoS_2 is found to be an indirect band gap ($\sim$1.2 eV) semiconductor from the bilayer to the bulk form, its PL is very weak (see Figure 2.6) due to the inefficient process of luminescent recombination, then the main mechanism of relaxation is through phonon-assisted emission. PL is only enhanced in the monolayer form, in which the CB electrons relax in the points K or K' that correspond to a direct transition. Treatment of direct gap recombination in TMDs has to be very careful because the transition does not occur at the bare gap energy; the electron and hole of each band interact very strongly between them forming an exciton, then the PL occurs at a lower energy than the band gap [56]. Moreover, the PL spectrum is composed of several broad peaks which come not only from the neutral exciton recombination, but also from the negatively charged exciton recombination; these features will be addressed in the next section as well as in Chapter 4.

2.4 Excitonic properties

When an electron reaches the conduction band, it remains there for a few ps until it relaxes to the BCB and recombines with the corresponding hole. While the electron is in the CB, the resulting picture is that of a state of two particles bound by a Coulomb interaction: the *exciton*. In bulk semiconductors, excitons can move freely through the material for a lifetime; such lifetime is mainly limited by both the radiative and the non-radiative decay rates in the exciton. The non-radiative decay can occur in several pathways such as Auger recombination, electron-phonon relaxation, or by trapping in defects of the material, [57, 58].

Because of the electron-hole binding energy, the excitonic states lie within the band gap, but this phenomenon is strongly dependent on the dimensionality (which causes electron confinement) and the structure of the material in which they are formed. For instance, there are two kinds of excitons in semiconductors and insulators: the *Wannier-Mott* (WM) exciton and the *Frenkel* (F) exciton. The first ones are the usual excitons found in non-organic semiconductors (GaAs, for instance) and the second ones in organic semiconductors or molecular crystals. Altough WM excitons are much more common in the nowadays semiconductor-based technology, the concept of exciton came first with the idea of excitation waves in organic molecules by Frenkel (1931) [59]. Narrow and intense lines in the spectra from these molecules were seen in the late 1920s. Large molecular separation in these crystals impedes the overlap between intermolecular electron wavefunctions, thus the electron-hole pair remains tightly bound to each site. Typical Bohr radius of Frenkel excitons are of the order of the lattice constant and the binding energy is $\sim 0.1 - 1$ eV [60].

The term Wannier-Mott exciton was coined in the late 1930s for materials in which the eletron wavefunction extends over several lattice sites, thus the hopping energy between any two adjacent crystal cells exceeds the exciton Coulomb-binding energy [61]. Unlike Frenkel excitons, Wannier-Mott excitons have a small binding energy of a few meV and typical sizes of several tens of lattice constants. Nonetheless, there may exist certain regimes in which the Wannier-Mott and Frenkel excitons share their features. The concept of hybrid Frenkel-Wannier-Mott excitons which could combine both large binding energies and relatively large size was introduced in the late 1990s [62]. Excitons in MoS_2 atomic monolayers are suspect to be Frenkel-Wannier-Mott ones [22] and could manifest attractive features such as strong exciton confinement [63], single-photon emission [64] and wide-spectrum solar energy harvesting [22]. Probably one of the most remarkable properties of Frenkel excitons is that excitons may be created and recombined at room conditions because the thermal fluctuations in this regime are not sufficient to dissociate the highly bound excitons.

The exciton in MoS_2 2D monolayer has to be carefully treated since the molybdenum disulfide molecule is noncentrosymmetric, then the transitions at K and K' points are correlated to the electron spin. Furthermore, excitons have been predicted theoretically to have both large Bohr radius and large exciton binding energy. The splitting from the spin-orbit coupling allows the creation of two different types

of exciton: the exciton A and B. The energy of the optical recombination between a CB electron and a hole in the lower VB at the K point is greater than that of a recombination with a hole in the upper VB; the first is known as *exciton B emission*, while the second is the *exciton A emission*, as shown in Figure 2.8. Exciton B emission occurs typically at 624 nm (1.98 eV) and is usually less intense than the exciton A emission, which occurs at 665 nm (1.86 eV). The reason for B emission being less intense than A is that the holes at VB tend to occupy the lower energy states, i.e. at the top of the valence band, making the recombination to the lower valence band be less probable.

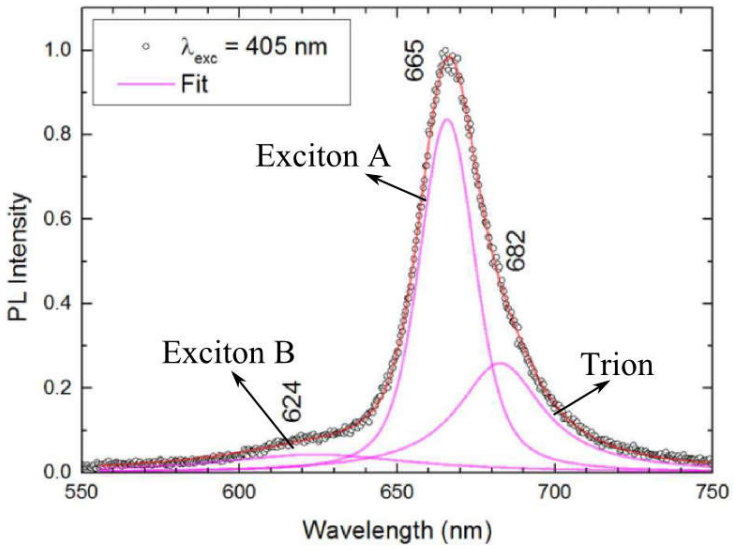

Figure 2.8 Photoluminescence spectrum of the MoS_2 monolayer displaying the different features of the excitonic emission. From [65].

Despite the fact of MoS_2 being an electrically neutral material, at room temperatures there exists a certain population of electrons in the conduction band even before the creation of an electron-hole pair. These electrons can interact with the hole at VB, forming a three-body bound system called the *negatively charged exciton* or *trion*. As there are two electrons coupled to the same hole, the binding energy of the additional electron in the trion (~ 20 meV) is significantly lower than that of the neutral exciton; then we expect for the PL spectrum two peaks separated by ~ 20 meV around 1.85 eV [66], as shown in Figure 2.8. As the width of the neutral exciton line is about 60 meV, we actually observe a composite line instead of two separated peaks. The respective weights of the charged and neutral excitons in the PL can be controlled through a gate voltage [67, 68], but also depends on the temperature since the thermal fluctuations at 300 K are comparable to the trion binding energy and favor the population of negatively charged excitons in the material. Besides, the substrate may affect the electron population at the CB due to additional doping of the material and also modify the weights of the emission of neutral and charged excitons in the PL. In Chapter 4 we discuss theoretically the excitons in a strain field by the combination of DFT-LDA and $k \cdot p$ theories.

CHAPTER 3

SAMPLE PREPARATION AND CHARACTERIZATION - EXPERIMENTAL DETAILS

Generation of quantum dots in monolayer MoS_2 involves a set of experimental techniques which range from the creation of the samples to advanced measurement techniques to characterize and identify the QDs. For the creation of the samples we have to consider both a substrate with the suitable elastic-plastic properties that allow us to generate deterministically the indentations and a pristine 2D crystal of MoS_2 to observe only the phenomena associated to strain. As stated in Chapter 1, mechanical exfoliation is the best method to study our fundamental problem. In the next section we will provide details on the fabrication of the samples.

3.1 Mechanical exfoliation on polymer substrates

We choose organic compounds to serve as a substrate to perform the indentations because they have a broad regime in which they behave elastically and undergo a soft transition to a plastic regime [69]. Methyl metacrilate (MMA) and Polymethyl metacrilate (PMMA) were considered.

3.1.1 MMA and PMMA spin coating

MMA and PMMA spin-coatings were performed on a hard substrate which consists of a 300 nm-thickness SiO_2 layer on a 0.7 mm thickness Si wafer. After a 4000 rpm cleaning with isopropyl alcohol and acetone in the spinner, the wafers were blown with N_2 to dry the residuals of acetone, then 50 μl of the polymer were deposited onto the 100 rpm-rotating wafer. The next step in the program varied whether we

were using either PMMA or MMA; for example, for MMA we used 4000 rpm for 30 s and then lowered the velocity to 1500 rpm for 30 s. This gave the most uniform and flat film of MMA ($\sim$ 100 nm thickness). Moreover, for PMMA we 3800 rpm for 80 s and then lowered the velocity to 1000 rpm for 30 s; this gives a $\sim$200 nm thickness for the film. Then the wafers were taken to the hot plate with an initial temperature of 60 °C, with increments of 40 °C every 3 minutes until 220 °C. The reason of this is that we experienced bubble formation in the film ($\sim$ 200 nm - 300 nm diameter bubles) probably due to a sudden heating when putting the wafer directly on a 220 °C plate.

3.1.2 Mechanical exfoliation

We may define a quantifier called the *difficulty of exfoliation* as the inverse of the number of monolayer flakes of >5 μm size over the total number of monolayer flakes. In this sense, it is more difficult to exfoliate over a high-molecular weight polymer than over a low one, since initially we always found a larger number of tiny monolayer flakes for 950K-C4 PMMA than for 450K-C2 PMMA and for MMA. The reason for that is that MMA and 450K PMMA are more viscous than 950K PMMA and thus they are more adhesive to the contact with MoS_2[1]. That means that if we need to use 950K PMMA as a substrate, then we have to develop a particular exfoliation technique by adjusting several details in the process.

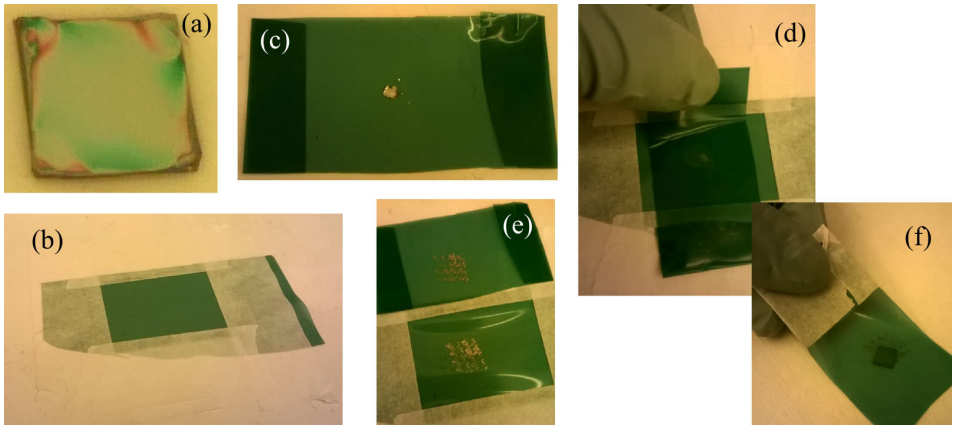

Figure 3.1 Mechanical exfoliation of MoS2 over PMMA substrate: (a) PMMA spin-coated wafer, (b) scotch-tape fixed to the table, (c) MoS_2 seed in tape, (d) transferring the MoS_2 seed to the fixed tape, (e) result of the exfoliation and (f) transference to the wafer.

We used commercial MoS_2 (from "SPI Supplies") for all our experiments. Figure 3.1 (a) shows a typical 1 cm^2 spin-coated substrate. The details on a typical exfoliation were performed as follows: (b), one scotch tape piece was fixed to the table with masking tape to avoid shear stresses when sticking and unsticking the tapes; (c) the MoS_2 flake was placed over the freestanding tape. In (d) we gen-

[1]Molecular weight is an adimensional quantity that expresses the weight of a molecule. Two polymers of different molecular weights will have different mechanical or thermal properties are also different. In our work we name the polymer 450K as a polymer of molecular weight of 450,000

tly put one tape against the other to let them scarcely be in contact and then pull the upper tape. We usually repeat (d) three to four times and obtain (e). In (f) we put the tape face down to the substrate without touching it directly with the fingers and then we blow it with pressurized N_2. This method improves the flake size of monolayer MoS_2 on 950K PMMA by 200% (with respect to conventional recipes of exfoliation), and consequently, reduces the difficulty of exfoliation for this substrate.

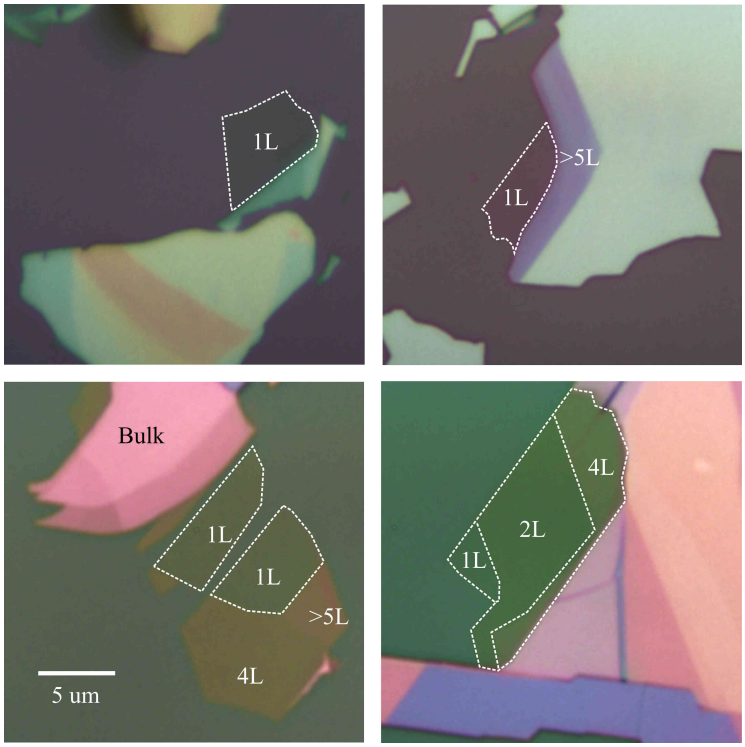

Figure 3.2 Monolayer MoS_2 on PMMA optical images, showing each one different flakes and different optical contrast with the substrate. 1L, 2L, 3L... stand for mono-, bi-, tri-layer and so on.

Optical contrast can be ambiguous to identify MoS_2 monolayers when the atomically thin material is exfoliated on a (almost uniform) thin film. Figure 3.2 shows four monolayers found along the same PMMA sample: note that the color of the substrate is not the same. In general, the greenish substrates mean thicker PMMA films than the purplish or the reddish. Nevertheless, we found that there is a correlation between the monolayer color/contrast and the color of the film: Purple films give high-contrasted greenish monolayer flakes, while green films give poor-contrasted yellowish monolayer flakes.

3.2 AFM topography - nanoindentation

Atomic force spectroscopy (AFM) is a wide spread scanning-probe microscopy technique that allows imaging the topography of a surface with atomic resolution [70]. It consists of a probe with a very sharp tip of 2 nm - 10 nm radius at the apex

in a cantilever of a few hundred micrometers length. Forces between the surface and the tip emerge when mutually approached: this results in a deflection of the cantilever which can be measured by optical means. Then using a fine piezoelectric positioner, the probe sweeps a given area and allows a computer to form an image of the surface. AFM can operate in various modes, among them we find: *contact mode* (CM) and *non-contact mode* (NCM). In CM, the tip is approached to the sample until it reaches a distance of the order of the interatomic distances, then the repulsive forces from the electronic clouds become relevant and we can scan with ultra-high resolution or even manipulate the surface (See Figure 3.3) [71, 72].

The parameter that is monitored in CM is the cantilever deflection, also called the *setpoint* [71]. For small deformations the cantilever behaves as a spring with frequency of resonance ω_0 and the Hooke's law $F = -k\Delta x$ applies. As the deflection in AFM is usually given in units of voltage, then the bending of the cantilever must be characterized by a *sensiblity* s which relates the voltage applied ΔV to the total deformation of the cantilever, then $F = -k\Delta V/s$.

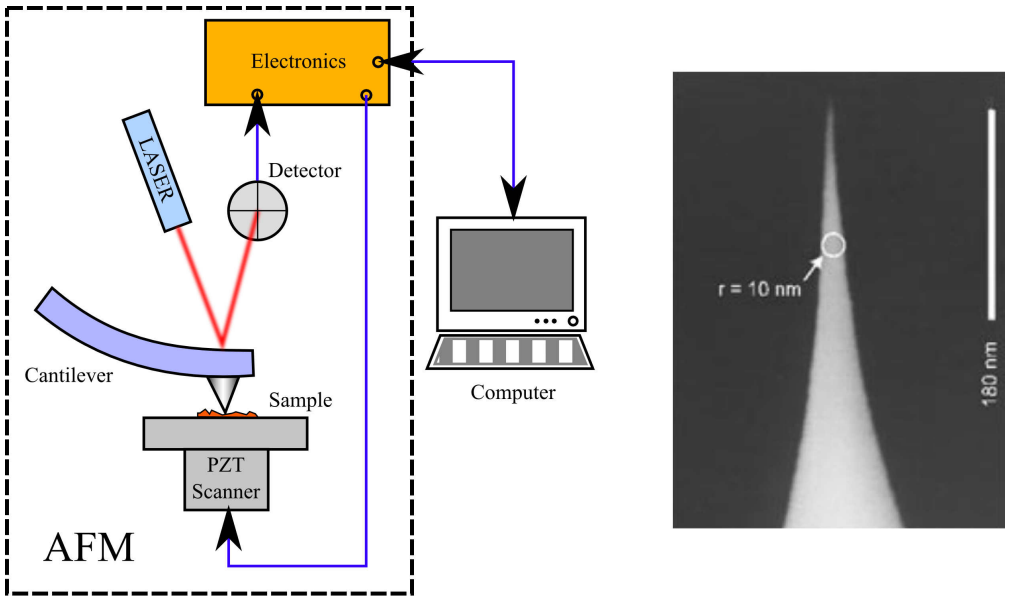

(a) (b)

Figure 3.3 AFM. (a) Diagram of working in the contact mode. (b) Scanning electron microscoy of a typical probe used in our indentations. Extracted from [59]

The NCM works with distances which range from 1 nm to 10 nm to study samples which are very soft or at risk of being damaged. The resolution is limited to several tens of nanometers [71, 72]. The feedback system makes NCM work at a constant distance to the surface, then the electronics is able to monitor either the cantilever's amplitude or frequency of resonance.

CM is needed to perform nanoindentations on MoS_2. Additionally, a very sharp probe with a low-elastic constant cantilever are necessary, therefore we chose the *SuperSharpSilicon™ - Non-Contact / Tapping mode - High Resonance Frequency*

- *Reflex Coating* (SSR-NCHR) from the fabricant NANOSENSORS™ [65]. This probe has a typical radius of curvature of 2 nm at the tip and a half-cone angle of the apex $<10°$; the cantilever has a thickness of 4 μm, a spring constant of $\sim$42 N/m and a resonance frequency of 330 kHz.

Before the characterization of the topography of the substrate, we made a calibration of the cantilever to know the spring constant based on the *Sader method* [73]. This method uses the length L and width b of the cantilever and the density of air ρ as input information. Additionally a thermal noise spectra is measured on the unloaded AFM cantilever and we fit the response of a Simple Harmonic Oscillator (SHO) with added white noise floor to the amplitude of the unloaded cantilever:

$$A = A_{white} + \frac{A_0 \omega^4}{(\omega^2 - \omega_r^2)^2 + \frac{\omega^2 \omega_r^2}{Q^2}},$$

where ω_r and Q are the fitted resonance frequency and quality factor of the cantilever, respectively. For our tip, the fitted parameters were ω_r=286.19 s^{-1} and Q =337.58. The Sader method relates all these quantities to the spring constant:

$$k = 0.1906 \rho b^2 L Q \omega_r^2 \Gamma_i(\omega_r) = 16.3 \text{ N/m}, \tag{3.1}$$

where Γ_i is the imaginary part of the hydrodynamic function [74]. The sensibility was calculated by putting the tip in contact with a hard substrate (SiO_2) and calculate the bare deflection of the cantilever as a function of the setpoint voltage. The process is shown in Figure 3.4: the load is represented by the ABC red curve, and the unload by the DEF curve. The slope is equal to the sensibility and the discontinuities at B, E correspond to the attractive force experienced by the tip just before touching the surface and the adhesive force due to the water meniscus which is formed via capillarity, respectively. This method yields s =67.339 V/μm. By using these concepts, in the next section we will study the plastic behavior of PMMA because it may provide an estimate of the shape that will be achieved via nanoindentation on MoS_2.

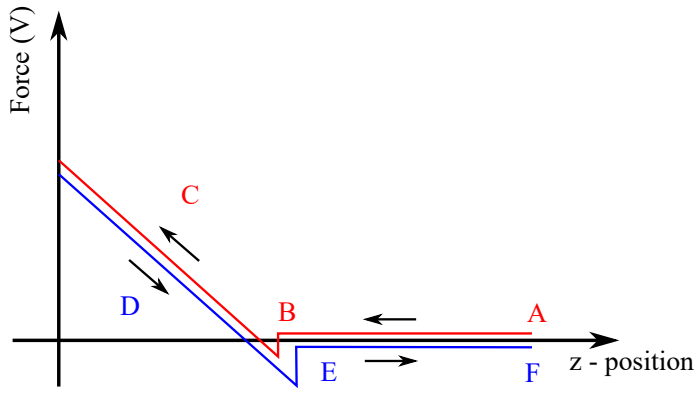

Figure 3.4 Force curve of AFM for nanoindentations. Processes A, B and C (solid red line) describe the load. Processes D, E and F correspond to the unload.

3.2.1 Nanoindentation on plastic PMMA: stress-strain curves

The scheme shown in Figure 3.4 is the same as that of the nanoindentation: the only difference is that the sample is deformable and a net vertical displacement of the tip is added to the deflection of the cantilever. That is, for a given setpoint the total deflection will be greater than the actual displacement of the cantilever (See Figure 3.5): Let h be the total displacement measured in a force curve for a given setpoint ΔV, and also let $\Delta x = \Delta V/s$ be the deflection of the cantilever. Then the *travel* inside the PMMA is $h' = h - \Delta x$ or $h' = h - \Delta V/s$ (See Figure 3.5 (a)). In this sense we can define an "effective plastic sensibility" of the PMMA as $s' = \Delta V/h'$.

EXAMPLE 3.1 Indentation over PMMA

Consider an indentation which yields the force curve of Figure 3.5 (c). The setpoint was 2.6 V and the total displacement of the cantilever was 39.2 nm in the load curve (red). Then the deflection is $\Delta x = 26.7$ nm and the travel distance is $h' = 12.4$ nm and the PMMA sensibility is $s' = 0.14$ V/μm. A statistical averaging over 81 indentations on PMMA at different setpoints yield $s' = (151 \pm 3)$ V/nm. The PMMA sensibility will let us know what is the travel distance for a given setpoint voltage.

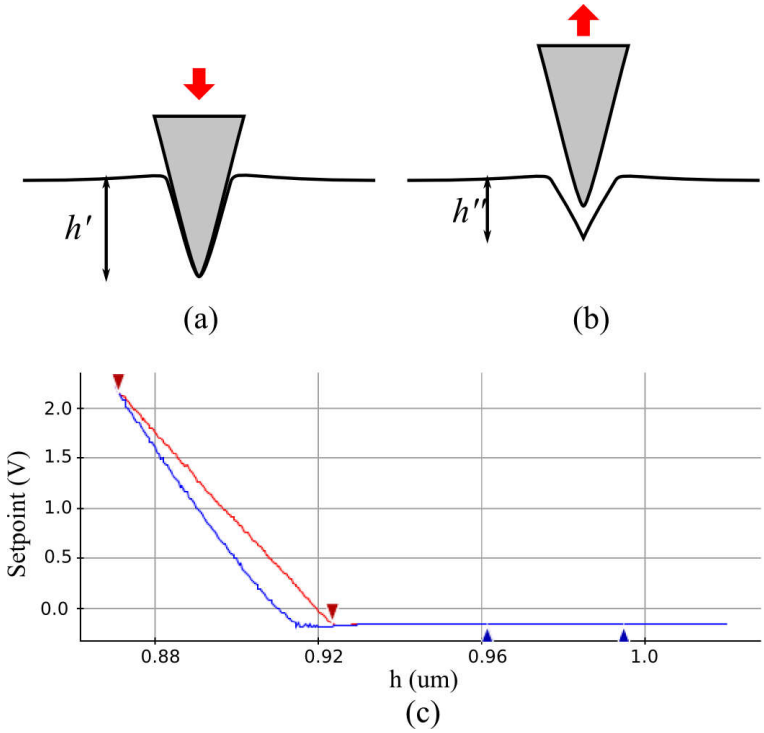

Figure 3.5 Indentation on PMMA. (a) load force (b) unload and (c) the force curve.

The elastoplastic effect of the indentation will make PMMA tend to recover its original shape when the tip is removed. Figure 3.5 (b) plots an indentation reaching

a depth $h'' < h'$. In the roughest approximation we will assume a triangular shape of the nanoindentation, whose strain can be easily calculated as

$$\varepsilon = \frac{\delta l}{l} = 2\left(\frac{h''}{l}\right)^2, \tag{3.2}$$

where l is the width of the indentation. Besides, the stress is equal to the force applied divided by the area of the tip that is in contact with the sample [75]. Provided all this information, now we are able to construct a stress-strain curve which reveals the elastic-plastic behavior of PMMA and gives us an idea of the stress of the sample as a function of the strain, as plotted in Figure 3.6. That figure was obtained from a set of force curves of nearly eighty indentations. This curve reflects most of the plastic behavior of the material, which follows a power-law, while the elastic regime for low strain is approximately linear. The forces (in volts) ranged between 1.8 V and 2.6 V; the fitted curve obtained for the plastic regime was

$$\sigma = 5.155\varepsilon^{0.189}\ [\text{GPa}]. \tag{3.3}$$

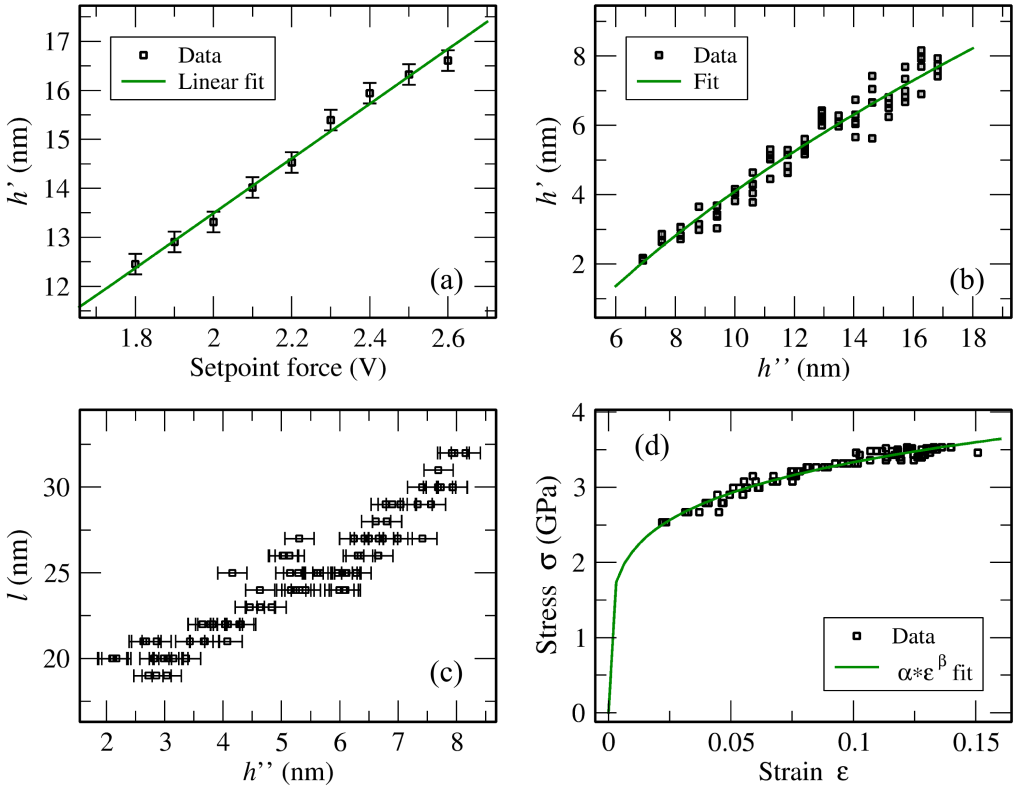

Figure 3.6 Stress-strain curve of indentations on PMMA. (a) shows the maximum indentation depth h' vs. the load force; (b) the correlation between the h' and the final plastic depth h''; (c) the correlation between the indentation width l and the plastic depth and (d) the stress-strain curve.

It can be deduced that PMMA behaves plastically for forces greater than 1.8 V. As MoS_2 has a high in-plane stiffness, then the force needed to stretch it has to be comparable to the value of the stiffness. We may also expect an indentation on

MoS_2 to be much more superficial than that on just PMMA for the same force. The relation between the force of the indenter and the final strain reached will be discussed in further detail in Section 6.1. For now, we will describe other techniques used in the characterization of the vibrational and optical properties of MoS_2, such as the Raman and photoluminescence spectroscopy.

3.3 Raman spectroscopy

The equipment in spectroscopic techniques consists, roughly speaking, of an excitation source, a monochromator and a detector[2]. The monochromator for Raman spectroscopy usually works in the so called triple-mode in which three diffraction gratings are used, giving an effective number of 1800 lines/mm and a high spectral resolution. The scheme of the Raman spectroscopy setup used for our measurements is similar to that of photoluminescence (See Figure 3.7), which will be addressed in the next section: a continuous wave (CW) laser pumping of 488 nm (or 514.5 nm) and 0.4 mW excites the sample through a 100x magnification and 0.94 numerical aperture (NA) objective. Then the signal is collected by the same objective and sent to the monochromator which scatters the different wavelengths and selects the light of an specific wavelength which is detected by a silicon-based charge coupled device (CCD). The CCD operates in temperatures below -120°C, an is usually cooled with liquid nitrogen.

In this work, Raman spectroscopy was used to characterize the number of layers in the flakes. In order to avoid any damage of the sample we used no more than 0.4 mW of excitation, but this resulted simultaneously in a low signal intensity and also low signal-to-noise ratio, reason why we performed three to six acquisitions of sixty seconds each.

The difficulty of properly locating the laser spot in the sample was remedied by the measurement of maps of spectra spread over a region of the flake where we expected to find the indentations. These maps might be composed of points distributed either within a square, along a line, or at random positions. We recall the advantage of possessing a servo-displacer mechanism embedded in the sample holder for this purpose. In the next section we will address other spectroscopic technique that plays a central role in our research and follows a similar scheme to that of Raman spectroscopy: the photoluminescence (PL) spectroscopy. In some cases, it was necessary to use the same equipment to measure both PL and Raman signal, which can be done by making a few adjustments on the gratings of the monochromator.

3.4 Photoluminescence spectroscopy

Similarly to Raman spectroscopy, photoluminescence studies the light which comes from an optically excited sample. The same objective focuses the excitation light on the sample and collects the signal to be measured in the spectrometer. In this

[2]The excitation source for Raman spectroscopy is normally a laser

case, the spectrometer is composed of a single 600 lines/mm and 500 nm blaze diffraction grating. The monochromator used has a length of 55 cm and is operated with a 100 μm-entrance slit[3].

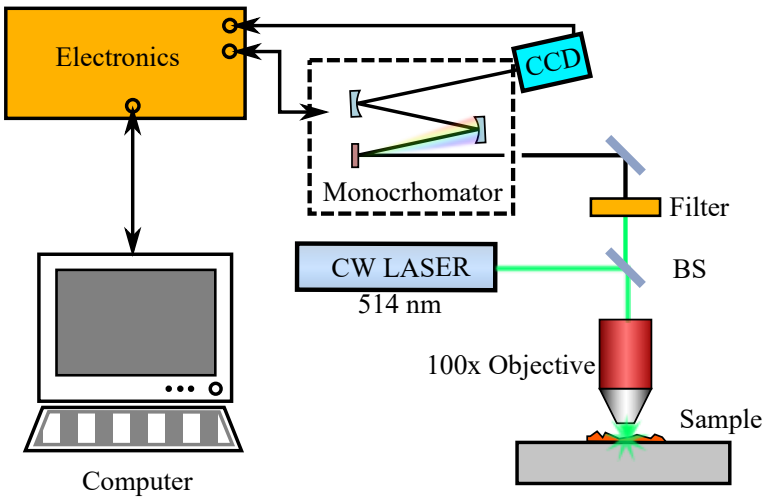

Figure 3.7 Diagram of a setup of photoluminescence spectroscopy operating at room temperature.

The objectives used in the measurements were a 100X 0.49 NA and a 50X 0.49 Mitutoyo lenses, with high ($\sim$20 mm) working distance. This is a suitable condition when the sample has to be inserted in a cryostat for low-temperature measurements. The implementation of this kind of objectives makes the technique be renamed as *micro-PL* (μ-PL) because the laser spot on the sample has a gaussian profile of ~ 1 μm width. The samples were excited with a CW argon solid-state laser of 514 nm wavelength and 0.4 mW - 1.0 mW excitation power. In other measurements, when specified, we used a 488 nm diode laser.

The detectors used were either liquid-nitrogen-cooled or Peltier-based-cooled. In most of the cases the CCD is front illuminated (FI). In other few cases, when specified, they were back illuminated (BI). The main advantage of a BI CCD is that the photosensitive Si layer is directly exposed to the signal, contrary to the FI case in which the polysilicon electrodes go ahead and blocks a portion of the signal[4].

We have described the main aspects of μ-PL, now we will address the types of measurements involving PL spectra. By the number of spectra obtained in a single measurement, we distinguish between *single spectrum* (SS), *spectra along-a-line* (SAL) and *hyperspectrum* (HS).

Single spectrum In this type of spectroscopic technique, we are concerned with all the main features of PL. Here we usually work with long integration times (between 1 - 2 min) and relatively low excitation power (no more than 700 mW) in order to

[3]By reducing the size of the entrance slit we expect to avoid the incoming signal from any other source in the laboratory, because just the signal directed towards the slit should pass through a narrow slit, this should be manifested in a high signal-to-noise ratio.

[4]However, the main disadvantage of BI is that the photosensitive layer displays multiple internal reflections resulting in an *etaloning* of the spectrum, a well-known artifact in spectroscopy. Etaloning is manifested strongly from 800 nm and above, thus it limits the range of wavelengths in which spectra can be measured [76].

avoid sample burning and thermal drift. By using the same parameters in all spectra we may, for instance, measure the ratio of the PL intensities (counts per second) of a monolayer to a bi- or multi-layer. Besides, single spectra are very useful when we need to quickly examine some other features of spectra, such as shifts of the positions of each peak and the broadening/narrowing of the distinct lines.

Spectra along a line SAL consists on a sequence of spectra tightly distributed along a line in a region of the sample. The number of spectra and the length covered varies according to the specific purpose of the measure. For example, a high-resolution SAL can be achieved with 125 spectra along a 5 μm line: almost any feature of the sample (a defect, a wrinkle, etc) should be observed. As the distance between two adjacent spectra is usually much lesser than the laser spot size, then a deconvolution of the signal with the gaussian shape of the beam must be performed to reduce the *oversampling* effect. As we will explain below, SAL is a special case of the hyperspectrum, and has the main advantage of being low-time-consuming compared to HS. Among the main disadvantages we find the limited information which can be obtained (in contrast to a 2D map) and the oversampling outside the line that we wish to measure.

Hyperspectrum HS combines a complete information about the emission and spatial resolution, which is suitable for those cases in which some features are being expected at specific locations of the sample, such as defects, quantum dots and/or wrinkles in MoS_2. Because of the long-time consumption of this technique, we find some issues such as thermal drifting, sample overheating and damaging. The only way to avoid those artifacts is by reducing the integration time (no more than 5 seconds) and the excitation power (below 125 μW).

Having discussed the distinct number of spectra, we may also classify the PL according to the temperature. The range of temperatures in which spectra can be obtained lies between 10K and 300K. We are particularly interested in the extreme cases of 10 K and room temperature because most of the features of quantum dot emission are displayed at very low temperatures. Furthermore, these results can be contrasted to that obtained at room temperatures in the pursuit of some emergent phenomena.

The implementation of low-temperature measurements makes it necessary to carry out a scheme of cooling the sample which includes 4K-liquid helium, a cryostat and a turbo-vacuum pump. As stated a few sections above, the usage of a long-work-distance objective allows us to easily couple the cryostat to the pre-existent setup. The usual path to perform a temperature-dependent measurement is to lower the pressure inside the cryostat by using a mechanical pump to around 10^{-3} mbar and then, to use a turbo-molecular pump to reduce the pressure to around 10^{-6} mbar. Then the sample is cooled with liquid helium in a cold-finger cryostat. This procedure allows us to achieve temperatures around 10 K.

Summarizing, in this chapter we listed and explained the main experimental techniques that we used in our research: from a detailed description of mechanical exfoliation, to the spectroscopic techniques used to characterize the samples, passing through the AFM-based nanoindentation. We also presented a short but

detailed study on the plastic-elastic properties of the PMMA substrate. We showed the indentation force curves and the stress-strain curve of PMMA, which are important to be considered in the indentation of MoS_2. About PL, we detailed several schemes of photoluminescence measurements, such as the single-PL spectrum, the spectra along-a-line and the hyperspectrum, which were performed in this work. Since PL is used to study the main features of the emission due to excitons, we devote the next chapter to address the physics of excitons with a special emphasis on the theoretical approach.

CHAPTER 4

THEORY OF THE EXCITON IN MOS_2

As discussed in Section 2.4, the excitations in MoS_2 have some special features which make the exciton here be rather different to excitons in other conventional semiconductors, such as GaAs, Si, Ge, etc. The large binding energy, the relatively large Bohr radius and the two-dimensional character makes the exciton be exceptionally appropriate for studying confinement or binding to defects. Different approaches for studying the exciton in MoS_2 have been addressed: analytical approaches and ab-initio calculations. We first discuss the ab initio calculations, among which we find the DFT and Bethe-Salpeter equation (BSE) theories.

Density functional theory (DFT) in the local density approximation (LDA) or the BSE [50, 56, 77, 78] give the most accurate estimates of the gap energy, kinetic energy and effective mass of carriers. Particularly, several groups around the world have performed highly computing-expensive calculations of MoS_2 in order to provide a set of parameters which can be used as the base of other more approximate analytical approaches which deal with the description of the shape of the bands and orbitals at the bands themselves [50]. Table 4.1 compiles some of the most relevant results of ab initio calculations of several groups, where the gap energy Δ, the hopping integral t, the spin-orbital coupling 2λ and deformation potentials $D_{\|}, D_{\perp}$ are displayed and whose employment in this work will be clarified later.

The main perturbative approaches that were pointed out in the preceding paragraph consist on two complementary theories for the quantitative description of the bands: the *tight-binding approximation* (TBA) and the $k \cdot p$ theory. TBA assumes that the electronic wavefunctions are a linear combination of single-electron atomic

	E_g (eV)	a (nm)	M_{exc}/m_0	t	2λ (eV)	ε	β	$D_{\parallel}$ (eV)	$D_{\perp}$ (eV)
Value	2.05	0.318	0.98	1.1	0.15	4.26	3.3	0.28	-7.18

Table 4.1 Table of ab-initio parameters for MoS_2, such as energy gap E_g, lattice parameter a, exciton's mass M_{exc}/m_0, hopping amplitude t, spin-orbit coupling λ, relative dielectric constant ε, and perturbation parameters $\beta, D_{\parallel}, D_{\perp}$ from deformation potential theory used in this work for theoretical approximations. From [50, 79]

orbitals belonging to each one of the bands. By using arguments based on group theory, we are allowed to specify these orbitals and calculate the perturbation on one orbital due to other neighboring atom orbitals. The result of this formalism is an estimate of the band shape in terms of the hopping integrals between adjacent sites [80].

Moreover, the $k \cdot p$ approach consists on calculating perturbatively the elements of the momentum operator near to the local minima/maxima of the bands. The result of this approach is an estimate of the band shape and also of the effective mass of the carrier, which is useful when calculating states of bound particles, such as excitons [81, 82]; this method will be examined in more detail in the following sections. Among other theoretical approaches of the exciton in 2D materials we find the *Dirac equation* and the *Schrödinger equation* which give accurate values of the exciton binding energy and reduced mass [83, 84]. There will not be further discussion of these last methods in this work, nonetheless we use their concepts to complement our $k \cdot p$ formalism which will be shown in the next section.

4.1 The $k \cdot p$ method for excitons in MoS_2

Single particle states are described through the one-electron Schrödinger equation:

$$H\psi_{n,\mathbf{k}}(\mathbf{r}) = E_{n,\mathbf{k}}\psi_{n,\mathbf{k}}(\mathbf{r}), \tag{4.1}$$

where $\mathbf{k}$ is the momentum, n is the label of the orbital state, $E_{n,\mathbf{k}}$ is the energy and H the Hamiltonian (without considering the spin-orbit coupling yet) of the particle:

$$H = \frac{p^2}{2m} + U(\mathbf{r}), \tag{4.2}$$

where the potential $U(\mathbf{r})$ involves the periodicity of the lattice. That is the reason why we write the electron state as a Bloch wavefunction:

$$\psi_{n,\mathbf{k}}(\mathbf{r}) = e^{i\mathbf{k}\cdot\mathbf{r}}u_{n,\mathbf{k}}(\mathbf{r}). \tag{4.3}$$

Since $\mathbf{p} = -i\hbar\nabla$, the Schrödinger equation for $u_{n,\mathbf{k}}(\mathbf{r})$ holds

$$\left(H + \frac{\hbar^2k^2}{2m} + H_{\mathbf{k}\cdot\mathbf{p}}\right)u_{n,\mathbf{k}}(\mathbf{r}) = E_{n,\mathbf{k}}u_{n,\mathbf{k}}(\mathbf{r}), \qquad H_{\mathbf{k}\cdot\mathbf{p}} = \frac{\hbar}{m}\mathbf{k}\cdot\mathbf{p} \tag{4.4}$$

Here, we consider $H_{\mathbf{k}\cdot\mathbf{p}}$ as a perturbation. As our aim is to calculate the bands around the K point, we have to expand perturbatively the relative momentum $\mathbf{q}$ which is measured from K and writing **k=q+K**. A complete description of the $k \cdot p$ treatment around points other than the Γ point in the Brillouin zone is done in the references [82, 85], we just describe the $k \cdot p$ model around K for the momentum q:

$$H_{\mathbf{k}\cdot\mathbf{p}} = \frac{\hbar}{2m}(q_+ p_- + q_- p_+), \tag{4.5}$$

where $q_\pm = q_x \pm q_y$ and $p_\pm = p_x \pm p_y$. Within this $\mathbf{k}\cdot\mathbf{p}$ formalism for electrons in monolayer MoS_2, we will just consider the coupling between the CB and VB edges, and write this hamiltonian in a basis of two states. We use the same derivation of the exciton features as that shown in the references [79, 81], which use the first-order perturbation theory to calculate the matrix elements of the $H_{\mathbf{k}\cdot\mathbf{p}}$ hamiltonian, $\langle\phi_n|p_\pm|\phi_m\rangle$, provided the $|\phi_i\rangle$ basis vectors are independent of $\mathbf{k}$. All considerations on symmetry and group theory applied to the case of orbitals at the K point of the Brilloin zone in MoS_2 come from references [82, 86]. These same considerations allow us to construct the $k \cdot p$ hamiltonian:

$$H_0 = at(\tau k_x \hat{\sigma}_x + k_y \hat{\sigma}_y) + \frac{\Delta}{2}\hat{\sigma}_z, \tag{4.6}$$

where a is the lattice parameter, t is the hopping integral between neighboring lattice sites, Δ is the electronic band gap, the $\hat{\sigma}_i$ are the usual Pauli matrices and $\tau = \pm 1$ is the valley index indicating whether the K or K' valley, respectively. The matrix form of the hamiltonian is

$$H_0 = \begin{pmatrix} \frac{\Delta}{2} & at(\tau k_x - ik_y) \\ at(\tau k_x + ik_y) & -\frac{\Delta}{2} \end{pmatrix} \tag{4.7}$$

As seen in Section 2.1, it is necessary to include the spin-orbit coupling in the hamiltonian, despite this enlarges the Hilbert space to include the spin degree of freedom. The new hamiltonian is

$$H = H_0 - (\lambda\tau)\frac{\hat{\sigma}_z - 1}{2} \otimes \hat{s}_z, \tag{4.8}$$

or in matrix notation,

$$H = \begin{pmatrix} \frac{\Delta}{2} & at(\tau k_x - ik_y) & 0 & 0 \\ at(\tau k_x + ik_y) & -\frac{\Delta}{2} + \lambda\tau & 0 & 0 \\ 0 & 0 & \frac{\Delta}{2} & at(\tau k_x - ik_y) \\ 0 & 0 & at(\tau k_x + ik_y) & -\frac{\Delta}{2} - \lambda\tau \end{pmatrix} = H_\uparrow + H_\downarrow \tag{4.9}$$

The new basis is $\{|\phi_{c\uparrow}\rangle, |\phi^\tau_{v\uparrow}\rangle, |\phi_{c\downarrow}\rangle, |\phi^\tau_{v\downarrow}\rangle\}$, where $\uparrow, \downarrow$ denote spin-up and spin-down respectively. As seen in eq. (4.9), the spin-up components are decoupled from the spin-down components, thus we could study the physics of just one of

these spin projections. The energy eigenvalues of the spin-up particle (or equivalently the $\tau = +1$ valley) are the roots of the characteristic polynomial of $H_\uparrow$:

$$\begin{aligned}(\Delta/2-\varepsilon)(\lambda-\Delta/2-\varepsilon)-atk^2&=0\\ \varepsilon=\frac{\lambda}{2}\pm\frac{1}{2}\sqrt{(\lambda-\Delta)^2+4atk^2}.&\end{aligned}\tag{4.10}$$

The sign "+" corresponds to the energy of a particle in the conduction band and the "-" for the valence band. At this point, we have just described the energy of a single particle in the conduction and valence bands of single layer MoS_2. But actually we are interested about the description of two coupled particles at CBM and VBM. Therefore, we can write the two-particle state as a function of two coordinates:

$$\Psi_{ij\uparrow}(\mathbf{r}_1,\mathbf{r}_2)=\phi_{i\uparrow}(\mathbf{r}_1)\phi_{j\uparrow}(\mathbf{r}_2),\tag{4.11}$$

where $i = c, v$. We have now 4-component spinors to describe the state:

$$\Psi_\uparrow=\begin{pmatrix}\phi_{c\uparrow}(\mathbf{r}_1)\phi_{c\uparrow}(\mathbf{r}_2)\\ \phi_{c\uparrow}(\mathbf{r}_1)\phi_{v\uparrow}(\mathbf{r}_2)\\ \phi_{v\uparrow}(\mathbf{r}_1)\phi_{c\uparrow}(\mathbf{r}_2)\\ \phi_{v\uparrow}(\mathbf{r}_1)\phi_{v\uparrow}(\mathbf{r}_2)\end{pmatrix}=\begin{pmatrix}\psi_c\\ \psi_v\end{pmatrix},\tag{4.12}$$

where

$$\psi_c=\begin{pmatrix}\phi_{c\uparrow}(\mathbf{r}_1)\phi_{c\uparrow}(\mathbf{r}_2)\\ \phi_{c\uparrow}(\mathbf{r}_1)\phi_{v\uparrow}(\mathbf{r}_2)\end{pmatrix},\qquad\qquad\psi_v=\begin{pmatrix}\phi_{v\uparrow}(\mathbf{r}_1)\phi_{c\uparrow}(\mathbf{r}_2)\\ \phi_{v\uparrow}(\mathbf{r}_1)\phi_{v\uparrow}(\mathbf{r}_2)\end{pmatrix}\tag{4.13}$$

As the Coulomb interaction depends only on the relative distance of the particles $r = |\mathbf{r}| \equiv |\mathbf{r}_1 - \mathbf{r}_2|$, the hamiltonian takes the form $H_T = H_1 + H_2 + V(r)$, where the H_i is the hamiltonian of the i-th particle, and $V(r) = 1/4\pi\varepsilon\varepsilon_0 r$ the usual Coulomb potential.

Note that the fact of the hole being an electron vacancy at the valence band means that it has the opposite quantum numbers of one electron at the same position in the valence band, including its energy and spin, just like an object reversed by a mirror reflection. A consequence of this is that the energy of a hole $\varepsilon^{(h)}$ is related to the corresponding electron energy $\varepsilon^{(e)}$ as $\varepsilon^{(h)}_\uparrow = -\varepsilon^{(e)}_\downarrow$. Taking this argument into account, we write the hamiltonian in the new basis as:

$$H_T = \begin{pmatrix} V(r) & -at(k_{2x} - ik_{2y}) & at(k_{1x} - ik_{1y}) & 0 \\ -at(k_{2x} + ik_{2y}) & \Delta - \lambda + V(r) & 0 & at(k_{1x} - ik_{1y}) \\ at(k_{1x} + ik_{1y}) & 0 & -\Delta + \lambda + V(r) & -at(k_{2x} - ik_{2y}) \\ 0 & at(k_{1x} + ik_{1y}) & -at(k_{2x} + ik_{2y}) & V(r) \end{pmatrix}. \tag{4.14}$$

The detailed calculation of the solution of the two-body problem with the hamiltonian (4.14) can be found in the appendix A. We just clarify that the low-kinetic-energy approximation is used again in our first-order considerations. Besides, we arrive to the Schrödinger equation for a 2D hydrogen atom:

$$\left[\mathscr{F}_1(\varepsilon) \nabla^2_{\mathbf{r}} - \frac{e^2}{4\pi\varepsilon_0\varepsilon} \right] \phi_{cv} = \mathscr{F}_0(\varepsilon)\phi_{cv}, \tag{4.15}$$

where $\mathscr{F}_1(\varepsilon) = \frac{2a^2t^2}{\varepsilon}$ ans $\mathscr{F}_0(\varepsilon) = \varepsilon - \Delta + \lambda - \frac{a^2t^2K^2}{2\varepsilon}$. From the solutions of this equation we are able to obtain the analytical expressions for the binding energy, the rest energy, and the effective mass of the exciton:

$$\begin{aligned} \varepsilon(0) &= \frac{8\zeta(\Delta - \lambda)}{8\zeta + C}, && \text{Exciton rest energy} \\ M &= \frac{\hbar^2(\Delta - \lambda)}{\zeta}, && \text{Exciton effective mass} \\ E_B &= \frac{C(\Delta - \lambda)}{8\zeta + C}, && \text{Exciton binding energy} \end{aligned} \tag{4.16}$$

where $\zeta = a^2t^2$ and $C = (e^2/(4\pi\varepsilon_0\varepsilon)(n - 1/2))^2$.

4.2 Excitons in a deformed lattice

Those simple formulae allows us to make some important predictions when the LDA parameters (Δ, λ, a, t) are dependent on a certain feature of the system. To be more specific, consider the case when the MoS_2 is subject to a certain strain. For now, we will not specify the type of strain that is acting on the material, nor the nature of the forces and stresses that provoked such strain, just we will assume that strain implies the displacement of the atoms from the sites $\mathbf{R}_i$ to their new positions at $\mathbf{R}_i + \delta\mathbf{R}_i$. The energy of a crystal can be expanded around the unstrained state characterized by the positions $\mathbf{R}_i$ as follows:

$$E_{n,\mathbf{k}} = E^0_{n,\mathbf{k}} + \frac{\partial E_{n,\mathbf{k}}}{\partial \mathbf{R}} \cdot \delta\mathbf{R}, \tag{4.17}$$

where $n, \mathbf{k}$ labels the n-th band and momentum $\mathbf{k}$ and $E^0_{n,\mathbf{k}}$ the energy of the unstrained lattice. Then the energy shift is $\frac{\partial E_{n,\mathbf{k}}}{\partial \mathbf{R}} \cdot \delta\mathbf{R}$. The *deformation potential*

theory states that the energy shift can be written in such a way that it reflects the symmetry of the crystal and is proportional to the strain [45]. For small deformations of the C_{3h} honeycomb lattice, the energy gap yields [45]

$$\frac{\partial E_{n,\mathbf{k}}}{\partial \mathbf{R}} \cdot \delta \mathbf{R} = D_{\parallel}\varepsilon_{\parallel} + D_{\perp}(\varepsilon_{xx} + \varepsilon_{yy}), \tag{4.18}$$

where $D_{\parallel}$ and $D_{\perp}$ are parameters that represent the energy shifts for a deformation parallel and perpendicular to the normal vector of the plane, respectively. These parameters are obtained via ab initio methods. It can also be shown that for small deformations the lattice parameter is affected by strain as [63]

$$a = (1+\varepsilon) \cdot a_0, \tag{4.19}$$

where $a_0 = 0.324$ nm is the lattice parameter of a free MoS_2 membrane and ε is the strain. The momentum element t of the $k \cdot p$ hamiltonian is also dependent on the interatomic distance, then we could also approximate it by

$$t = t_0(1 - \beta \frac{\delta a}{a_0}), \tag{4.20}$$

where β is a positive constant and t_0 is the hopping term at zero strain. As the tensile strain is defined as $\varepsilon = \delta l/l = \delta a/a$, we write the hopping element as

$$t = t_0(1 - \beta\varepsilon). \tag{4.21}$$

This equation states that the hopping element decreases as the interatomic distance becomes greater: this is because the overlapping of the orbitals of adjacent atoms is lessened when the tensile strain raises. The parameter β is also obtained from ab initio calculations and has the rough value of 3.2 for MoS_2 [87]. The spin-orbital coupling is not affected by strain [88], thus in principle, we are able to know the dependence on the strain of the gap energy, the rest energy and the effective mass of the MoS_2 exciton for small deformations. For most of the cases, the strain tensor ε is a function of the coordinates (x,y), thus we can model the exciton features for an arbitrary strain field. For instance, this will be useful when considered abrupt spatial variations of the strain field such as the case of a nanoindentation.

Summarizing, in this part we have reviewed the main electronic, mechanical, vibrational optical and excitonic properties of MoS_2, in order to give an overall idea of the features and concepts that will be addressed in later chapters of this work. We also discussed the effect of the strain on the gap energy and the exciton effective mass and how this can be useful to develop our hypothesis of quantum dot generation via nanoindentation. Then in the following chapters we will introduce the definition of quantum dot by supporting ourselves in the idea of quantum confinement and present our results on theoretical calculations of quantum dots. Furthermore we present our main experimental results of AFM, Raman and photoluminescence spectroscopy measurements.

PART II

THE QUANTUM DOT

CHAPTER 5

QUANTUM DOTS IN MOS_2

Since the 1990s, scientists began to use the term *quantum dot* to describe "artificial atoms" which were formed when growing nano-heterostructures in semiconductors [10]. These artificial atoms have the property of emitting in a single, very narrow spectral line because of two facts: the enhancement of radiative processes over the non-radiative increases the emission intensity and the quantum confinement propitiates a discrete distribution of energy levels, rather similar to the energy levels of atoms.

But how are these energy levels distributed within the confinement potential? To answer this question we recall the *Heisenberg's uncertainty principle* which relates the spreading of both particle's momentum Δp and position Δx. As the spreading (or separation) of the confined levels is proportional to the kinetic energy, e.g. to Δp^2, we expect this separation to be greater than the thermal fluctuations which are proportional to $k_B T/2$. If we associate Δx to the width of the well, we have a first criterion of confinement [55]

$$\Delta x \leq \sqrt{\frac{\hbar^2}{m k_B T}} \tag{5.1}$$

We also expect that quantum confinement emerges when the *de Broglie* wavelength of the particle $\lambda = h/\Delta p$ is comparable to the size of the well, and the spreading of the energy levels is related to it through the following formula:

$$\Delta x = \lambda \sim \sqrt{\hbar^2/2m\Delta E}, \tag{5.2}$$

where ΔE is the energy separation between the first confined levels of the well. At this point we have given a satisfactory definition of confinement and established the minimum requirements for the confinement to be manifested in a quantum system. But the meaning of *quantum well* is still obscure, reason why we will introduce this concept in the context of semiconductors.

5.1 What is a quantum dot?

When layered structures of different semiconductors are formed, there will be regions of different band gaps, which will be arranged in such a way that the Fermi level is the same along the structure. This can generate *potential energy wells* for both electrons and holes at the conduction and valence bands, respectively and then the criteria of quantum confinement can be addressed here. When studying the motion of a free electron in a semiconductor, it is necessary to describe the density of states $g(E)$ i.e. the number of states that can be occupied by an electron of energy E. The density of states depends on the dimensionality of the material, as can be seen in Figure 5.1, where $g(E)$ changes from a monotonically and smoothly varying function in the bulk (3D) case, to a discrete energy distribution in the quantum dot (defined as the zero dimensional case), passing through the step-shaped $g(E)$ for quantum well (2D) and hair comb-shaped for quantum wires (1D).

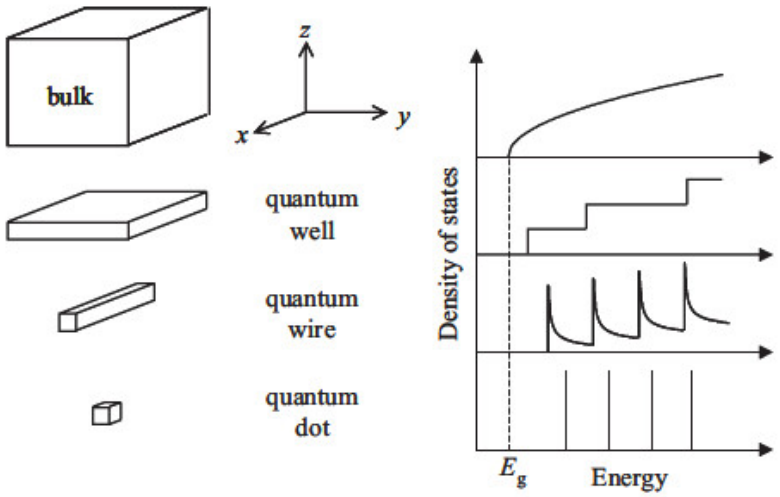

Figure 5.1 Density of states for the same material as a bulk form, a quantum well, quantum wire or quantum dot. Extracted from [1].

Despite the fact that in our work on MoS_2 we do not address any *heterostructure*, the principle of confinement and the density of states is completely analogous to the situation described above, regardless of the nature of the spatial variation of the band gap. As MoS_2 is nearly a two-dimensional semiconductor, the density of states of a free electron is described by that of a quantum well in Figure 5.1,

and the criteria for three-dimensional confinement (a quantum dot) is given by eqs (5.1), (5.2) for all three dimensions. Then we present our definition of quantum dot:

Definition 1 Quantum dot*: A structure that confines particles with a certain de Broglie wavelength and satisfies the criteria of confinement given by the Heisenberg's uncertainty principle in the form of the equations* (5.1) *and* (5.2)*.*

Having properly defined a quantum dot, then we will describe the confinement of excitons in quantum dots in the next section, and establish the regimes in which the confinement energy is more relevant than the Coulomb interaction between electron and hole (and vice versa).

5.2 Excitons in quantum dots

As stated in the last section, a spatial variation of the band gap can lead to the emergence of confinement potentials for both electrons and holes in a semiconductor. This is still the case of MoS_2 in which some mechanisms are able to induce such spatial variations of the gap. But first, we will describe separately the quantum dot-induced confinement for each Wannier-Mott and Frenkel excitons.

The large Bohr radius and low binding energy of a Wannier-Mott exciton allows us to treat the Coulomb interaction between electron and hole as a perturbation, since the energy gap E_g is much greater than the exciton binding energy E_b [59]. In this case, the energy levels for both electron and hole are quantized separately, thus we can think of the quantum dot as a confiner of almost independent electrons and holes [59].

On the other hand, Frenkel excitons have a binding energy such that the confining potential has to be treated as a perturbation, then the whole particle is confined [60]. Thus in this case, the quantum dot acts as a confiner of excitons. The most common examples of quantum dots of this kind in MoS_2 are probably those defect sites that trap the so-called *bound excitons*.

As excitons in MoS_2 share some features of both Wannier-Mott and Frenkel, then we assume that the whole exciton is the particle that suffers confinement in the QD, hence the description of the exciton given in Section 4.1 also remains valid for excitons confined in quantum dots. Along this work we have addressed several times the behaviour of MoS_2 when is subject of strain: a sufficiently abrupt spatial variation on the strain field applied to a MoS_2 monolayer could generate a quantum well that acts as a confinement potential, and this spatial variation could be produced via nanoindentation, then we can now formulate the central hypothesis of this dissertation:

Hypothesis 1 Exciton confinement via nanoindentation*: A quantum dot that confines excitons in MoS_2 can be generated through nanoindentation if the following two conditions are satisfied: The width of the well is such that satisfies equation* (5.1) *for thermal fluctuations at a given temperature T, and the depth of the well is such that the energy separation between the first levels satisfies the equation* (5.2)*.*

Provided this definition, we can now generate a set of specific conditions that satisfy the hypothesis of confinement. We will have to describe the shape of the nanoindentation in order to model the strain field but this is not a trivial task, then we will have to assume some shapes that could give us an estimate of the energy separation and the exciton wavefunctions. This will be the subject of the next section, in which we characterize the shape of the MoS_2 membrane through its width and depth and define an optimal indentation that behaves as a true quantum dot. For now, we can choose the indentation width $l \sim \Delta x$ that satisfies the condition (5.1): at 10 K, the maximum width of the well that exhibits confinement of excitons of mass $M = 0.98m_0$ is $l \approx 10$ nm, while at 4 K the maximum width is $l \approx 15$ nm.

5.3 Wavefunctions for an exciton in a nanoindented MoS_2 monolayer.

To find the distribution of confined levels in indented MoS_2 we should first briefly address the wavefunctions. Using the same notation as in the preceding chapters, we model the confined exciton through the following hamiltonian:

$$H_{\text{exc}} = H_{k\cdot p}^{(e)} + H_{k\cdot p}^{(h)} + V(r) + U(\mathbf{R}), \tag{5.3}$$

where $H_{k\cdot p}^{(e)}$ and $H_{k\cdot p}^{(h)}$ are the $k\cdot p$ hamiltonians for electon and hole, respectively, $V(r)$ is the Coulomb electrostatic potential which depends on the relative e-h distance and $U(\mathbf{R})$ is the confinement potential for the exciton, which depends on the center-of-mass position of the exciton. In our first-order approximation, $U(\mathbf{R})$ is decoupled of the rest of the terms of H_{exc}, thus we can write the exciton wavefunction as

$$\Psi_{\text{exc}}(\mathbf{R},\mathbf{r})^{(m,n,\mathbf{k})} = \Phi^m(\mathbf{R})\phi_{cv}^{n,\mathbf{k}}(r), \tag{5.4}$$

where the indices m,n specify the confined state in the well and the 2D-hydrogen level of the exciton, and $\mathbf{k}$ stands for the exciton momentum. At low temperatures, we can consider just those ground-state excitons with **q=0**, then the Schrödinger equation stands:

$$H_{\text{exc}}\Phi^m(\mathbf{R})\phi_{cv}(r) = (E_0 + E_m)\Phi^m(\mathbf{R})\phi_{cv}(r), \tag{5.5}$$

where E_0 is the exciton rest energy. As the ground state of the exciton is just an additive constant for the confined energies, our aim in this chapter will be to calculate the eigenfunctions of $U(\mathbf{R})$, that is, we will calculate $\Phi^m(\mathbf{R})$.

In a first approximation, we will assume that the shape of the indentation is isotropic, whose profile is shown in Figure 5.2 (a). A more complete approach of the deformation due to a spherical indenter is given by the J_2 *plastic-flow theory* which assumes a power-law for the strain-stress curve, small elastic-plastic deformations and paraboloidal indenters [89]. The central role of this theory is to find the hardening function of the material, which goes beyond the scope of this work, due to the large number of considerations that we have to make to describe the deformation of an atomically thin membrane on a plastic polymer.

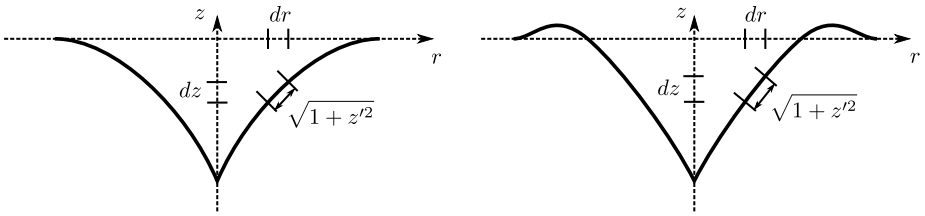

(a) (b)

Figure 5.2 Profile of a nanoindentation. (a) Shows the shape assumed for calculations, while (b) represents the real shape due to the plastic deformation by a spherical indenter.

Note that the only difference between Figure 5.2 (a) and (b) is the pile-up in the borders of the indentation. As we shall see later, this pile-up is no more than a few tenths of nm, thus we can neglect them in our description of the strain. The most similar shape to that represented in the diagram is a sinusoidal function (See also Figure 5.3 (a)):

$$z(r) = \begin{cases} h\left(\sin\frac{\pi r}{l} - 1\right) & 0 \le r \le l/2 \\ 0 & \text{otherwise} \end{cases} \tag{5.6}$$

then the strain tensor could be written as

$$\varepsilon_{xx} = \varepsilon_{yy} = \frac{1}{2}\left(\frac{dz}{dr}\right)^2 = \begin{cases} \frac{\pi^2}{2}\left(\frac{h}{l}\right)^2 \cos^2\frac{\pi r}{l} & 0 \le r \le l/2 \\ 0 & \text{otherwise} \end{cases}, \qquad \varepsilon_{zz} = \nu\varepsilon_{xx}, \tag{5.7}$$

where ν is the Poison ratio of MoS_2. Here, $\varepsilon_{xx} = \varepsilon_{yy}$ because MoS2 behaves isotropically for biaxial deformations [90]. In order to obtain an expression for the potential $U(\mathbf{R})$, we recall the results of Chapter 4: The band gap, the hopping amplitude and the lattice constant are

$$\begin{aligned} \Delta &= \Delta_0 - (D_\parallel \nu + 2D_\perp)\varepsilon_{xx}, \\ t &= t_0(1-\beta\varepsilon_{xx}), \qquad a = a_0(1+\varepsilon_{xx}) \end{aligned} \tag{5.8}$$

Using the notation $\zeta_0 = t_0^2 a_0^2$, we obtain for the exciton rest energy:

$$E_0(\varepsilon_{xx}) = \frac{8\zeta_0(\Delta_0 - \lambda)}{8\zeta_0 + C}\left[1 - \left(2(\beta-1) + \frac{D_\parallel \nu + 2D_\perp}{\Delta_0 - \lambda}\right)\varepsilon_{xx} + \mathscr{O}(\varepsilon_{xx}^2)\right]. \tag{5.9}$$

The strain-field potential $U(\mathbf{R})$ should be assumed to be generated by the spatial variations of the exciton energy. In this way, we can set the potential equal to zero out of the indentation and combine the equations (5.7) and (5.9) to obtain a specific form of the potential:

$$U(\mathbf{R}) = \begin{cases} -\frac{\pi^2}{2} E_0(0) \left(\frac{h}{l}\right)^2 \left(2(\beta-1) + \frac{D_\parallel \nu + 2D_\perp}{\Delta_0 - \lambda}\right) \cos^2 \frac{\pi r}{l} & 0 \le r \le l/2 \\ 0 & \text{otherwise} \end{cases}, \quad (5.10)$$

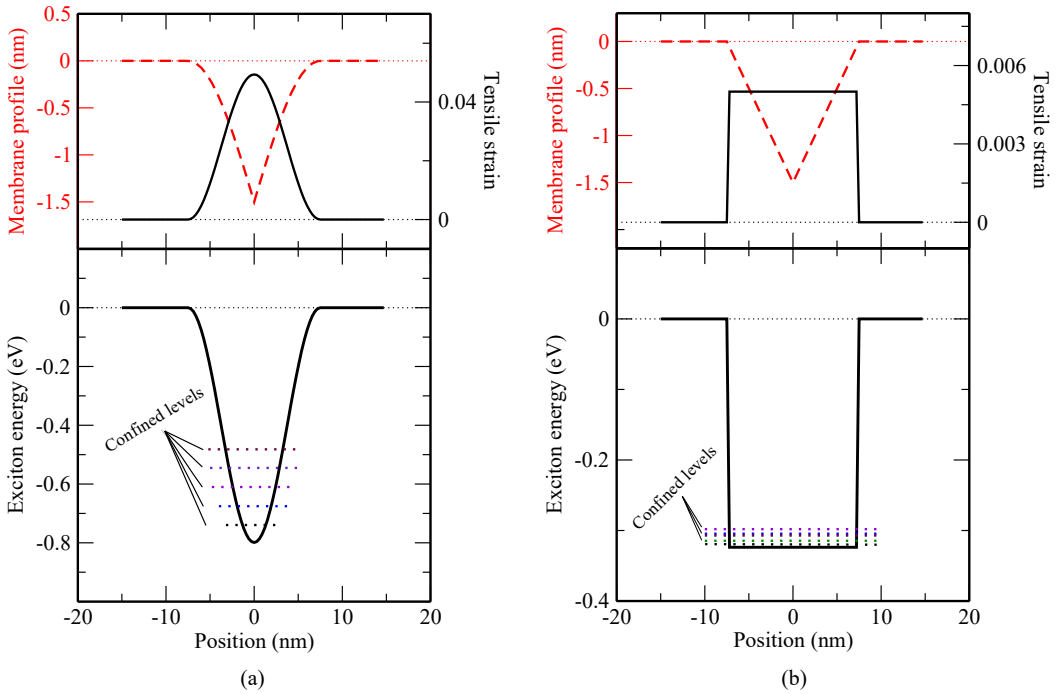

Figure 5.3 Strain profiles of indentations used to model the exciton confination: (a) the smooth sinusoidal profile and (b) a triangular profile.

Nevertheless, this potential seems to be very difficult to solve. In order to obtain an estimate for the confined levels, let us make a gross assumption: let the shape of indentation be triangular, as shown in Figure 5.3 (b). This rough approximation describes a constant strain $\varepsilon_{xx} = 2(h/l)^2$ inside the indentation, and zero outside. That means that the confinement potential is then reduced to a finite square well potential of depth

$$V_0 = 2E_0(0) \left(\frac{h}{l}\right)^2 \left(2(\beta-1) + \frac{D_\parallel \nu + 2D_\perp}{\Delta_0 - \lambda}\right). \quad (5.11)$$

Equation (5.11) is also useful to quantify the modification of the exciton energy as a function of the (biaxial) strain, if we consider that V_0 is the negative energy shift of the exciton energy. Figure 5.4 shows this behavior, in which the exciton energy is lowered when increased the biaxial tensile strain of MoS_2 monolayer. In the Example 5.1 we illustrate the assumption of a triangular shape of the indentation in MoS_2.

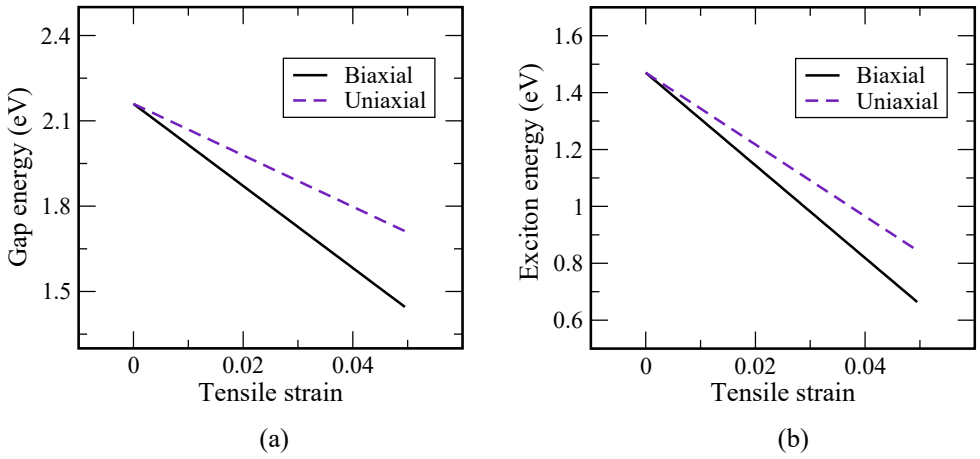

Figure 5.4 Gap energy (a) and exciton energy (b) vs.tensile strain based on the deformation potential theory.

EXAMPLE 5.1 Excitons in a cylindricallly symmetric square well

We can assume the excitons to be confined in a cylindrically symmetric square well, in order to have a first estimation of the confinement criteria. If these criteria is satisfied for this case, then they will also be satisfied for the sine-shaped profile. The solutions of the Schrödinger equation are radial wavefunctions written in terms of Bessel and modified Bessel functions or the first kind:

$$\Phi(\mathbf{R}) = \begin{cases} A_n J_n\left(\sqrt{\frac{2m(V_0-E)}{\hbar^2}}r\right) & 0 \leq r \leq l/2 \\ B_n K_n\left(\sqrt{\frac{2mE}{\hbar^2}}r\right) & r > l/2 \end{cases}, \tag{5.12}$$

where A_n, B_n are constants to be adjusted to satisfy the conditions of continuity in the function and in the first derivative of both solutions at $l/2$. n are integer indices that describe the angular part of the wavefunction, $e^{in\phi}$.

We calculate numerically the first confined levels of the cylindricallly symmetric square well. We use the following parameters for the calculation: l= 15 nm, h = 1.5 nm, then V_0 = -323.8 meV. Then the energy difference between the first two confined levels is $\sim$24 meV, which is greater than the thermal fluctuations at 4 K ($\sim$0.3 meV). Using this values, we find that the de Broglie wavelenght of the exciton for this energy separation is $\lambda \sim 20$ nm, which is even larger than the diameter of the indentation.

The example 5.1 confirms that a 15 nm - diameter and 1.5 nm - depth indentation are suitable conditions for exciton confinement in MoS_2. Additionally, we simulated the confined exciton wavefunctions for the sine-shaped indentation case via finite-elements, powered by COMSOL^{TM}. Figure 5.5 shows the first confined wavefunctions in a 15 nm sized circular indentation. We have to consider, however, that in most of the cases (as we will explore in the next chapters) the actual shape of indentations is not circular but triangular, due to the format of the AFM tip used to produce the indentation. This will break a degeneracy due to the cylin-

drical symmetry in the former case, causing a small splitting of the excited states of excitons.

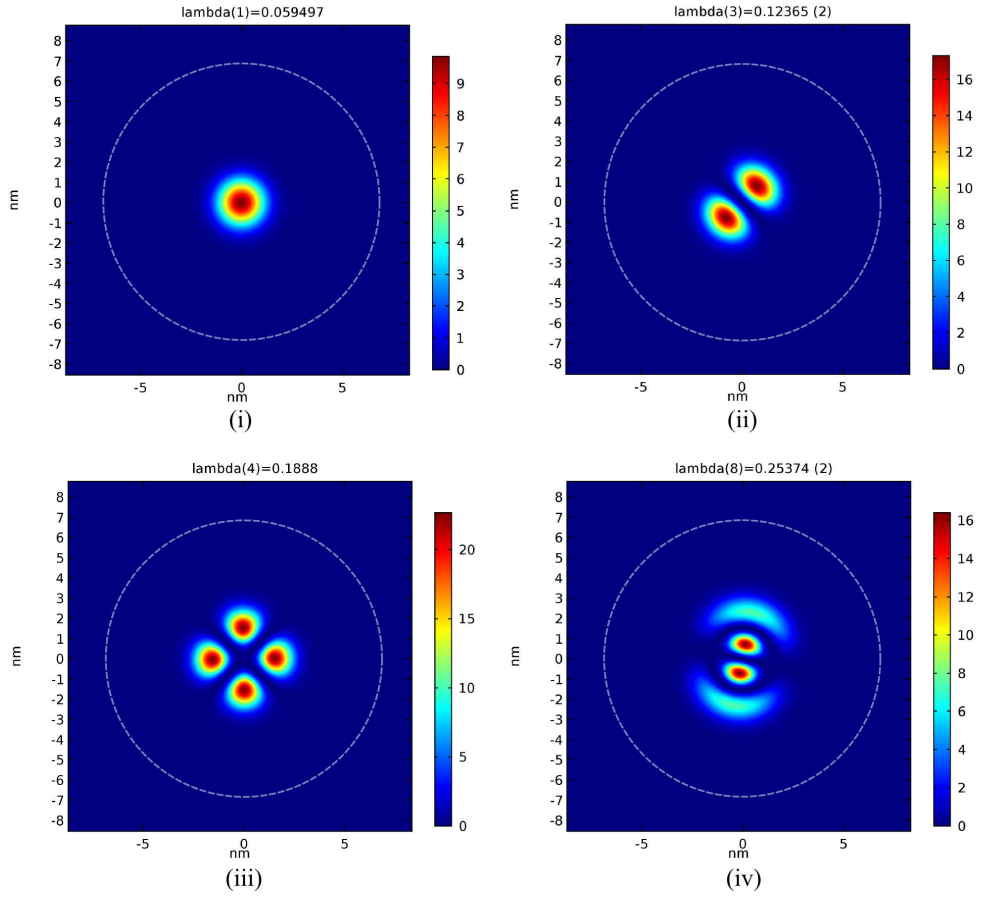

Figure 5.5 Simulation in COMSOL of the first four confined states of the potential of equation (5.10) in a circular indentation, organized from (i) to (iv).

The simulations on a 15 nm - side triangular indentations were also performed with COMSOL^{TM}. We obtained an energy separation of $\sim$9 meV between the first two confined levels, which is still larger than the thermal fluctuations at 4K. The wavefunctions of the first confined states are plotted in Figure 5.6.

In this chapter we constructed the hypothesis of exciton confinement that helped us to determine the conditions in which a quantum dot could be generated via a strain field. As the technique used to generate this local field was the AFM-nanoindentation, the devote the next chapter to review the features of AFM indentation for the case of a membrane of MoS_2 deposited over a plastic polymer substrate. We also discuss the main results of the optical characterization via the photoluminescence.

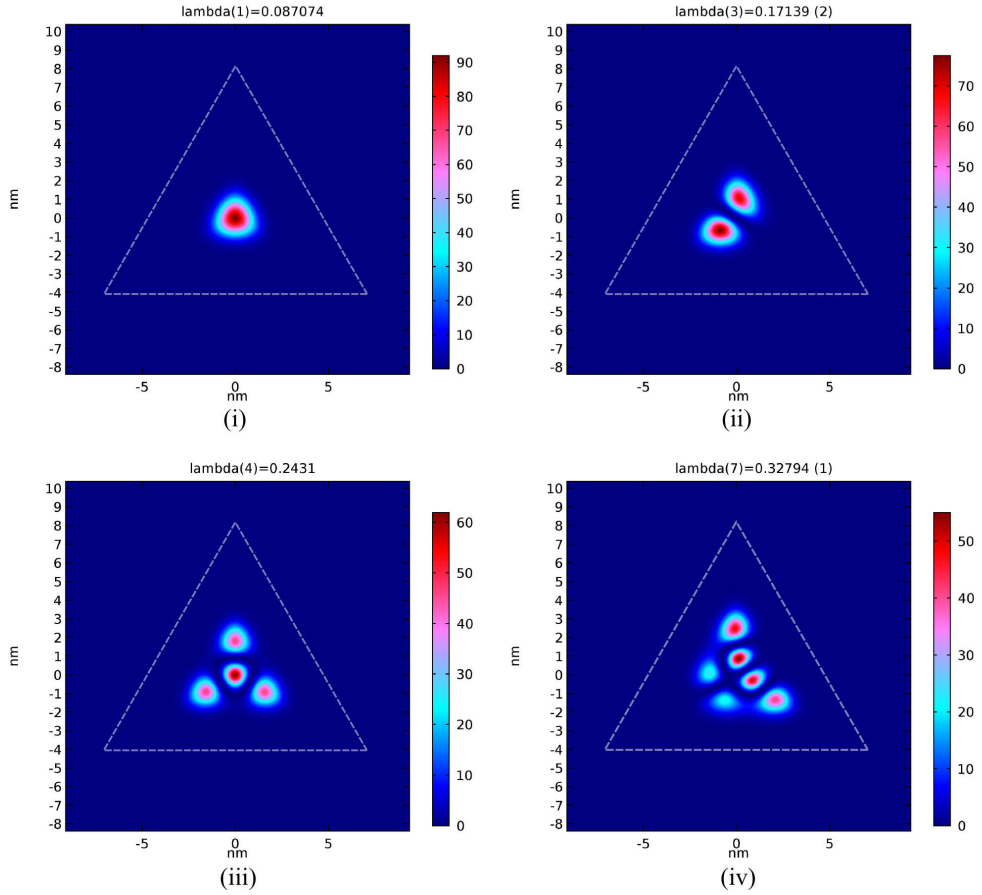

Figure 5.6 Simulation in COMSOL of the first four confined states of the potential of equation (5.10) in a triangular indentation, organized from (i) to (iv).

CHAPTER 6

GENERATION AND CHARACTERIZATION OF QUANTUM DOTS

Provided enough theoretical background, we performed nanoindentations via the atomic force microscopy of MoS_2 monolayers over PMMA substrate, because this polymer displays most of the plastic - elastic attributes that are suitable to achieve the indentation sizes required for exciton confinement. Nevertheless, the technique of nanoindentation of MoS_2 over a polymer substrate has not been developed by any other group yet[1], thus an exhaustive analysis of all the possible issues has to be performed and recorded systematically, before starting the characterization of the indentation itself.

6.1 Nanoindentation of MoS_2 on PMMA substrate via AFM

We have already addressed the plastic - elastic behavior of PMMA in past chapters and obtained the stress-strain, $\sigma - \varepsilon$, curve of the substrate, which behaves as $\sigma = \alpha\varepsilon^{\beta}$, where α is a positive constant and β is an exponent between zero and one. As we assumed that only the spherical end of the indenter was in physical contact with the sample at the indentation [75], we may also relate the force of the indenter to the mean strain generated $\bar{\varepsilon}$ as:

$$F_{\text{PMMA}} = A\alpha\bar{\varepsilon}^{\beta}, \tag{6.1}$$

[1]We found in the literature some atomistic simulations of nanoindentations on ultrathin materials, such as in ref. [91], and also on few-layers of MoS_2 over a rigid substrate, as in reference [92]

where $A = 2\pi r^2$ is the surface of the half-spherical indenter. We also know by the large elastic modulus of MoS_2 that the membrane remains elastic for most of the forces used in the indentation. The formalism of the Föpl-Henkyl equation [93] for a clamped circular membrane subjected to central concentrated force loads has been known for giving analytical expressions for the membrane deformation and radial tension. They also predict that for a given Poison's ratio, there could emerge some radial wrinkles that make the membrane shape lose its original azimutal symmetry. Nonetheless, for the case of MoS_2, which has a low Poison's ratio (ν=0.245), the membrane deformation is azimutally symmetrical and its maximum deflection at the center w_0 is related to the force load F by the following expression:

$$\left(\frac{2\omega_0}{l}\right)^3 \approx \left(\frac{4}{5}\right)^2 \frac{F}{\pi Y l}, \tag{6.2}$$

where l and Y are the membrane radius and the membrane stiffness, respectively. If we take the mean strain $\bar{\varepsilon}^2 = (w_0/l)^2$, we can write the force as

$$F_{\mathrm{MoS2}} = \left(\frac{5}{4}\right)^2 \frac{\pi Y l}{2^{3/2}} \bar{\varepsilon}^{3/2} \tag{6.3}$$

That means that a system composed by both the polymer substrate and MoS_2 membrane should satisfy the principle of superposition when performing an indentation:

$$F_{\mathrm{indent}} = F_{\mathrm{PMMA}} + F_{\mathrm{MoS2}} = \alpha A \bar{\varepsilon}^{\beta} + \frac{5}{4}\frac{\pi Y l}{2^{3/2}} \bar{\varepsilon}^{3/2} \tag{6.4}$$

This reasoning could be justified by considering that all the force exerted by the indenter is invested on a plastic deformation of PMMA *plus* an elastic deflection of the MoS_2 membrane. Conservation of energy could also prove this statement by additionally requiring that the work done on the system be slow and adiabatical i. e. no energy is used to heating the material. To put some numbers in this equation, let us consider a nanoindentation of $l = 30$ nm size and mean strain of 2%, then the force needed to produce such an indentation is

$$F_{\mathrm{indent}} \approx 30.9\ \mathrm{nN} + 14.7\ \mathrm{nN} = 45.6\ \mathrm{nN} \tag{6.5}$$

Then, what force is needed on the AFM cantilever in order to produce a force F_{indent} over the sample?. By using the same considerations for the cantilever sensibility s and spring constant k that were addressed in Section 3.2, we are able to assert that the maximum deflection[2] of the cantilever Δx in the force curve is related to the setpoint voltage ΔV and F_{indent} via the following equation:

$$\Delta x = \frac{\Delta V}{s} + \frac{F_{\mathrm{indent}}}{k},$$

[2]not to be confused with the width of the confinement potential of last chapter, also named Δx

which allows us to predict which setpoint voltage is needed to perform the nanoindentation

$$\Delta V = s\left(\Delta x - \frac{F_{\text{indent}}}{k}\right). \tag{6.6}$$

Now, by extracting information of a force curve in which Δx =39 nm (that is a typical value for MoS_2 indentations), and using the known parameters of our cantilever we obtain that $\Delta V \approx 2.42$ V. We have to make an important clarification here: the force of indentation and setpoint voltage calculated here are mere estimates of the actual scenario, which we summarize below:

- The MoS_2 was assumed to be a clamped circular membrane of radius l. This means that the strain on the borders does not tend to zero but the MoS_2 is fixed there. This is partially true because the strain field generated by an indentation is not zero out of it, despite MoS_2 could be displaced, peeled off, or even torn, as we will see later.
- The indentation was assumed to be slow and adiabatic. This was considered due to the "low" indenter velocities ($\sim$4 μm/s). However, a more detailed study of the (thermo)dynamics of nanoindentations is needed to prove this argument [94](this goes beyond the scope of this work) and leads us to the third point in this discussion,
- the dynamics of the indentation is rather complicated: Plastic deformations are processes with hystheresis [95], thus a maximum AFM cantilever's deflection just reveals the maximum depth achieved by the indented onto the sample, but the final depth is always less. This could also explain a certain randomness in the indentation's size and depth: we will return to this point after showing our results.

Now, we will show our main results with respect to AFM indentation in PMMA substrates. There are two types of configurations in which the indentations were performed: the *single indentation* and the *matrix indentation*. The first consists on several isolated indentations which were spatially separated ($\sim$1.5 μm between two of them, see Figure 6.1). The main advantages of this configuration are that we avoid the generation of strain fields among the indentations and we can measure the photoluminescence of each one separately. The main disadvantages are that the PL signal coming from the indentation could be very weak due to the low ratio between the areas of indented zones and strain-free regions which are illuminated by the laser, and that the diffraction limit of visible light impedes us to know the exact position of the indentation in the μPL setup. One way to solve this issue is to place the indentations close to the edges of the flake or at visually recognizable zones.

The second type of indentations consists of an array of indentations, usually within a matrix (See Figure 6.2). The usual spacing between these indentations is 100 nm - 200 nm. Each indentation within a matrix is performed with the same parameters as the others, this leads us to the main advantage: the PL signal from

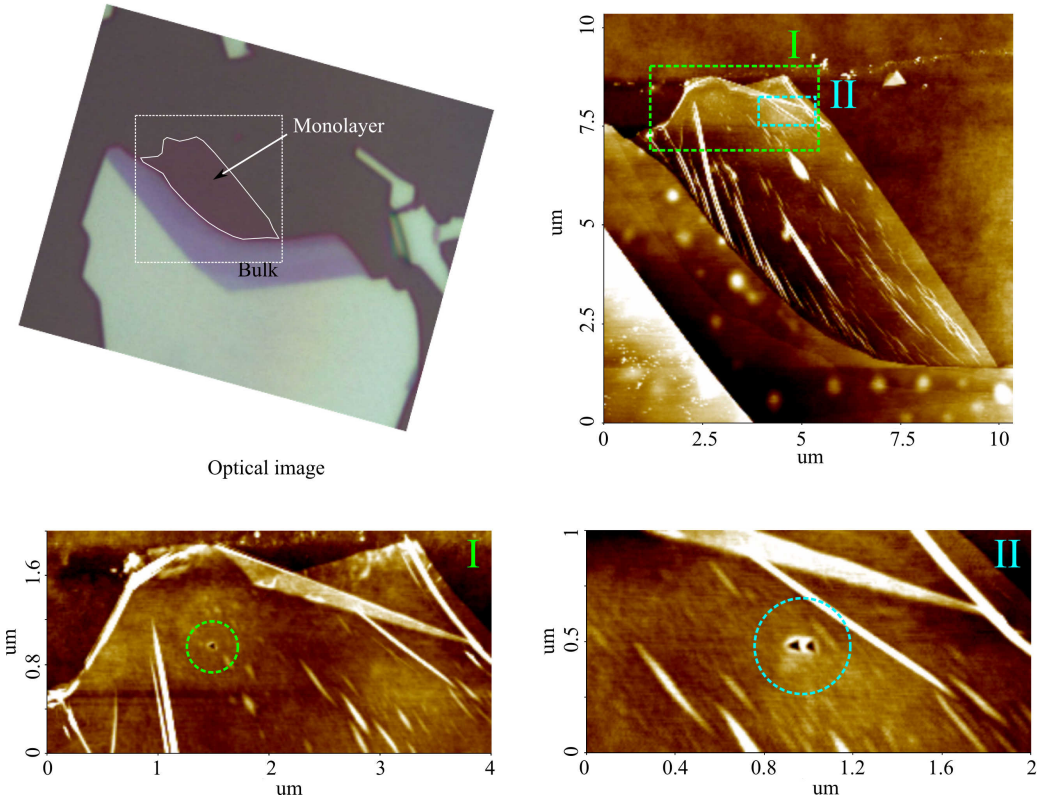

Figure 6.1 Single indentations of MoS_2 on PMMA substrate. From up-left to down-right: optical image of the flake, general AFM topograhpy of the flake and zoom to single indentations.

matrix indentations should be enhanced, since we are measuring the photoluminescence of many "nearly identical" indentations, where the ratio of the areas of strained to the strain-free fields is being increased. Unfortunately, the main disadvantage of this type of indentation is that while building the matrix, each single indentation will pre-stress the membrane for the next indentation, then the strain field is progressively incremented until the material fails and suffers a tear, as shown in Figure 6.3. We have observed that the stress is of the order of the 11% of the bulk modulus of MoS_2 for the tearing to occur.

As discussed above, we expect all indentations to be the same in a matrix arrangement, but this is not what actually happens: the randomness in the indentation's size is mostly due to the plastic hysteresis of PMMA, but also because the same force could produce different ls and εs such that equation (6.4) still holds. Then there exists a not controllable parameter in the nanoindentations and it may be either the size or the mean strain. However, the best way to ameliorate this situation is to search for a *perfectly plastic* substrate, in which the material does not return to its original shape and the size of the indentation be accurately determined by the apex angle of the AFM tip. We also point out that when 2.4 V is used as the setpoint voltage, the mean indentation size was 25 nm - 40 nm: this size is still large for our requirements. One possible way to solve this issue is to try using other more viscous polymer substrates to obtain a more plastic behavior.

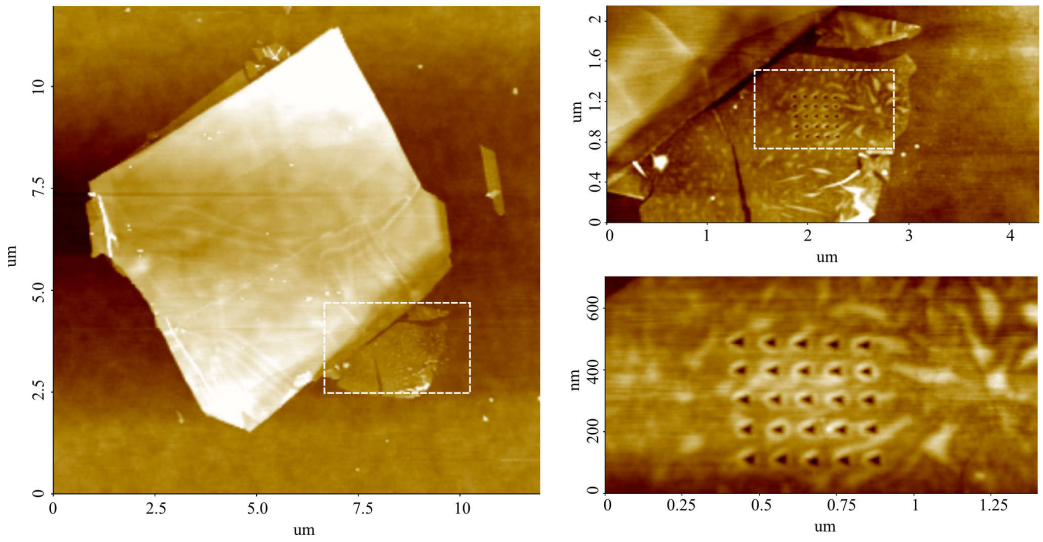

Figure 6.2 AFM matrix of indentations of MoS_2 on PMMA substrate performed with 2.6 V force.

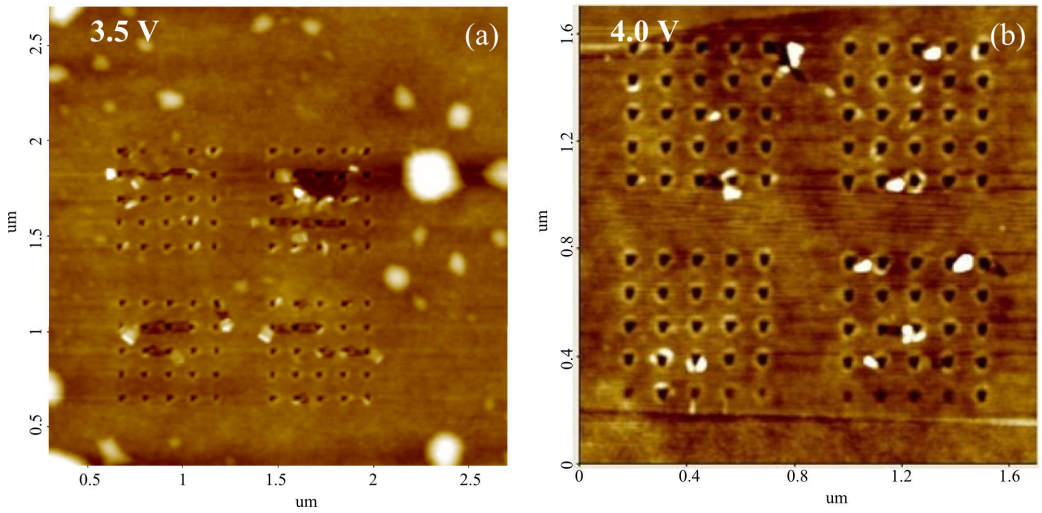

Figure 6.3 Examples of torn matrices of indentations. In the upper-left corner we show the force used in the indentations.

For now, we will focus on the characterization via PL and Raman spectroscopy of each type of indentations in order to decide which one of the methods gives the best results about exciton confinement.

6.2 Photoluminescence and Raman spectroscopy of MoS_2 and indentations

The optical attributes of MoS_2 monolayers have been mostly studied via photoluminescence and Raman spectroscopy. The main features of PL spectra have been already discussed in the Chapter 2, as well as the aspects of the Raman spectrum. Now we present the results of the optical characterization of MoS_2 layers and discuss what is changed when indentations are performed in monolayers. We begin

with the Raman spectrum shown in Figure 6.4: the two optical E' and A'$_1$ modes are dependent on the strain, but E' is more sensitive than A'$_1$ for strained monolayer; the shifts with respect to the relaxed membrane is about 0.2 cm^{-1} for E' and 2.3 cm^{-1} redshift for A'$_1$, which indicates that in-plane vibrations are more affected by deformation than out-of plane ones. This is easily explained by the fact that tensile strain modifies more the Mo-Mo and Mo-S interatomic distances than the vertical S-S distance, then in-plane strain is always greater than out-of-plane.

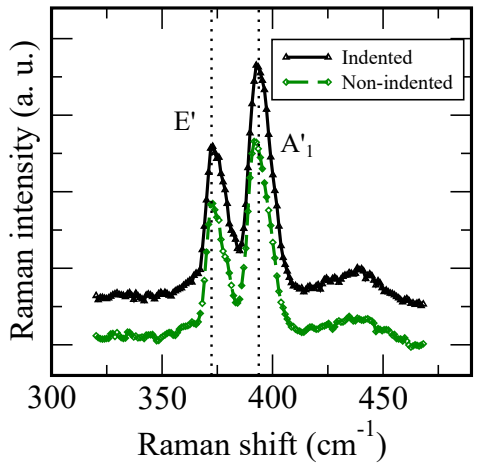

Figure 6.4 Raman spectrum for (a) unstrained and (b) ∼2.3% strained monolayer MoS_2.

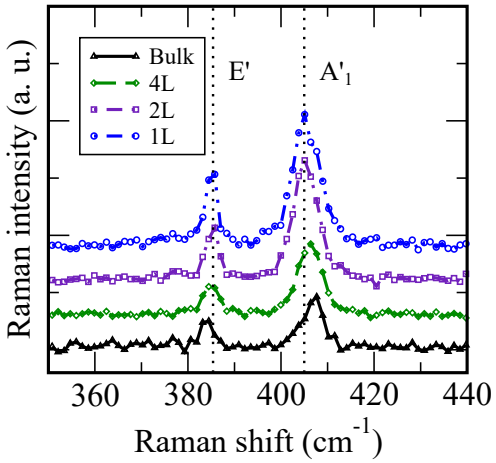

Figure 6.5 Raman spectra for different number of layers in MoS_2-PMMA.

The Raman spectrum - based characterization of the strain is difficult to be performed for the case of nanoindentations because of two facts: the first is that indentations are too small compared to the area that is being sampled in the micro-Raman, then the features of the indentations could be eclipsed by those of unstrained region. The second fact is that every indentation also pre-stress its surroundings, and the presence of wrinkles or tears could generate more complicated strain fields, making it troublesome to establish the reference spectrum of a unstrained relaxed MoS_2 membrane [96]. These are the reasons why we do not devote more interest on Raman spectroscopy along this work; we just relegate this technique to characterize the number of layers of MoS_2: in Figure 6.5 we show our most relevant results on this characterization on PMMA substrates. The mean E'-A'$_1$ separation we found for monolayers in our samples was 19.5 cm^{-1}, for bilayers 21.4 cm^{-1} and for four or more layers >24.2 cm^{-1}.

Different types of PL measurements were performed in various dependences of ICEX-UFMG due to the specific facilities of each laboratory. For example, in the *Laboratory of Raman Spectroscopy* we measured high signal-to-noise ratio spectra in the range 530 nm - 800 nm, but the main issue was that the diffraction grating (1800 lines/mm) needed at least twelve wavelenght windows to acquire the whole spectrum. In the *Laboratory of Semiconductors* we performed more satisfactory PL measurements because of the facilities provided by the piezoelectric device *attoCube* which allows to control suitably the position of the excitation on the sample.

We also performed measurements in the *Laboratory of Spectroscopy* in which the setup for hyperspectra was equipped. These measurements at room temperature provided relevant information about the borders of the flakes and indentations which will be discussed in this chapter. For now, we organize our PL results by the temperature at which spectra were measured as follows: in Section 6.2.1 we address the room temperature measurements for both single indentations and matrices-of-indentations. Similarly, in Section 6.2.2 we discuss low-temperature measurements in the same manner as that for room temperature.

6.2.1 Room temperature PL

Most of the measurements were performed in this regime because MoS_2 luminesces at room conditions. Some features of room temperature results such as peak broadening and shift of the PL will be addressed in this section. Photoluminescence spectra for both unstrained MoS_2, single and matrix indentations are shown in Figure 6.6, where violet (black) dots in (a) and (b) correspond to spectra of a nearby unstrained (indented) region. Unstrained spectra show the characteristic two luminescence peaks that describe the recombination of A and B exciton at ~ 1.81 eV and ~ 2.02 eV, respectively. Exciton A peak is indeed composed of two contributions: one from exciton A itself and other for a negatively charged exciton, or *trion*, whose energy is slightly lesser than that of the neutral A exciton (20 meV lesser) due to the interaction with an additional electron in CB; these curves are well-fitted with three or four *Voigt profiles* (as seen in Figure 6.7). A Voigt profile is the convolution of a gaussian and a lorentzian curves, and is used to describe cases in which both *homogeneous* and *inhomogeneous* broadening are present.

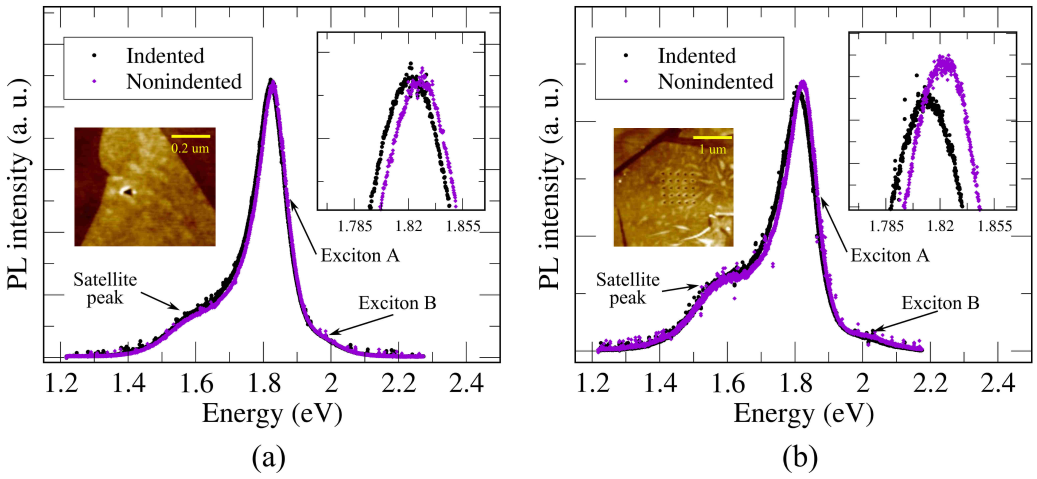

Figure 6.6 Photoluminescence spectrum at room temperature for (a) single indentations and (b) matrix of indentations. Violet dots represent the spectra for unstrained regions and black dots for strained. Insets show a detail of the redshift due to strain and the topography of the indentation.

In most of our room temperature spectra, Voigt curves were used for the fitting due to the predominance of inhomogeneous broadening. We chose four of them in order to fit the exciton B, exciton A, charged exciton and one broad line that

helps to fit the 1.5 eV - 1.8 eV part of the spectrum that we will name as *satellite peak*. We do not expect any isolated peak in this region because the high carrier-carrier and carrier-phonon scattering in this material at room temperature increases the rates of non-radiative processes and impedes the thermalization of the excitons within the nanoindentations. We also see that the indentations provoke a strain in the material, lowering the exciton recombination energy. Figure 6.6 shows the effect of the strain in the membrane due to a single indentation and to a matrix of indentations: in the case of a single indentation (a), the strain is low and the redshift (8 meV) is lesser than that of a matrix of indentations (13 meV). This is an expected result from our considerations about tensile strain in MoS_2: the more the membrane is stretched, the lesser is the exciton recombination energy. We also point out that a low tensile strain should not affect significantly the intensity of the exciton A emission, because local small variations of the strain field do not produce any effect of exciton funneling, while large and extended variations could produce it. Among other interesting features of the photoluminescence at room temperatures, as shown in Figure 6.6, we find a broad satellite peak centered barely at 1.6 eV which is not expected from the theory of exciton emission. In some cases, such as in Figure 6.6 (b) the intensity is appreciable: it may come from some effect of the MoS_2 on the polymer substrate, or from a residual strain along the flake. We discard the funneling phenomena as a possible explanation because the width of the peak is not expected to be so large. Another feature of the spectra at room temperature was the low (almost negligible) intensity of B emission, this can be due to the spin population alterations in the flake or an interaction with the polymer substrate. A fact that supports this argument is that we observed the B intensity to vary as we move from one PMMA-substrate sample in to other also made of PMMA, then this feature may depend on the way the samples are prepared.

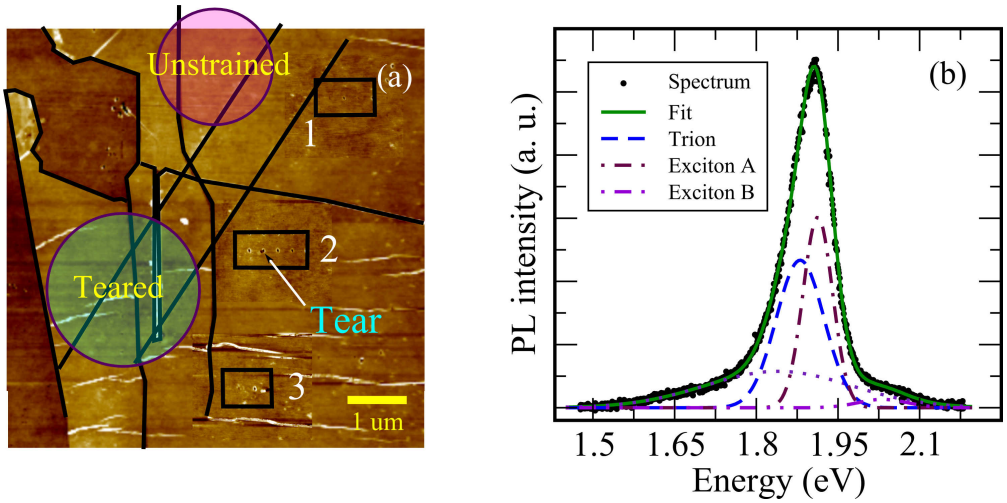

Figure 6.7 Photoluminescence hyperspectra at room temperature. (a) AFM image of the MoS_2 flake, (b) a typical PL spectrum and intensity.

We used the technique of the hyperspectra to study the photoluminescence in matrices of indentations at room temperature. Figure 6.7 shows the hyperspectra

analysis of one sample that has three matrices of indentations labelled as 1, 2, and 3, as seen in the AFM topography of Figure 6.7 (a). The indentations in matrix 1 were not uniform, and the effective strain in each indentation oscillates between 0.41% and 4.6% which makes it difficult to predict any phenomena in this region. On the contrary, matrix 2 has mainly high values of strain which range between 3% and 6%. Additionally, one of these indentations produced a tear, relaxing the membrane. As well as those of matrix 1, indentations in matrix 3 were not uniform and suffered some tears. We chose a region which contains all three matrices in the hyperspectra to analyze any emergent phenomena.

Some wrinkles and tears of the sample are marked in the AFM image with solid black lines to guide the eye of the reader. Additionally, we mark with circles in Figure 6.7 (a) two other relevant regions of the map: the *unstrained region* which is the most clean zone of the image, is used to extract the reference PL of unstrained MoS_2. The *torn region*, which is the zone with the largest number of wrinkles and tears, is used for studying the effects of membrane relaxation due to tearing in the PL.

Due to the large laser spot size ($\sim 1\ \mu$m) compared to the typical sizes of the indentations and the matrices of indentations, there exists an additional difficulty: in a typical 10 μm x 10 μm hyperspectra we measure about 32 spectra along a line, resulting in the measurement of PL of points which are separated 300 nm, which is a distance smaller than the laser spot size; this leads to an issue known as *oversampling* of signals. One way to correct the oversampling is to perform a deconvolution of the hyperspectra with the profile of the laser spot. Typically, the spot has a gaussian profile [3], then the deconvolution may be performed numerically with this hypothesis.

We swept over a 7 μm x 7 μm region in such a way that it covered a portion of the PMMA substrate, plus a part of the unstrained MoS_2 monolayer as well as the matrices of indentations. We also marked some wrinkles and tears in the flake because they might produce some shifts in the spectrum. With these considerations, we are able to detect any phenomena at the edge of the flake by characterizing the shifts on the intensity, position and width of the different peaks that compose the PL spectrum at each point in the sample. In order to achieve that, we fit each spectrum with four Voigt curves, as shown in Figure 6.7(b): as we move along the sample, we study separately the contribution of each line to the PL. We present the results of our measurement of hyperspectra in Figures 6.8, 6.9 and 6.10 which show the intensity, position and linewidth maps for the satellite, trion and exciton A peaks.

In our analysis of the emission intensity from Figure 6.8, we observed an abrupt increase of the emission at the edge of the flake and it remains the same until a sudden decrease occurs in the leftmost part of the flake. The contribution of the satellite peak does not exhibit any appreciable change of the intensity when approaching to the indentation matrices, as shown in Figure 6.8 (b). However, the A emission from the matrix 2 is strongly suppressed while the trion emission is

[3]This is true for gas lasers, but may be no longer valid for the 488 nm diode laser that we used because the emission for diode lasers is not as coherent as that of gas-based lasers; nevertheless we assumed a gaussian shape for the beam as a first approximation.

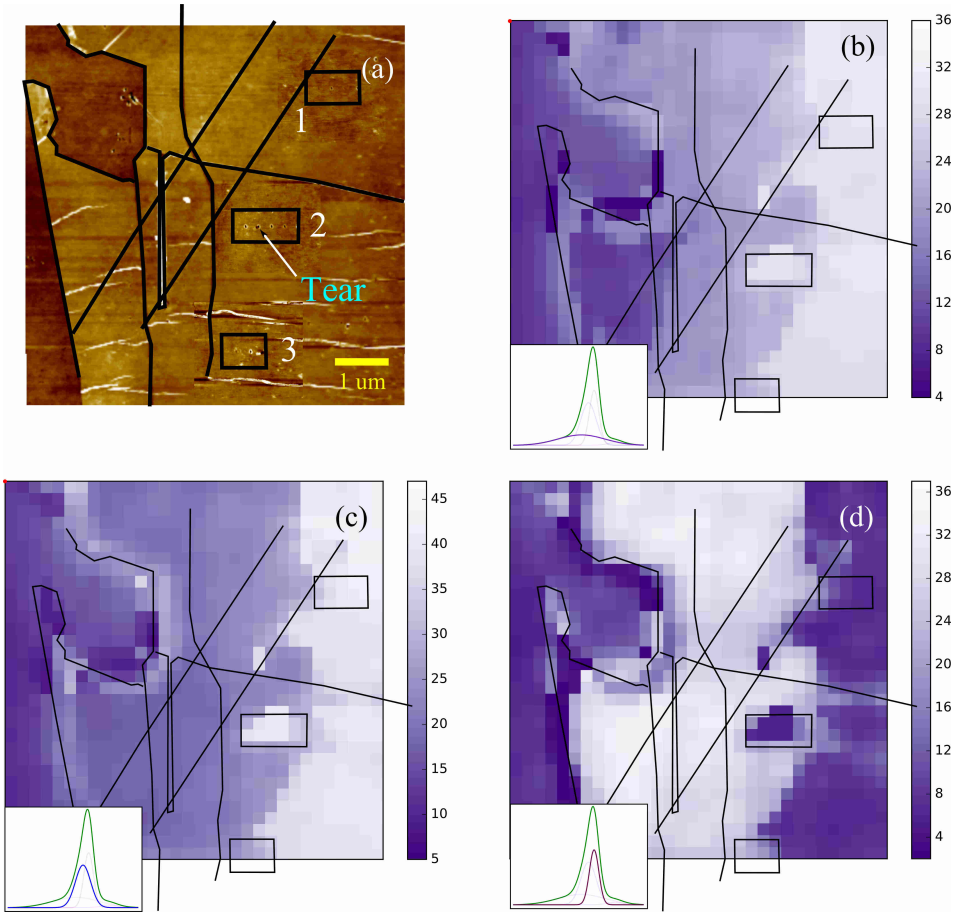

Figure 6.8 PL-intensity hyperspectra at room temperature. (a) AFM image of the MoS_2 flake, the (b) satellite peak, (c) trion and (d) exciton A contributions.

increased (See Figures 6.8 (c)-(d)), possibly due to an interplay between the intensities of trion and A emission in the fitting. We will return to this discussion later to expose first the rest of the results of hyperspectra.

In order to analyze the shifts in the peak position for each contribution we generated a color-scale (in eV) in which red means redshift and blue means blueshift, as displayed in Figure 6.9, taking as reference the peak position at an unstrained region of the map. The satellite peak in Figure 6.9 (b) shows a strong redshift at the borders and the torn region of the flake, but it is almost insensitive to the variation of the position along the map. The same behavior is displayed by the trion peak in Figure 6.9 (c), but a slightly larger blueshift ($\sim$10 meV) is observed at the matrix 2 in Figure 6.9 (d). This is opposite to the expected for strained MoS_2, where a decrease in the band-gap energy is manifested as a redshift of the A emission. Further discussion about this point will be combined with the interplay of trion and A emission, later in this chapter.

Other feature in the hyperspectra is that of the linewidth, as shown in Figure 6.10, using a color scale that displays in eV whether the peak is narrowed (negative values) or broadened (positive values) compared to a reference spectrum in an

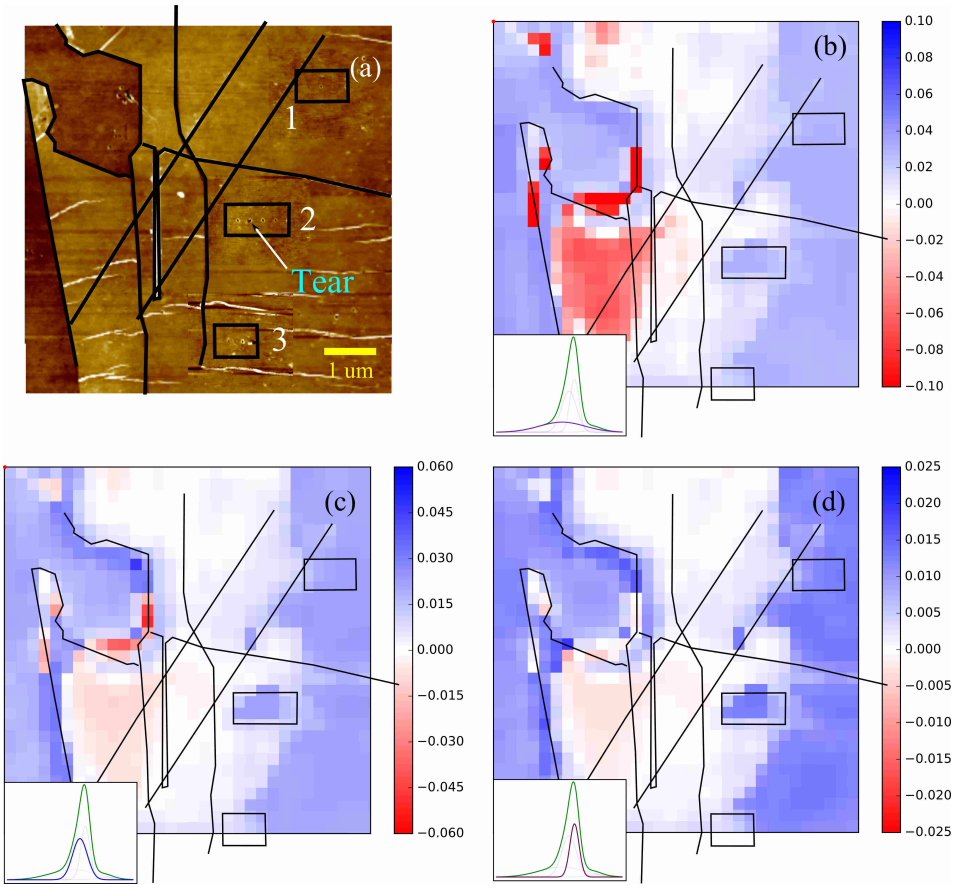

Figure 6.9 PL-shift hyperspectra at room temperature, taking as a reference the spectrum of an unstrained position of the sample. (a) AFM image of the MoS_2 flake, the (b) satellite peak, (c) trion and (d) exciton A shifts.

unstrained region of the map. For the torn region of the map, the satellite (b) and the trion (c) peaks have opposite behaviors: while the satellite peak is strongly narrowed, the trion is broadened. Then there is a correlation between the the satellite and trion peaks, which may come from the fitting optimization of the spectra: the fitting routine may have generated a spurious interplay between peaks. The exciton A (See Figure 6.10 (d)) peak is strongly narrowed in the matrix 2, as well as for the satellite and trion peaks, then the matrix of indentations produces an overall narrowing of the spectrum.

Now, we return to our discussion about the interplay between the trion and A intensities, which is somehow related to the fact of having observed an unexpected blueshift of the A emission. Thus, this interplay may cause either an energy shift of the maximum of the intensity or a slant of the shape. In some areas of the map, such as in the border of the flake, a strong blueshift is also observed, then we may compare the nature of the blueshift in the border to that of the blueshift in the matrix of indentations. To achieve that, we analyze the shape of the spectra at different points of the sample, such as at the border, at the unstrained region and at the indented part of the map.

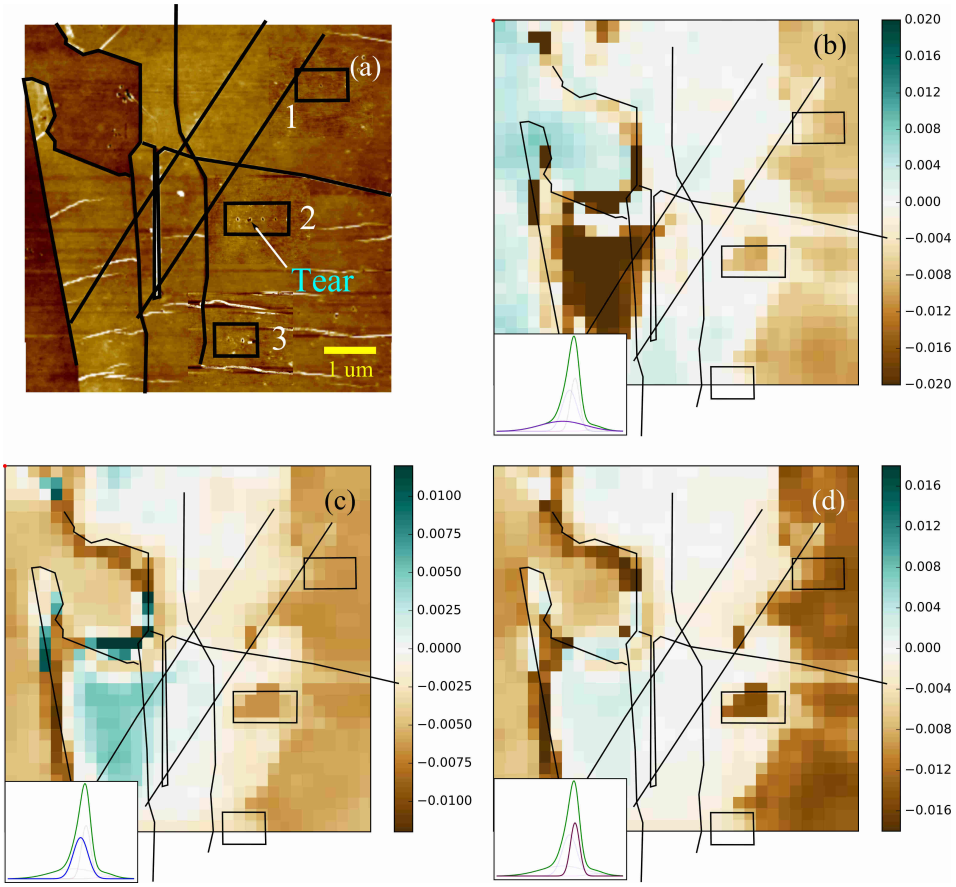

Figure 6.10 PL-linewidth hyperspectra at room temperature. (a) AFM image of the MoS_2 flake, the (b) satellite peak, (c) trion and (d) exciton A linewidth.

Figure 6.11(a) shows a sequence of points labeled from 1 to 4 which represent two points in the unstrained region, a point within the matrix of indentations and a point at the edge of the flake, respectively. The black curve in part (b) shows the difference between the two nearby 1-2 points, which is mainly white noise. The green curve shows the difference between unstrained zone and the matrix; there are three shifts of 1-3 from positive to negative values, which means that the slant of the spectrum is affected by the strain. In contrast, the violet curve (that corresponds to the 1-4 shift) displays just one shift of sign, which means that the spectrum does not change its shape but is shifted to the red. From these facts we could conclude that the effect of the indentations is to distort the spectrum, probably by increasing the emission from charged excitons compared to that of neutral excitons. In the same way we asseverate that there is an energy shift of the emission at the edge of the flake, but the nature of this shift is not clear.

Room temperature PL-hyperspectra displayed some features such as blueshift of A emission, slant of the spectrum and overall spectrum narrowing due to the presence of indentations. Nevertheless, the phenomena that we are expecting to emerge due to the indentations should actually be manifested in the lowest energy region of the spectrum, because the confined exciton emission from quantum dots lie on

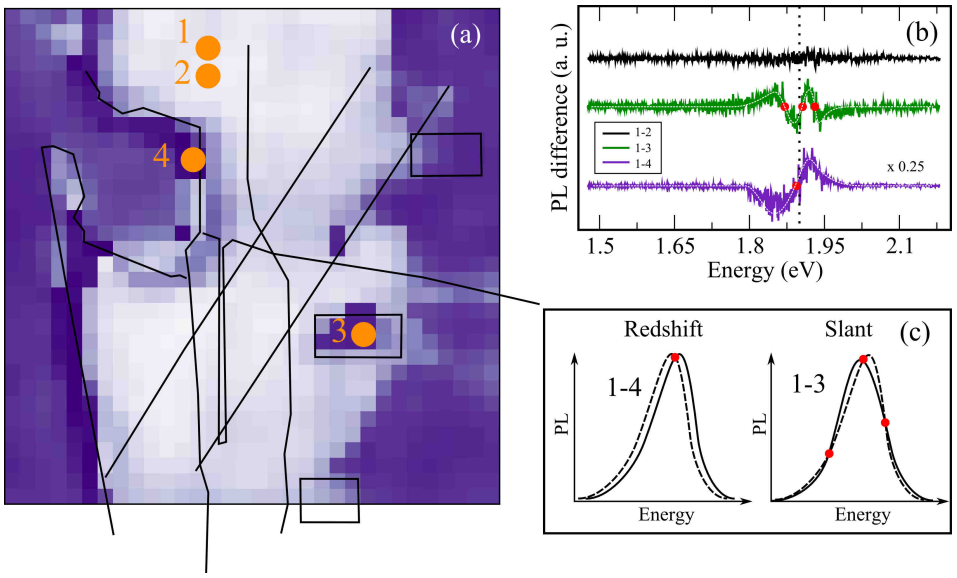

Figure 6.11 Color online. Analysis of the shape of the spectra: (a) Map of the intensity of exciton A; points *1* to *4* show the points in which the spectra were analysed. (b) difference of normalized PL of 2, 3 and d with respect to 1. (c) scheme of the PL redshift as observed in 1-4, and slant as observed in 1-3.

energies close to 1.55 eV or lower, according to our calculations. As discussed in previous chapters, these phenomena is not observable at room temperature, reason why we dedicate the next section to analyze our low-temperature measurements.

6.2.2 Low temperature PL

We lowered the temperature of the MoS_2 monolayer over PMMA to 10 K to investigate the emission from the indented membranes at a temperature regime in which confinement of excitons could appear. In order to make a comparative analysis between these two temperature regimes, we chose the same sample whose spectra at room temperature were presented in the last section and measure the PL at the same positions. The AFM topography is shown in Figure 6.12 (a) in which we marked the two points, one inside and the other outside the matrix of indentations 2: in this manner we studied the PL for both strained and unstrained MoS_2 and also for both room and low temperature.

It is known that as the temperature is lowered, the band-gap increases due to thermal dilatation effects and reduced electron-phonon interaction [97], therefore the position of exiton A peak is blueshifted. Low temperature also favors the emergence of other emission peak which come from the emission of excitons bound to surface defects of the lattice; this is called the *exciton S peak* and appears at a lower energy than that of exciton A peak at room temperature, explaining the bound character of this type of exciton [98]. These features are shown in Figure 6.12 (b), which displays the PL at position 2 for both room and low temperatures. The reason why it is not possible to observe the exciton S at room temperature is the same why the confinement of excitons cannot also be observed: the thermal fluctuations

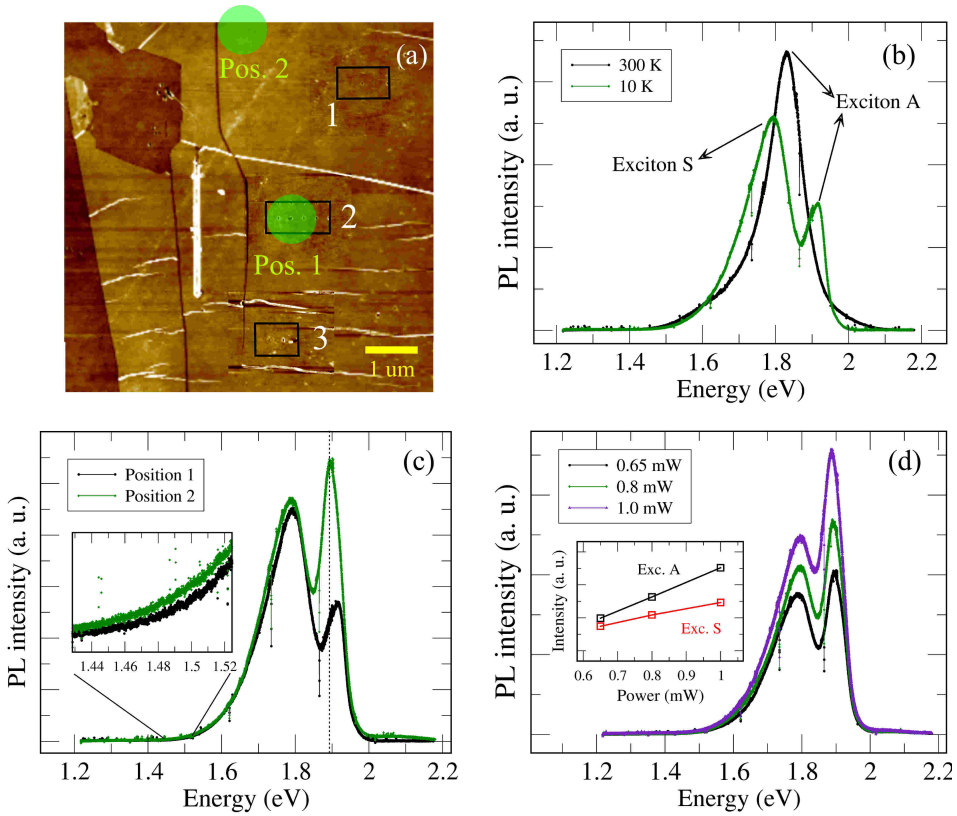

Figure 6.12 Photoluminescence at 10 K for indented MoS_2 on a PMMA substrate. (a) shows the sample and the positions at which the PL was measured, (b) shows the emission at point 2 at both room and low temperatures. (c) shows the spectra at low temperature at both positions and (d) the power dependent spectrum at position 2.

imprint enough energy to the excitons to be scattered out of the defects, then the emission of bound S excitons is decreased.

Moreover, surface defects are randomly (say, uniformly) distributed along the flake, therefore there should not be any spatial dependence of the emission of exciton S: this is one of the features that we show in Figure 6.12 (c), in which the PL was measured at both positions for the same 10 K temperature. The intensity of exciton S is unchanged, as expected, while the exciton A is strongly affected by the position; more specifically, the emission of exciton A is lowered and *blueshifted* at the matrix of indentations by 19 meV. One possible consequence of this phenomenon is that the blueshift observed in the part (c) actually corresponds to a reduction of the population of charged excitons (or electrons) when moving towards the matrix of indentations. The fact that supports this assertion is that the right-side (blue-side) of the exciton peak is the same for both spectra: if there were any shift, the sides of the peaks would not match, just as depicted in Figure 6.11 (c) for a typical shift; therefore, the blueshift observed here would follow more a change in the weights of the emission from neutral and charged excitons. Inset in the part (c) shows the 1.44 eV - 1.52 eV region of the PL in which we expected to observe some features of quantum dot emission; however, there is no such manifestation, maybe due to the

still high power used to excite the sample (0.6 mW). This could mean that even at 10 K the excitons are strongly scattered out of the matrix of indentations and then there is no emission from the quantum dots. That could also mean that the QDs saturate and their PL is low compared to the high background emission.

Another feature observed for the PL as a function of the excitation power matches with the reviewed in the literature: both peak A and peak S are power-dependent, as shown in Figure 6.12 (d). The A peak is expected to grow linearly with power, since the number of excitons created per unit area per unit time are linearly related to the number of incoming photons per unit time per unit area that excite the sample. Nevertheless, peak S is expected to grow sublinearly because of the defect-like nature of its emission: once all the defects at the MoS_2 surface are saturated, the emission does not increase anymore with the power [98]. From this observation we deduce that there exist a large number of surface defects in the crystal since the behavior of the intensity for peak S is still linear in the power regime studied.

In this chapter we exposed the main results of the experimental part of our work: we addressed the physics and the achievement of nanoindentations via the AFM in MoS_2 over PMMA substrate: we found that 2.4 V setpoint voltage was an optimum value that permitted us to perform small indentations (a few tens of nm diameter), although we needed sizes lower than 15 nm. We also showed the features of the Raman spectrum that depend on the strain and on the number of layers, and found that A'_1 Raman mode is strain-dependent, while both E' and A'_1 modes tend to separate when increasing the number of layers. Finally we showed the results on single PL and hyperspectra at room and 10 K temperature.

PART III

CONCLUSIONS AND FUTURE WORK

Conclusions and issues

In this work we described theoretically the generation of quantum dots in atomic monolayers of molybdenum dysulfide and characterized their emission by means of the photoluminescence spectrum. Although the photoluminescence measurements in both room- and low-temperature regimes did not show the enough evidence to demonstrate the generation of the dots, we exhaustively explored the experimental difficulties that lead to these results. We organize the specific conclusions as follows:

Conclusions from the theoretical predictions

We described the exciton attributes such as total energy, binding energy and effective mass by means of the $k \cdot p$ *perturbation theory*, which used the results of *ab initio* calculations and symmetry considerations found in the literature. Later, we related these properties to the strain via deformation potential and obtained a first-order expression for the exciton energy as a function of the local strain; then we stated our hypothesis of exciton confinement via the nanoindentation in which a quantum dot could be generated through the strain field induced by a AFM-based nanoindentation of a MoS_2 monolayers. Using this hypothesis we built a criterion for the generation the quantum dots in the laboratory and supported that criterion with some examples and simulations of exciton wavefunctions within the nanoindentation.

Experimental conclusions

Provided the theoretical predictions we created some different samples of MoS_2 monolayers over a poly-methyl-methacrylate (PMMA) substrate. This substrate was the best available polymer that satisfied the requirements of elasticity-plasticity for nanoindentations. AFM-based characterization of the topography revealed that the substrate was uniform, but the MoS_2 flakes often showed several wrinkles which were a symptom of a pre-strained membrane.

Our main findings are that at room temperature, the strain causes a slant on the shape of the peak A: this slant comes from a shift of the populations of neutral and charged excitons in the area of the indentations. The redshift of peak A due to the strain generated by an indentation is low (a few meV for 2% strain at the indentation): this is because we are actually observing the overall strain field which is slightly affected by an indentation, while the signal that comes from the indentation is very low or nonexistent, probably due to the short exciton lifetime that impedes the population of the confined levels in the indentation before the recombination.

For low temperatures we observed the emergence of the peak S in the PL spectrum: this peak comes from exciton emission at surface defects. Peak S intensity is constant along the flake since the surface defects are uniformly distributed. The apparent blueshift of peak A at the indented zone could actually be due to an exchange of population between neutral and charged excitons wen approaching to the

strained zone: the exciton A intensity increases at the indentations while the trion intensity decreases and vice-versa.

The overall conclusion of our PL measurements is that the main features of the indentations occurred at the highest energy part of the spectrum: redshifts and slants. Nevertheless the phenomena that we expected, such as narrow and intense lines at low energy (say, 1.5 eV) were not manifested at 10 K for 30 nm-sized indentations. This was because the size of the dot was not suitable for the measurements performed at such temperature. The most suitable size calculated to achieve exciton confinement in a nanoindentation was 15 nm at 4 K.

Issues and perspectives

Along our research we faced several difficulties of both theoretical and experimental nature; although all the theoretical problems were just related to the lack of a consensus in the literature around the *ab initio* calculations and related quantities, such as the gap energy, the effective mass of the carriers, the deformation potentials and other relevant parameters which are used in the $k \cdot p$ and tight-binding theories. Experimental difficulties were more diverse and related to the nanoindentation process, the photoluminescence measurements and the temperature issues.

The nanoindentation-related issues were the proper characterization of the elastic-plastic regime of the PMMA substrate in which we consider only a macroscopic model of indentation, neglecting the molecular scales of the nanoindentations. There was also a difficulty on the measurement of the shape of an indentation: only the indentation depth and width were measured, neglecting the complicated shape of an indentation which comes from the combination of elastic and plastic properties of both MoS_2 and PMMA in the process of indentation. We also noticed that there exists an underestimation of the strain because the size of the probe is always comparable to the dimensions of the indentations: the calculated uncertainty in the measurement of strain is about 0.001, which may lead to an error of 50% in the measurement of the strain. Other common issue in matrices of indentations was the strain field generated between two adjacent indentations which is difficult to quantify and sometimes so large that it produced tears that relax completely the membrane, damaging all neighboring indentations.

Photoluminescence was also difficult to be performed because we were not able to use a technique which conciliate both the low temperature and spatial resolution needed to characterize properly the quantum dot emission. We also point out that the excitation power and energy create electron-hole pairs of high energy in their respective bands and may recombine much before thermalizing inside the quantum dot, which allow just a few states within. One possible solution to these issues could be to apply the same scheme of the hyperspectrum measurement to a sample mounted on a cryostat and pump it with a low-power laser of wavelenght larger than 700 nm such that we can excite the quantum dots near-resonantly and avoid the creation of excitons outside the indentations.

There was also an issue related to the temperature and the thermal processes at low temperature: the sample never reached the 4 K temperature at which the

quantum dot features were expected to be manifested. Instead, the minimum temperature measured in the cryostat was 9 K, which is still high for the phenomena that we predicted. One possible solution of this issue is to decrease very slowly the temperature of the sample until it reaches 4 K. Processes such as thermal relaxation of PMMA at low temperatures have been studied: although these processes could be troublesome, they have been reported to occur at temperatures well below 1 K [99]. Even thought the thermal expansion coefficient of PMMA is well-known for temperatures greater than -50 °C, it remains unknown for low temperatures, making it difficult to describe quantitatively the structural properties of PMMA in the low temperature regime.

Finally, we recall that a categorical demonstration of the generation of quantum dots in MoS_2 via nanoindentation should reflect the single-photon nature of the emitter: this can be performed through a measurement of correlation functions. Quantum dots are artificial atoms indeed, then the transitions occurring in them involve the emission of a single photons whose statistics are characterized by the second-order correlation function. A typical setup for this measurement is known as the *Hanbury-Brown-Twiss* experiment (HBT) which counts the coincidences of the arrival of a photon at one detector and that of a second photon at other detector which is delayed some time τ in relation to the arrival of the first photon. A measure of this kind is also regarded as a perspective of future work in this direction.

A

COMPLETE CALCULATION OF THE EXCITON WAVEFUNCTION

As stated in Chapter 1, the electronic states of the band-edges are mixtures of Mo $4d$ and S $3p$ orbitals. In the K points, the d orbitals can be divided in three irreducible representations: $A'(d_{z^2})$, $E'_1(d_{xy}, d_{x^2-y^2})$ and $E''(d_{xz}, d_{yz})$. In the monolayer limit, reflection symmetry in the z axis allows hybridization between A' and E'_1 orbitals. Figure A.1 shows the band-edges in the neighborhood of K and K' points, and depicts the electronic state in the CBM and VBM mainly as Mo $4d$ orbitals. We label these states as $|\phi_c\rangle$ and $|\phi_v\rangle$ for the CBM and VBM respectively.

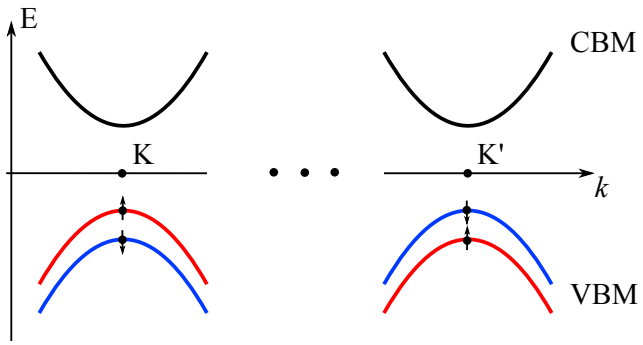

Figure A.1 Approximate parabolic band structure near K and K' points. VB is split between spin-up (red line) and spin-down (blue) at K and K', resp.

Therefore, the states of CB and VB can be written as $|\phi_c\rangle = |\phi_c\rangle' \equiv |d_{z^2}\rangle$, $|\phi_v\rangle \equiv (|d_{x^2-y^2}\rangle + i|d_{xy}\rangle)/\sqrt{2}$ and $|\phi_v\rangle' \equiv (|d_{x^2-y^2}\rangle - i|d_{xy}\rangle)/\sqrt{2}$, respectively. We could define a more compact notation by introducing the valley index τ which is defined as +1 for K valley and as -1 for the K' valley. In this manner we can write the VBM state as $|\phi_v^\tau\rangle = (|d_{x^2-y^2}\rangle + i\tau|d_{xy}\rangle)/\sqrt{2}$. We can construct a suitable basis to treat the single-particle states in monolayer MoS_2, then we use the *Dirac fermion formalism* to describe a two-fold spinor whose components are the $|\phi_c\rangle$ and the $|\phi_v^\tau\rangle$ states of the band-edges. The notation follows:

$$|\phi_c\rangle = \begin{pmatrix} 1 \\ 0 \end{pmatrix} \qquad |\phi_v^\tau\rangle = \begin{pmatrix} 0 \\ 1 \end{pmatrix}. \tag{A.1}$$

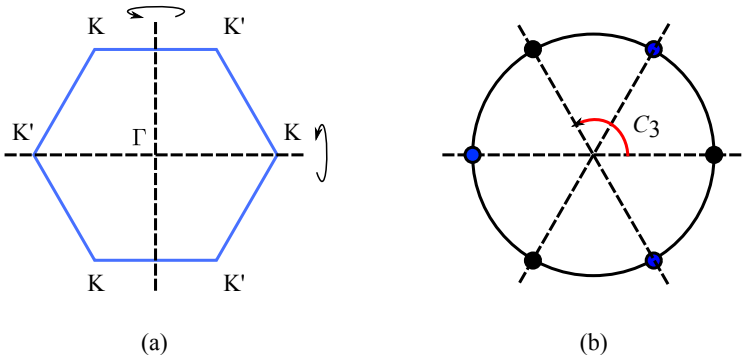

Figure A.2 Symmetry in the hexagonal lattice. (a) Symmetry in the reflection about an axis, (b) Rotation symmetry in the C_{3h} group.

We use some considerations about symmetry to identify which momentum elements are zero. In Figure A.2 (a) we see that K and K' are related through a reflection about the vertical (and horizontal) axis: $(K'_x, K'_y) = (-K_x, K_y)$, thus we could use a compact notation to describe $\mathbf{q}$ by redefining the lowering and raising operators: $\mathbf{q}_\pm = \tau q_x \pm i q_y$. The Figure A.2 (b) describes the symmetry of a three-fold rotation C_3 of $2\pi/3$ in an hexagonal lattice; the effect of such rotation in the states and the operators is:

$$C_3|\phi_v\rangle = C_3|A'\rangle = |A'\rangle, \qquad C_3|\phi_v\rangle = C_3|E'_1\rangle = e^{2i\pi/3}|E'_1\rangle$$
$$C_3 P_\pm C_3^\dagger = e^{\mp 2i\pi/3} P_\pm \tag{A.2}$$

Therefore, as $C_3^\dagger C_3$ gives the identity matrix, then we can calculate for example the $\langle E'_1|C_3^\dagger C_3 P_\pm C_3^\dagger C_3|A'\rangle$ entry, which must be equal to $\langle E'_1|P_\pm|A'\rangle$, then

$$\langle E'_1|C_3^\dagger C_3 P_\pm C_3^\dagger C_3|A'\rangle = \langle E'_1|e^{-2i\pi/3}e^{\mp 2i\pi/3}P_\pm|A'\rangle = \begin{cases} e^{-4i\pi/3}\langle E'_1|P_+|A'\rangle, & P_+ \\ \langle E'_1|P_-|A'\rangle, & P_- \end{cases}$$

We see that $\langle E_1'|P_+|A'\rangle = e^{-4i\pi/3}\langle E_1'|P_+|A'\rangle$ requires $\langle E_1'|P_+|A'\rangle = 0$, thus the only nonzero $\langle E_1'|H_{\mathbf{k}\cdot\mathbf{p}}|A'\rangle$ entry is given by $\langle E_1'|P_-|A'\rangle$. In this manner, we can construct the $\mathbf{k}\cdot\mathbf{p}$ hamiltonian as

$$H_0 = at(\tau k_x\hat{\sigma}_x + k_y\hat{\sigma}_y) + \frac{\Delta}{2}\hat{\sigma}_z, \tag{A.3}$$

where a is the lattice parameter, t is the hopping integral between neighboring lattice sites, Δ is the electronic band gap and the $\hat{\sigma}_i$s are the usual Pauli matrices.

Using the same notation and the same basis as in Chapter 4, we return to the derivation of the exciton properties at the same point in which we announced this appendix in the Chapter 4. Then, we start with the exciton hamiltonian:

$$H_T = \begin{pmatrix} V(r) & -at(k_{2x} - ik_{2y}) & at(k_{1x} - ik_{1y}) & 0 \\ -at(k_{2x} + ik_{2y}) & \Delta - \lambda + V(r) & 0 & at(k_{1x} - ik_{1y}) \\ at(k_{1x} + ik_{1y}) & 0 & -\Delta + \lambda + V(r) & -at(k_{2x} - ik_{2y}) \\ 0 & at(k_{1x} + ik_{1y}) & -at(k_{2x} + ik_{2y}) & V(r) \end{pmatrix}. \tag{A.4}$$

The hamiltonian (A.4) satisfies the Schrödinger equation

$$H_T\Psi = \varepsilon\Psi \tag{A.5}$$

To simplify our notation, we write the hamiltonian (A.4) as:

$$H_T = \begin{pmatrix} \mathscr{O}_2 + \gamma(\sigma_0 - \sigma_3) + V(r)\sigma_0 & \mathscr{O}_1 \\ \mathscr{O}_1^+ & \mathscr{O}_2 - \gamma(\sigma_0 + \sigma_3) + V(r)\sigma_0 \end{pmatrix}, \tag{A.6}$$

where

$$\mathscr{O}_2 = \begin{pmatrix} 0 & -at(k_{2x} - ik_{2y}) \\ -at(k_{2x} + ik_{2y}) & 0 \end{pmatrix}, \tag{A.7}$$

$\gamma = \frac{\Delta - \lambda}{2}$, $\mathscr{O}_1 = at(k_{1x} - ik_{1y})\sigma_0$ is a nonhermitian operator, σ_0 is the 2×2 identity matrix and the σ_3 is the Pauli matrix defined before in this section. From this point we shall omit the redundant index $\uparrow$ do describe the K valley. The Schrödinger equation (A.5) may be written as the following system of coupled equations:

$$\begin{aligned} (\mathscr{O}_2 + \gamma(\sigma_0 - \sigma_3) + V(r)\sigma_0)\psi_c + \mathscr{O}_1\psi_v &= \sigma_0\varepsilon\psi_c \\ \mathscr{O}_1^+\psi_c + (\mathscr{O}_2 - \gamma(\sigma_0 + \sigma_3) + V(r)\sigma_0)\psi_v &= \sigma_0\varepsilon\psi_v. \end{aligned} \tag{A.8}$$

We can invert the last equation of (A.8) as

$$\psi_v = (-\mathscr{O}_2 + \sigma_0\varepsilon + \gamma(\sigma_0 + \sigma_3) - V(r)\sigma_0)^{-1}\,\mathscr{O}_1^+\psi_c, \tag{A.9}$$

and make a zeroth-order approximation:

$$(-\mathscr{O}_2+\sigma_0\varepsilon+\gamma(\sigma_0+\sigma_3)-V(r)\sigma_0)^{-1}=\frac{1}{\varepsilon\sigma_0+\gamma(\sigma_0+\sigma_3)}+\mathscr{O}\{\mathscr{O}_2,V(r)\}. \tag{A.10}$$

Here, we assumed the kinetic energy and the Coulomb interaction to be weak with respect to the quasiparticle total energy, the gap energy and the spin-orbital coupling. This is justified within a first order perturbation on $V(r)$ and $\mathscr{O}_2$. In this way, we rewrite the first equation of (A.8) as:

$$(\mathscr{O}_2+\gamma(\sigma_0+\sigma_3)+V(r)\sigma_0)\psi_c+\frac{\mathscr{O}_1^+\mathscr{O}_1}{\varepsilon\sigma_0+\gamma(\sigma_0+\sigma_3)}\psi_c=\sigma_0\varepsilon\psi_c. \tag{A.11}$$

Equation (A.11) describes the energy of a bound state in the conduction band; in the coordinate representation we have to write the k_i as differential operators and solve the equation to obtain the wavefunction. We use a separation of the center of mass an the relative motions, by defining a "center of mass" coordinate $\mathbf{R}=\alpha\mathbf{r}_1+\beta\mathbf{r}_2$ and using the following *ansatz*:

$$\Psi_j=e^{i\mathbf{K}\cdot\mathbf{R}}\psi_j(\mathbf{r}), \tag{A.12}$$

where $\mathbf{K}$ is the center-of-mass momentum operator which can be decomposed into the operators $K_\pm=Ke^{\pm i\Phi}=K_x\pm iK_y$, where $\Phi=\arctan\left(\frac{K_y}{K_x}\right)$. In the new reference frame, we can write the derivatives as:

$$\begin{aligned}
K_x&=\alpha k_{1x}+\beta k_{2x}, \qquad K_y=\alpha k_{1y}+\beta k_{2y}\\
\partial_{1x}\Psi&=i\alpha K_x e^{i\mathbf{K}\cdot\mathbf{R}}\psi(\mathbf{r})+e^{i\mathbf{K}\cdot\mathbf{R}}\partial_x\psi(\mathbf{r}),\\
\partial_{1y}\Psi&=i\alpha K_y e^{i\mathbf{K}\cdot\mathbf{R}}\psi(\mathbf{r})+e^{i\mathbf{K}\cdot\mathbf{R}}\partial_y\psi(\mathbf{r}),\\
\partial_{2x}\Psi&=i\beta K_x e^{i\mathbf{K}\cdot\mathbf{R}}\psi(\mathbf{r})-e^{i\mathbf{K}\cdot\mathbf{R}}\partial_x\psi(\mathbf{r}),\\
\partial_{2y}\Psi&=i\beta K_y e^{i\mathbf{K}\cdot\mathbf{R}}\psi(\mathbf{r})-e^{i\mathbf{K}\cdot\mathbf{R}}\partial_y\psi(\mathbf{r}).
\end{aligned} \tag{A.13}$$

Given that $\mathbf{k}=-i\nabla$, thus we can write the identities:

$$\begin{aligned}
k_{1x}&=\alpha K_x-i\partial_x, \qquad & k_{1y}&=\alpha K_y-i\partial_y,\\
k_{2x}&=\beta K_x+i\partial_x, \qquad & k_{2y}&=\beta K_y+i\partial_y,
\end{aligned} \tag{A.14}$$

and hence

$$\begin{aligned}
k_{1x}-ik_{1y}&=\alpha K_- -i\partial_x-\partial_y, \qquad & k_{1x}+ik_{1y}&=\alpha K_+ -i\partial_x+\partial_y,\\
k_{2x}-ik_{2y}&=\beta K_- +i\partial_x+\partial_y, \qquad & k_{2x}+ik_{2y}&=\beta K_+ +i\partial_x-\partial_y.
\end{aligned} \tag{A.15}$$

Equation (A.15) allows us to write the $\mathscr{O}_1$ operator as

$$\mathscr{O}_1 = at(\alpha K_- - i\partial_x - \partial_y)\sigma_0, \qquad \mathscr{O}_1^+ = at(\alpha K_+ - i\partial_x + \partial_y)\sigma_0, \quad \text{(A.16)}$$

and

$$\begin{aligned}\mathscr{O}_1^+\mathscr{O}_1 &= a^2t^2\sigma_0(\alpha K_+ - i\partial_x + \partial_y)(\alpha K_- - i\partial_x - \partial_y)\\ &= a^2t^2\sigma_0\left[\alpha^2K^2 - i\alpha(K_+ + K_-)\partial_x - \alpha(K_+ - K_-)\partial_y - \nabla_{\mathbf{r}}^2\right]\\ &= a^2t^2\sigma_0\left[\alpha^2K^2 - \nabla_{\mathbf{r}}^2 - 2i\alpha(K_x\partial_x + K_y\partial_y)\right], \end{aligned} \quad \text{(A.17)}$$

which is assumed to be hermitian. We replace this result in (A.11) to obtain:

$$\begin{aligned}&(\mathscr{O}_2 + \gamma(\sigma_0 + \sigma_3) + V(r)\sigma_0)\psi_c +\\ &+\frac{a^2t^2\sigma_0\left[\alpha^2K^2 - \nabla_{\mathbf{r}}^2 - 2i\alpha(K_x\partial_x + K_y\partial_y)\right]}{\varepsilon\sigma_0 + \gamma(\sigma_0 + \sigma_3)}\psi_c = \sigma_0\varepsilon\psi_c. \end{aligned} \quad \text{(A.18)}$$

as $\psi_c = \begin{pmatrix}\phi_{cc}\\ \phi_{cv}\end{pmatrix}$, where $\phi_{cc}(\mathbf{r}) = \phi_c(\mathbf{r}_1)\phi_v(\mathbf{r}_2)$, then we could write (A.18) as

$$\begin{pmatrix} V(r) & -at(\beta K_- + i\partial_x + \partial_y)\\ -at(\beta K_+ + i\partial_x - \partial_y) & V(r) + 2\gamma\end{pmatrix}\begin{pmatrix}\phi_{cc}\\ \phi_{cv}\end{pmatrix} +$$

$$+a^2t^2\sigma_0\left[\alpha^2K^2 - \nabla_{\mathbf{r}}^2 - 2i\alpha(K_x\partial_x + K_y\partial_y)\right]\begin{pmatrix}\frac{1}{\varepsilon+2\gamma} & \\ & \frac{1}{\varepsilon}\end{pmatrix}\begin{pmatrix}\phi_{cc}\\ \phi_{cv}\end{pmatrix} = \varepsilon\begin{pmatrix}\phi_{cc}\\ \phi_{cv}\end{pmatrix} \quad \text{(A.19)}$$

which is equivalent to a system of two equations:

$$\begin{aligned}&\left[V(r) + \frac{a^2t^2}{\varepsilon+2\gamma}\left(\alpha^2K^2 - \nabla_{\mathbf{r}}^2 - 2i\alpha(K_x\partial_x + K_y\partial_y)\right)\right]\phi_{cc} -\\ &- at(\beta K_- + i\partial_x + \partial_y)\phi_{cv} = \varepsilon\phi_{cc}, \end{aligned} \quad \text{(A.20)}$$

$$\begin{aligned}&\left[V(r) + 2\gamma + \frac{a^2t^2}{\varepsilon}\left(\alpha^2K^2 - \nabla_{\mathbf{r}}^2 - 2i\alpha(K_x\partial_x + K_y\partial_y)\right)\right]\phi_{cv} -\\ &- at(\beta K_- + i\partial_x - \partial_y)\phi_{cc} = \varepsilon\phi_{cv}. \end{aligned} \quad \text{(A.21)}$$

As our goal is to obtain an equation for one electron in c and one hole in v, i. e. for ϕ_{cv}, we first obtain ϕ_{cc} from (A.20):

$$\phi_{cc} = \left[V(r) - \varepsilon + \frac{a^2t^2}{\varepsilon + 2\gamma}\left(\alpha^2K^2 - \nabla_{\mathbf{r}}^2 - 2i\alpha(K_x\partial_x + K_y\partial_y)\right)\right]^{-1} \times \\ \times at(\beta K_- + i\partial_x + \partial_y)\phi_{cv}. \tag{A.22}$$

Using again the approximation of low kinetic energy and Coulomb interaction,

$$\left[V(r) - \varepsilon + \frac{a^2t^2}{\varepsilon + 2\gamma}\left(\alpha^2K^2 - \nabla_{\mathbf{r}}^2 - 2i\alpha(K_x\partial_x + K_y\partial_y)\right)\right]^{-1} = -\frac{1}{\varepsilon} - \mathscr{O}\{k^2, V(r)\}, \tag{A.23}$$

thus, (A.22) is approximated as:

$$\phi_{cc} \approx -\frac{at(\beta K_- + i\partial_x + \partial_y)}{\varepsilon}\phi_{cv}, \tag{A.24}$$

and equation (A.21) becomes:

$$\left[V(r) + 2\gamma + \frac{a^2t^2}{\varepsilon}\left(\beta^2K^2 - \nabla_{\mathbf{r}}^2 + 2i\beta(K_x\partial_x + K_y\partial_y)\right) + \right. \\ \left. + \frac{a^2t^2}{\varepsilon}\left(\alpha^2K^2 - \nabla_{\mathbf{r}}^2 - 2i\alpha(K_x\partial_x + K_y\partial_y)\right)\right]\phi_{cv} = \varepsilon\phi_{cv} \tag{A.25}$$

If we make $\alpha = \beta = 1/2$, then

$$\left[V(r) + (\Delta - \lambda) + \frac{a^2t^2K^2}{2\varepsilon} - \frac{2a^2t^2}{\varepsilon}\nabla_{\mathbf{r}}^2\right]\phi_{cv} = \varepsilon\phi_{cv}. \tag{A.26}$$

Using the Coulomb form of the potential $V(r)$, we write the equation in a convenient way:

$$\left[-\frac{2a^2t^2}{\varepsilon}\nabla_{\mathbf{r}}^2 - \frac{e^2}{4\pi\varepsilon_0\varepsilon r}\right]\phi_{cv} = \left[\varepsilon - \Delta + \lambda - \frac{a^2t^2K^2}{2\varepsilon}\right]\phi_{cv} \tag{A.27}$$

or

$$\left[\mathscr{F}_1(\varepsilon)\nabla_{\mathbf{r}}^2 - \frac{e^2}{4\pi\varepsilon_0\varepsilon}\right]\phi_{cv} = \mathscr{F}_0(\varepsilon)\phi_{cv}, \tag{A.28}$$

where $\mathscr{F}_1(\varepsilon) = \frac{2a^2t^2}{\varepsilon}$ ans $\mathscr{F}_0(\varepsilon) = \varepsilon - \Delta + \lambda - \frac{a^2t^2K^2}{2\varepsilon}$. Equation (A.28) is that of the two-dimensional hydrogenoid atom. As it is well known, the wavefunctions of the 2D hydrogenoid atom are the product of a decaying exponential function (which represents the asymptotic behavior at high r), an integer-power of r (for

asymptotically small r) and hypergeometric functions for intermediate values of r. The energy spectrum is characterized by the quantum number n as

$$\mathscr{F}_0 = -\left(\frac{e^2}{4\pi\varepsilon_0\varepsilon}\right)^2 \frac{1}{4\mathscr{F}_1(n-1/2)^2} \tag{A.29}$$

and the normalized wavefunctions [100] are:

$$\begin{aligned}\phi_{cv} =& \frac{\beta_n}{2|l|}\left[\frac{(n+|l|-1)!}{(n-|l|-1)!(2n-1)}\right]^{1/2} e^{-\beta_n r/2}(\beta_n r)^{|l|}\times \\ &\times \frac{e^{il\phi}}{\sqrt{2\pi}} F(-n+|l|+1, 2|l|+1, \beta_n r),\end{aligned} \tag{A.30}$$

where $\beta_n = e^2/(n-1/2)4\pi\varepsilon_0\varepsilon\mathscr{F}_1(\varepsilon)$. We can manipulate equation (A.29) to know the energy value, from which it follows that:

$$\frac{2\zeta}{\varepsilon}\left(\varepsilon - (\Delta-\lambda) - \frac{\zeta K^2}{2\varepsilon}\right) = -\frac{C}{4}, \tag{A.31}$$

where $C = (e^2/(4\pi\varepsilon_0\varepsilon)(n-1/2))^2$, and $\zeta = a^2t^2$. Multiplying both sides of the last equation by $4\varepsilon^2$ and solving the resulting 2nd-degree algebraic equation, we obtain the energy:

$$\varepsilon = \frac{1}{8\zeta + C}\left[4\zeta(\Delta-\lambda) \pm \sqrt{(4\zeta(\Delta-\lambda))^2 + 4(8\zeta+C)\zeta^2K^2}\right] \tag{A.32}$$

That is the energy dispersion $\varepsilon(K)$ of an exciton in TMDC. In the *low energy regime*, K^2 is small and we can expand (A.32) to get

$$\varepsilon = \varepsilon(0) + \frac{\hbar^2}{2M}K^2, \tag{A.33}$$

where

$$\varepsilon(0) = \frac{8\zeta(\Delta-\lambda)}{8\zeta+C}, \qquad M = \frac{\hbar^2(\Delta-\lambda)}{\zeta}, \tag{A.34}$$

are the exciton rest energy and mass, respectively. The exciton binding energy is obtained by making $n = 1$ from equation (A.29):

$$E_B = \frac{C(\Delta-\lambda)}{8\zeta+C} \tag{A.35}$$

These are the results exposed in Chapter 4 for the properties of the exciton.

REFERENCES

1. Various. *MoS_2: Materials, Physics and Devices*. Number 21 in Lecture Notes in Nanoscale Science and Technology. Springer, Chengdu, 2014.
2. P. Kannan, D. Late, H. Morgan, and C. Rout. Recent developments in 2D layered inorganic nanomaterials for sensing. *Nanoscale*, 7:13293, 2015.
3. G. Fiori, F. Bonaccorso, G. Iannaccone, T. Palacios, D. Neumaier, A. Seabaugh, S. K. Banerjee, and L. Colombo. Electronics based on two-dimensional materials. *Nat. Nanotechnol.*, 9:768, 2014.
4. J. Fan, T. Li, and I. Djerdj. Two-Dimensional Atomic Crystals: Paving New Ways for Nanoelectronics. *J. Electron. Mater.*, 44:4080, 2015.
5. Q. Peng and S. Deab. Outstanding mechanical properties of monolayer MoS_2 and its application in elastic energy storage. *Phys. Chem. Chem. Phys.*, 15:19427, 2013.
6. C. Ataca, H. Şahin, E. Aktürk, and S. Ciraci. Mechanical and electronic properties of mos2 nanoribbons and their defects. *The Journal of Physical Chemistry C*, 115(10):3934–3941, 2011.
7. Noah F. Q. Yuan, Kin Fai Mak, and K. T. Law. Possible topological superconducting phases of mos_2. *Phys. Rev. Lett.*, 113:097001, Aug 2014.
8. G. T. Einevoll. Confinement of excitons in quantum dots. *Phys. Rev. B*, 45:3410–3417, Feb 1992.
9. Garnett W. Bryant. Theory for quantum-dot quantum wells: Pair correlation and internal quantum confinement in nanoheterostructures. *Phys. Rev. B*, 52:R16997–R17000, Dec 1995.
10. Y. Masumoto and T. Takagahara. *Semiconductor Quantum Dots: Physics, Spectroscopy and Applications*. Nanoscience and Nanotechnology. Springer, 2002.
11. Y. Li, Y. Zhao, H. Cheng, Y. Hu, G. Shi, L. Dai, and L. Qu. Nitrogen-Doped Graphene Quantum Dots with Oxygen-Rich Functional Groups. *J. Am. Chem. Soc.*, 134:15, 2012.
12. K. Mak, C. Lee, J. Hone, J. Shan, and T. Heinz. Atomically Thin MoS_2: A New Direct-Gap Semiconductor. *Phys. Rev. Lett.*, 105:136805, 2010.
13. D. Kufer, I. Nikitskiy, T. Lasanta, G. Navickaite, F. Koppens, and G. Konstantatos. Hybrid 2D–0D MoS_2 –PbS Quantum Dot Photodetectors. *Adv. Mater.*, 27:176, 2015.
14. C. Chen, H. Qiao, S. Lin, C. Luk, Y. Liu, and Z. Xu. Highly responsive MoS_2 photodetectors enhanced by graphene quantum dots. *Sci. Rep.*, 5:11830, 2015.

15. D. Gopalakrishnan, D. Damien, and M. Shaijumon. MoS_2 Quantum Dot-Interspersed Exfoliated MoS_2 Nanosheets. *ACS Nano*, 8:5297, 2014.

16. H. Dong, S. Tang, Y. Hao, H. Yu, W. Dai, and G. Zhao. Fluorescent MoS_2 Quantum Dots: Ultrasonic Preparation, Up-Conversion and Down-Conversion Bioimaging, and Photodynamic Therapy. *ACS Appl. Mater. Interfaces*, 8:3107, 2016.

17. Y. Li, H. Wang, L. Xie, Y. Liang, G. Hong, and H. Dai. MoS_2 Nanoparticles Grown on Graphene: An Advanced Catalyst for the Hydrogen Evolution Reaction. *J. Am. Chem. Soc.*, 133:7296, 2011.

18. Y. He, G. Clark, J. Schaibley, Y. He, M. Chen, and Y. Wei. Single quantum emitters in monolayer semiconductors. *Nat. Nanotechnol.*, 2015.

19. A. Srivastava, M. Sidler, Andras Kis2 Adrien V. Allain2, Dominik S. Lembke2, and A. Imamoğlu1. Optically active quantum dots in monolayer WSe_2. *Nat. Nanotechnol.*, 10:491, 2015.

20. M. Koperski, K. Nogajewski, A. Arora, V. Cherkez, P. Mallet, J.-Y. Veuillen, J. Marcus, P. Kossacki, and M. Potemski. Single photon emitters in exfoliated WSe_2 structures. *Nat. Nanotechnol.*, 2015.

21. C. Chakraborty, L. Kinnischtzke, K. Goodfellow, Ryan Beams, and A. Vamivakas. Voltage-controlled quantum light from an atomically thin semiconductor. *Nat. Nanotechnol.*, 2015.

22. J. Feng, X. Qian, C. Huang, and J. Li. Strain-engineered artificial atom as a broad-spectrum solar energy funnel. *Nat. Photonics*, 6:285, 2012.

23. S. Kumar, A. Kaczmarczyk, and B. D. Gerardot. Strain-Induced Spatial and Spectral Isolation of Quantum Emitters in Mono- and Bilayer WSe_2. *Nano Lett.*, 15:7567, 2015.

24. K. S. Novoselov, D. Jiang, F. Schedin, T. J. Booth, V. V. Khotkevich, S. V. Morozov, and A. K. Geim. Two-dimensional atomic crystals. In *Proceedings of the National Academy of Sciences*, 2005.

25. B. Radisavljevic, A. Radenovic, J. Brivio, V. Giacometti, and A. Kis. Single-layer MoS_2 transistors. *Nat. Nanotechnol.*, 6:147, 2011.

26. S. Li ans K Yang, C. Tan, X. Huang, W. Huangb, and H. Zhang. Preparation and applications of novel composites composed of metal–organic frameworks and two-dimensional materials. *Chem Comm*, 52:1555, 2016.

27. B. Radisavljevic, M. Whitwick, and A. Kis. Integrated Circuits and Logic Operations Based on Single-Layer MoS2. *ACS Nano*, 5:9934, 2011.

28. O. Lopez-Sanchez, D. Lembke, M. Kayci, A. Radenovic, and A. Kis. Ultrasensitive photodetectors based on monolayer MoS_2. *Nat. Nanotechnol.*, 8:497, 2013.

29. M.Tsai, S. Su, J. Chang, Dand Tsai, C. Chen, C. Wu, L. Li, L. Chen, and J. He. Monolayer MoS_2 Heterojunction Solar Cells. *ACS Nano*, 8:8317, 2014.

30. M. Vasilevskiy, A. Santiago-Pérez, C. Trallero-Giner, N. Peres, and A. Kavokin. Exciton polaritons in two-dimensional dichalcogenide layers placed in a planar microcavity: Tunable interaction between two Bose-Einstein condensates. *Phys Rev B*, 92:245435, 2015.

31. D.G. Teer. New solid lubricant coatings. *Wear*, 251(1-12):1068–1074, oct 2001.

32. J. Wanga, M. Gua, B. Songhaob, and S. Gec. Investigation of the influence of MoS_2 filler on the tribological properties of carbon fiber reinforced nylon 1010 composites. *14th International Conference on Wear of Materials*, 255:774, 2003.

33. R. V. Kasowski. Band Structure of MoS_2 and NbS_2. *Phys. Rev. Lett.*, 30:1175, 1973.

34. Gotthard Seifert, Humberto Terrones, Mauricio Terrones, Gerd Jungnickel, and Thomas Frauenheim. Structure and electronic properties of mos_2 nanotubes. *Phys. Rev. Lett.*, 85:146–149, Jul 2000.

35. H. Li, J. Wu, Z. Yin, and H. Zhang. Preparation and Applications of Mechanically Exfoliated Single-Layer and Multilayer MoS_2 and WSe_2 Nanosheets. *Acc. Chem. Res.*, 47:1067, 2014.

36. X. Li and H. Zhu. Two-dimensional MoS_2: Properties, preparation, and applications. *Journal of Materiomics*, 1:33, 2015.

37. Jeffrey D. Cain, Fengyuan Shi, Jinsong Wu, and Vinayak P. Dravid. Growth mechanism of transition metal dichalcogenide monolayers: The role of self-seeding fullerene nuclei. *ACS Nano*, 10(5):5440–5445, 2016. PMID: 27138735.

38. H. F. Liu, S. L. Wong, and D. Z. Chi. Cvd growth of mos2-based two-dimensional materials. *Chemical Vapor Deposition*, 21(10-11-12):241–259, 2015.

39. Néstor Perea-López, Zhong Lin, Nihar R Pradhan, Agustín Iñiguez-Rábago, Ana Laura Elías, Amber McCreary, Jun Lou, Pulickel M Ajayan, Humberto Terrones, Luis Balicas, and Mauricio Terrones. Cvd-grown monolayered mos 2 as an effective photosensor operating at low-voltage. *2D Materials*, 1(1):011004, 2014.

40. Dongri Qiu and Dong Uk Lee and Sang Woo Pak and Eun Kyu Kim. Structural and optical properties of MoS2 layers grown by successive two-step chemical vapor deposition method . *Thin Solid Films*, 587:47 – 51, 2015. {ICMAP} 2014.

41. D. Dumcenco, D. Ovchinnikov, K. Marinov, P. Lazi, M. Gibertini, N. Marzari, O. Lopez Sanchez, Y. Kung, D. Krasnozhon, and M. Chen. Large-Area Epitaxial Monolayer MoS_2. *ACS Nano*, 4:4611, 2015.

42. Yingchun Cheng, Kexin Yao, Yang Yang, Liang Li, Yingbang Yao, Qingxiao Wang, Xixiang Zhang, Yu Han, and Udo Schwingenschlögl. Van der Waals epitaxial growth of MoS2 on SiO2/Si by chemical vapor deposition. *RSC Advances*, 3(38):17287, 2013.

43. P. Hohenberg and W. Kohn. Inhomogeneous Electron Gas. *Phys Rev*, 136:864, 1964.

44. W. Kohn. Nobel Lecture: Electronic structure of matter—wave functions and density functionals. *Rev. Mod. Phys.*, 71:1253, 1998.

45. P. Yu and M. Cardona. *Fundamentals of Semiconductors*. Graduate texts in Physics. Springer, 2010.

46. W. Feng, Y. Yao, W. Zhu, J. Zhou, W. Yao, and D. Xiao. Intrinsic spin Hall effect in monolayers of group-VI dichalcogenides: A first-principles study. *Phys Rev B*, 86:165108, 2012.

47. K. Mak, K. He, J. Shan, and T. F. Heinz. Control of valley polarization in monolayer MoS_2 by optical helicity. *Nat. Nanotechnol.*, 96:1, 2012.

48. Q. Yue, J. Kangb, Z. Shao, X. Zhang, S. Chang, and G. Wang. Mechanical and electronic properties of monolayer MoS_2 under elastic strain. *Phys. Lett. A*, 376:1166, 2012.

49. A. Castellanos-Gomez, M. Poot, G. Steele, H. van der Zant, N. Agrait, and G. Rubio-Bollinger. Elastic properties of freely suspended MoS_2 nanosheets. *Adv. Mater.*, 24:772, 2012.

50. A. Ramasubramaniam. Large excitonic effects in monolayers of molybdenum and tungsten dichalcogenides. *Phys. Rev. B*, 86:2012, 2012.

51. C. Ataca, M. Topsakal, E. Akturk, and S. Ciraci. A Comparative Study of Lattice Dynamics of Three- and Two-Dimensional MoS_2. *J. Phys. Chem. C*, 115:16354, 2011.

52. P. Tonndorf, R. Schmidt, P. Böttger, X. Zhang, J. Börner, A. Liebig, M. Albrecht, C. Kloc, and O. Gordan. Photoluminescence emission and Raman response of monolayer MoS_2, $MoSe_2$, and WSe_2. *Opt. Express*, 4:4908, 2013.

53. H. Li, Q. Zhang, C. C. Yap, and B. K. Tay. From Bulk to Monolayer MoS_2 : Evolution of Raman Scattering. *Adv. Funct. Mater.*, 22:1385, 2012.

54. C. Lee, H. Yan, Louis E. Brus, T. Heinz, J. Hone, and S. Ryu. Anomalous Lattice Vibrations of Single and Few-Layer MoS_2. *ACS Nano*, 4:2695, 2010.

55. M. Fox. *Optical properties of solids*. Number 3 in Oxford master series in condensed matter physics. Oxford University Press, 2 edition, 2012.

56. D. Qiu, F. da Jornada, and S. Louie. Optical Spectrum of MoS_2: Many-Body Effects and Diversity of Exciton States. *Phys. Rev. Lett.*, 111:216805, 2013.

57. Haining Wang, Changjian Zhang, and Farhan Rana. Ultrafast Dynamics of Defect-Assisted Electron–Hole Recombination in Monolayer MoS2. *Nano Letters*, 15(1):339–345, 2015. PMID: 25546602.

58. A. Thilagam. Ultrafast exciton relaxation in monolayer transition metal dichalcogenides. *J. Appl. Phys.*, 119:164306, 2016.

59. A. Kavokin, J. Baumberg, G. Malpuech, and F. Laussy. *Microcavities*, chapter 4, pages 127–137. Oxford University Press, 20017.

60. V. Agranovich and G. Bassani. *Electronic excitations in organic based nanostructures*, volume 31 of *Thin Films and Nanostructures*. Academic Press, Amsterdam, 2003.

61. G. Wannier. The structure of electronic excitation levels in insulating crystals. *Phys. Rev.*, 52:191, 1937.
62. V. Agranovich, H. Benisty, and C. Weisbuch. Organic and inorganic quantum wells in a microcavity: Frenkel–Wannier–Mott excitons hybridization and energy transformation. *Solid State Commun.*, 102:631, 1997.
63. R. Roldan, A. Castellanos-Gomez, E. Cappelluti, and Francisco Guinea. Strain engineering in semiconducting two-dimensional crystals. *J. Phys.: Condens. Matter*, 27:313201, 2015.
64. J. Wrachtrup. Single photons at room temperature. *Nat. Nanotechnol.*, 11:7, 2016.
65. SuperSharpSilicon. Non-Contact Tapping mode High Resonance Frequency Reflex Coating afm tip SSS-NCHR datasheet.
66. T. Berkelbach, M. Hybertsen, and D. Reichman. Theory of neutral and charged excitons in monolayer transition metal dichalcogenides. *Phys Rev B*, 88:045318, 2013.
67. J. S. Ross, S. Wu, H. Yu, N. J. Ghimire, A. M. Jones, and G. Aivazian. Electrical control of neutral and charged excitons in a monolayer semiconductor. *Nat. Commun.*, (2498), 2012.
68. K. Mak, K. He, C. Lee adn G. H. Lee, J. Hone, T. F. Heinz, and Jie Shan2. Tightly bound trions in monolayer MoS_2. *Nat. Mater.*, (3505), 2012.
69. T. J. Wallin. Mechanical Properties of Polymer Nanocomposites Based on Functionalized Graphene Sheets. Technical report, College of William and Mary Physics Department in Virginia, 2010.
70. T. Fernandes. Friction-induced artifact in atomic force microscopy topographic images. Master's thesis, UFMG, 2014.
71. Daniel Rugar and Paul Hansma. Atomic Force Microscopy, 1990.
72. E. Meyer. Atomic force microscopy. *Progress in Surface Science*, 41(1):3–49, 1992.
73. J. Sader, J. Chon, and P. Mulvaney. Calibration of rectangular atomic force microscope cantilevers. *Rev. Sci. Instrum.*, 70:3967, 1999.
74. J. Sader. Frequency response of cantilever beams immersed in viscous fluids with applications to the atomic force microscope. *J. Appl. Phys.*, 84:64, 1998.
75. B. Sinisa, D. Mesarovic, and N. Fleck. Spherical indentation of elastic-plastic solids. *Proc. R. Soc. Lond. A*, 455:2707, 1999.
76. Andor. Optical Etaloning in CCDs and EMCCDs. Technical report, Available in `http://www.andor.com`, 2012.
77. A. Ramirez-Torres, V. Turkowski, and T. Rahman. Time-dependent density-matrix functional theory for trion excitations: Application to monolayer MoS_2 and other transition-metal dichalcogenides. *Phys Rev B*, 90:085419, 1990.
78. T. Cheiwchanchamnangij and W. Lambrecht. Quasiparticle band structure calculation of monolayer, bilayer, and bulk MoS_2. *Phys. Rev. B*, 85:205302, 2012.
79. J. Li, Y. Zhong, and D. Zhang. Excitons in monolayer transition metal dichalcogenides. *J. Phys.: Condens. Matter*, 27:315301, 2015.
80. E. Cappelluti, R. Roldan, J. A. Silva-Guillen, P. Ordejon, and F. Guinea. Tight-binding model and direct-gap/indirect-gap transition in single-layer and multilayer MoS_2. *Phys. Rev. B*, 88:075409, 2013.
81. D. Xiao, G. Liu, W. Feng, X. Xu, and W. Yao. Coupled Spin and Valley Physics in Monolayers of MoS_2 and Other Group-VI Dichalcogenides. *Phys. Rev. Lett.*, 108:196802, 2012.
82. A. Kormányos, V. Zólyomi, N. Drummond, P. Rakyta, G. Burkard, and V. Fal'ko. Monolayer MoS_2: Trigonal warping, the Γ valley, and spin-orbit coupling effects. *Phys. Rev. B*, 88:045416, 2013.
83. O. Berman, R. Kezerashvili, and K. Ziegler. Coupling of two Dirac particles. *Phys Rev A*, 87:042513, 2013.
84. J. Sabio, F. Sols, and F. Guinea. Two-body problem in graphene. *Phys. Rev. B*, 81:045428, 2010.
85. Mildred S Dresselhaus, Gene Dresselhaus, and Ado Jorio. *Group Theory: Application to the Physics of Condensed Matter*, volume 53. Springer, 2008.
86. J. Ribeiro-Soares, R. M. Almeida, E. B. Barros, P. T. Araujo, M. S. Dresselhaus, L. G. Cancado, and A. Jorio. Group theory analysis of phonons in two-dimensional transition metal dichalcogenides. *Phys Rev B*, 90:115438, 2014.

87. A. Castellanos-Gomez, R. Roldan, E. Cappelluti, and M. Buscema. Local Strain Engineering in Atomically Thin MoS_2. *Nano Lett.*, 13:5361, 2013.

88. T. Cheiwchanchamnangij, W. Lambrecht, Y. Song, and H. Dery. Strain effects on the spin-orbit-induced band structure splittings in monolayer MoS_2 and graphene. *Phys. Rev. B*, 88:155404, 2013.

89. J. Hutchinson and K. Neale. Finite strain J_2 deformation theory. In D. Carlson, editor, *Proceedings of the IUTAM Symposium of Finite Elasticity*, 1981.

90. A. McCreary, R. Ghosh, M. Amani, J. Wang, and K. Duerloo. Effects of Uniaxial and Biaxial Strain on Few-Layered Terrace Structures of MoS_2 Grown by Vapor Transport. *ACS Nano*, 10:3186, 2016.

91. I. Szlufarska. Atomistic simulations of nanoindentation. *Mater. Today*, 9:42, 2006.

92. J. Stewart and D. Spearot. Atomistic simulations of nanoindentation on the basal plane of crystalline molybdenum disulfide (MoS_2). *Modelling Simul. Mater. Sci. Eng.*, 21:045003, 2013.

93. J. Cong-rui. Large deflection of circular membrane under concentrated force. *Appl. Math. Mech.*, 29:889, 2008.

94. U. Hangen. Time Dependent Deformation Behavior of PMMA. Technical report, Hysitron, Inc., 2010.

95. A. Cleland. *Foundations of nanomechanics: From Solid-State Theory to Device Applications*. Advanced texts in Physics. Springer, 2003.

96. S. Luo, G. Hao, Y. Fan, L. Kou, and C. He. Formation of ripples in atomically thin MoS_2 and local strain engineering of electrostatic properties. *Nanotechnology*, 26:105705, 2015.

97. Y. Varshni. Temperature dependence of the energy gap in semiconductors. *Physica*, 34:149, 1967.

98. S. Tongay, J. Suh, C Ataca, W. Fan, A. Luce, and J. Kang. Defects activated photoluminescence in two-dimensional semiconductors: interplay between bound, charged, and free excitons. *Sci. Rep.*, 3:2657, 2013.

99. J. Zimmermann. Low temperature thermal relaxation in polymethyl methacrylate (PMMA). *Cryogenics*, page 27, 1984.

100. X. L. Yang, S. H. Guo, and F. T. Chan. Analytic solution of a two-dimensional hydrogen atom. I. Nonrelativistic theory. *Phys. Rev. A*, 43:1186, 1991.

Colophon

This document was typeset using the the LaTeX- based typographical style of the 7”$\times$10” WILEY INTERSCIENCE books, with several modifications made by José D. Hernández to adapt the document to the A4, 11pt style for a dissertation.